ÇUKUROVA UNIVERSITY
INSTITUTE OF NATURAL AND APPLIED SCIENCES

PhD. THESIS

Yalçın GÜLER

SEARCH FOR FERMION PORTAL DARK MATTER AND LARGE EXTRA DIMENSION PRODUCED WITH JETS AND MISSING TRANSVERSE ENERGY IN PROTON - PROTON COLLISIONS AT $\sqrt{s}$= 13 TeV

DEPARTMENT OF PHYSICS

ADANA-2018

ÇUKUROVA UNIVERSITY
INSTITUTE OF NATURAL AND APPLIED SCIENCES

SEARCH FOR FERMION PORTAL DARK MATTER AND LARGE EXTRA DIMENSION PRODUCED WITH JETS AND MISSING TRANSVERSE ENERGY IN PROTON - PROTON COLLISIONS AT $\sqrt{s}$= 13 TEV

Yalçın GÜLER

PhD THESIS

DEPARTMENT OF PHYSICS

We certify that the thesis titled above was reviewed and approved for the award of degree of the Doctor of Philosophy by the board of jury on 21/12/2018.

……	……..……	.....
Prof. Dr. İsa DUMANOGLU	Prof. Dr. Aysel Kayış TOPAKSU	Prof. Dr. Sefa ERTÜRK
SUPERVISOR	MEMBER	MEMBER
……..	……	
Assoc. Prof. Dr. Sezgin AYDIN	Prof. Dr. Eda EŞKUT	
MEMBER	MEMBER	

This PhD Thesis is performed in Department of Physics of Institute of Natural And Applied Sciences of Çukurova University.
Registration Number:

Prof. Dr. Mustafa GÖK
Director
Institute of Natural and Applied Sciences

This Study was supported by Çukurova University Scientific Research Fund.Project Number: FDK-2015-2915

Note:The usage of the presented specific declerations, tables, figures, and photographs either in this thesis or in any other reference without citiation is subject to "The law of Arts and Intellectual Products" number of 5846 of Turkish Republic.

This thesis is dedicated to my parents.
For their endless love, support and encouragement

ABSTRACT

PhD. THESIS

SEARCH FOR FERMION PORTAL DARK MATTER AND LARGE EXTRA DIMENSION PRODUCED WITH JETS AND MISSING TRANSVERSE ENERGY IN PROTON - PROTON COLLISIONS AT $\sqrt{s}$= 13 TeV

Yalçın GÜLER

ÇUKUROVA UNIVERSITY
INSTITUTE OF NATURAL AND APPLIED SCIENCES
DEPARTMENT OF PHYSICS

Supervisor	: Prof. Dr. İsa DUMANOĞLU
Co-Supervisor	: Assoc. Prof. Dr. Bayram TALİ
	Year: 2018, Page: 150
Jury	: Prof. Dr. İsa DUMANOĞLU
	: Prof. Dr. Aysel KAYIŞ TOPAKSU
	: Assoc. Prof. Dr. Sezgin AYDIN
	: Prof. Dr. Sefa ERTÜRK
	: Prof. Dr. Eda EŞKUT

Monojet analysis provides significant contributions to the new physics explorations at collider experiments. The search for dark matter is conducted for events containing one or more energetic jets with imbalanced transverse momentum using 35.9 fb^{-1} proton-proton collision data collected with CMS detector at LHC. Since SM expectation and observed events are in good agrement, no evidece was found neither for dark matter nor for extra dimensions. The results were interpreted for fermion portal dark matter and ADD model with large extra spatial dimensions. Then limits were set to mediator and dark matter masses for fermion portal model and to Planck Scale as a function of number of extra dimensions for ADD model.

Key Words: Dark Matter, Fermion Portal, ADD, LHC, CMS, Monojet

ÖZ

DOKTORA TEZİ

√S = 13 TeV'LİK PROTON - PROTON ÇARPIŞMASINDA, JETLER VE KAYIP DİK ENERJİLERİN OLUŞMASIYLA, FERMİYON KANALI KARANLIK MADDE VE EKSTRA BOYUT ARAŞTIRMALARI

Yalçın GÜLER

ÇUKUROVA ÜNİVERSİTESİ
FEN BİLİMLERİ ENSTİTÜSÜ
FİZİK ANABİLİM DALI

Danışman : Prof. Dr. İsa DUMANOĞLU
İkinci Danışman : Doç. Dr. Bayram TALİ
Yıl: 2018, Sayfa: 150
Jüri : Prof. Dr. İsa DUMANOĞLU
: Prof. Dr. Aysel KAYIŞ TOPAKSU
: Doç. Dr. Sezgin AYDIN
: Prof. Dr. Sefa ERTÜRK
: Prof. Dr. Eda EŞKUT

Monojet analizi, çarpıştırıcı deneylerinde yeni fizik keşiflerine önemli katkılar sağlar. Karanlık madde, BHÇ'deki CMS detektöründen elde edilen 35.9 fb^{-1}'lık proton-proton çarpışma verileri kullanılarak, bir veya daha fazla yüksek enerjili jetlerin dik momentumlarının dengelenmediği olaylarda araştırılmıştır. SM'den beklenen ve ölçülen olayların uyum içinde olması nedeniyle karanlık madde varlanamamıştır. Sonuçlar fermion kanalı karanlık madde ve ek boyutlu ADD modeli açısından yorumlanmıştır. Sonuçta fermiyon kanalı için aracı ve karanlık madde kütlesine ve ADD modeli içinse ek boyutların bir fonksiyonu olarak Planck ölçeğine limitler konulmuştur.

Anahtar Kelimeler: Karanlık Madde, Fermiyon Kanalı, ADD, BHÇ, CMS, Tekjet

GENİŞLETİLMİŞ ÖZET

Protonlar, elektronlar, nötronlar, nötrinolar ve hatta kuarklar genellikle bilimsel keşif haberlerinde duyduğumuz terimlerdir. Bunların hepsi ve diğer parçacıklar mikroskoplarda bile görülemeyecek kadar küçük atom altı parçacıklardır. Moleküller ve atomlar, görebildiğimiz ve hissedebildiğimiz bilinen maddelerin temel öğeleri iken, atom altı parçacıkları öğrenmek ve evrenimizin doğasını anlamak için atomların içine bakmaya ihtiyacımız vardır. Bu çalışmanın bilimine, Parçacık Fiziği veya Yüksek Enerji Fiziği (YEF) denir.

Atomlar uzun zaman önce, Yunan filozof Democritus tarafından ortaya atılmıştır ve 20. yüzyılın başına kadar her türlü maddenin temel bölünmez yapıtaşları olduğu düşünülmüştür. 1900'lerde Rutherford ve diğer bilim insanlarının deneyleri aracılığıyla atomların, proton ve nötronlardan oluşan yoğun bir merkezi çekirdekten ve çekirdeği çevreleyen elektronlarla, çoğunlukla boş alandan oluştuğunu öğrendik. Böylece proton, nötron ve elektronları, doğanın temel parçacıkları olarak görmeye başladık.

Parçacık fiziği bilimi, protonları veya elektronları yüksek enerjilerde hızlandırarak çarpıştırıp parçalayabilen, parçacık hızlandırıcılarının icadıyla ilerledi, bu çarpışmalarda bir çok yeni parçacık keşfedildi.

1960'ların başlarında, hızlandırıcılar daha yüksek enerjilere ulaştıkça, çok fazla türde parçacık bulundu. Bunların hepsi yeni temel parçacıklar olabilir miydi? Temel parçacıkların neler olduğu karmaşası, geçen yüzyılda yapılan uzun bir dizi deney ve kuramsal çalışmalarla, iki temel parçacık kümesinin çok basit bir planda var olduğu anlaşılana kadar devam etti: kuarklar ve leptonlar (leptonlar; elektronlar, muon, tau ve onların nötrinolarıdır) ve bunların birbirleriyle etkileşime girmesine izin veren bir dizi temel kuvvetler. Bu kuvvetlerin, ayar bozonları denilen parçacıkların değişimiyle iletildiği kabul edilir. Bunların bir örneği fotondur. Foton elektromanyetik kuvvetin taşıyıcısıdır.

Proton, nötron veya hızlandırıcı deneylerinde görülen diğer parçacıkların tamamı, bu temel parçacıkların çeşitli kombinasyonundan oluşurlar. Tüm bu parçacık kümeleri, onların karşıt parçacıklarını da içerir. Bunlar, madde ve anti-maddeyi oluştururlar.

Madde en temelde kuarklar ve elektron denilen küçük parçacıklardan oluşur. Kuarklar altı çeşittir: yukarı (u), aşağı (d), çekici (c), garip (s), üst (t) ve alt (b). Kuarkların ve leptonların anti (sembol üzerinde bir çizgi ile belirtilir) olarak adlandırılan karşıt parçacıkları da vardır. Kuarklar, baryon denen daha ağır parçacıkları veya bir antikuarkla birleşerek mezonları oluşturabilirler. Atomların

çekirdeğini oluşturan protonlar ve nötronlar baryonlara, pion veya kaonlar ise mezonlara örnek olarak gösterilebilir. Bugün, **Standart Model (SM)**, bu temel parçacıkların rolünü ve bunlar arasındaki etkileşimleri açıklayan kuramdır. Parçacık Fiziği'nin amaçlarından biri de, bu modeli tüm akla yatkın şekillerde test etmek, daha ötesinde bir şey olup olmadığını keşfetmeye çalışmaktır.

Temel parçacıkların dünyasını anlayabilmek için onları parçalamamız gerekir. Bu da ancak onları yüksek enerjilerde hızlandırıp çarpıştırmakla mümkün olabilir. Bu çarpışma, etkileşim seviyesinde birbirine yaklaşan parçacıkların iç yapı kuvvetlerinin bozulmasına ve temel yapı taşlarının serbest kalmasına yol açar. Çarpışan parçacıklardan etrafa saçılan temel parçacıkların enerjisi dedektörlerin yardımıyla ölçülür. Dedektörlerden toplanan bilgiler parçacıkların birbirleriyle olan hiyerarşik yapısının deneysel olarak gözlemlenmesini sağlar.

Dünyanın en büyük parçacık fiziği labaratuvarı olan CERN (Avrupa Nükleer Araştırma Merkezi), BHÇ (Büyük Hadron Çarpıştırıcısı) de dahil olmak üzere çok sayıda parçacık hızlandırıcısına ve çarpışma deneylerine ev sahipliği yapar. BHÇ, proton ve ağır iyonların (kurşun, altın vs.) ışık hızına yakın hızlara ulaşmasını sağlamak ve saniyede 40 milyon parçacığın çarpışabilmesi için tasarlanmıştır. BHÇ üzerinde yer alan dört büyük dedektör kompleksi vardır. Bunlardan CMS, çok amaçlı fizik analizleri yapabilmek üzere tasarlanmıştır.

CMS'nin amacı SM'de yer alan parçacıkların yapısını ve birbirleriyle olan etkileşimlerini anlayabilmek ve açıklayamadığı konularda SM ötesi fizik araştırmaları yapmaktır. Parçacıkların oluşumu esnasındaki yük parite kırılımı, karanlık maddenin ya da süpersimetrik parçacıkların varlığı, kütle çekimsel kuvvetin anlaşılabilmesi gibi yanıt bekleyen konular SM'in açıklayamadığı konulardır.

SM ötesi araştırma konularından Karanlık Madde (KM) analizleri CMS deneyinde, sonuçları en çok merak edilenlerin başında gelir. KM araştırmaları astrofizik ve yüksek enerji fiziğinin konusudur. Astrofizikte yapılan araştırmalar salt gözleme dayanmaktadır. Parçacık fiziğinde ise araştırmalar kuram ve kuramın öngördüğü şekilde yapılan deneyleri temel almaktadır. BHÇ'de yürütülen KM çalışmaları deneyseldir ve SM ötesi fiziği olarak nitelendirilmektedir.

Bu tezin ilk bölümünde kısaca KM konusunda genel bilgiler verilerek ne zaman ve kimin tarafından gözlendiği konusuna değinilmiştir. KM kuramı ilk olarak Fritz Zwicky tarafından 1930 yıllarında ortaya atılmıştır. Fritz 1933'de Koma adlı gök ada kümesini incelerken, kütlesinin kuramsal olarak beklenilenden ortalama 400 kat daha fazla olduğunu gözlemledi. Bunun sonucunda gözle görülmeyen ve ölçemediğimiz bir kütlenin gök adanın kütlesine katkıda bulunduğunu düşünmüştür

ve bu katkıyı KM olarak değerlendirmiştir. İkinci bölümde SM'i oluşturan temel parçacıklara ve birbirleriyle olan etkileşim ilişkilerine değinilmiştir. KM konusunda daha detaylı bilgiler verilerek hem modeller hem de analiz yöntemleri anlatılmıştır.

Laboratuvar ve deney düzeneklerinin yer aldığı CERN, BHÇ üzerinde yer alan diğer dedektörler ve CMS dedektörünün yapısı konumu alt dedektörleri detaylı bir şekilde ifade edilmiştir.

Bu tezde, tekjet + kayıp enerji olaylarının analizinin yanı sıra çeşitli modellere dayalı fenomenolojik çalışmalar incelenmiş ve veri analiz sonuçlarıyla karşılaştırılmıştır. Bu modeller iyi bilinen ADD (Arkani-Hamed, Dimopoulos, and Dvali) modeli ve sonuçları henüz veri ile karşılaştırılmamış, fermiyon kanalı Dirac KM modelidir. Bu modeller için üretim seviyesi ön değerlendirmeler de çalışılmıştır.

Bu çalışmanın esas bölümü, **Tekjet (Monojet) + kayıp enerji (MET)** analizidir. KM analizi, BHÇ'deki CMS dedektöründe kütle merkezi enerjisi 13 TeV olan proton-proton çarpışmasından elde edilen ve toplam ışıklılık değeri 35.9 fb^{-1}olan veriler kullanılarak gerçekleştirilmiştir. KM sinyalinin, Tekjet + MET olaylarında olabileceği öngörüsüyle analiz gerçekleştirilmiştir. BHÇ'de KM'nin ipuçları olabilecek sinyalleri farklı birçok fiziksel kanalda gözlemlemek mümkündür. Bu fiziksel kanallarından birisi de Tekjet + MET kanalıdır. Enerji-momentum korunumu gereği her olay için jet ile kayıp enerjinin birbirini dengelemesi gerekir. Birçok kuram KM parçacığının BHÇ'de üretilmesi için yeterince hafif olduğunu iddia etmektedir. Eğer KM parçacığının çarpıştırıcıda üretildiği varsayılırsa detektörden fark edilmeden çıkıp gitmelidir. Ancak detektörden çıkarken momentumlarını ve enerjilerini de taşıyacaklarından bu kayıp enerji ve momentum KM parçacığının varlığının işareti olarak kabul edilir. KM parçacığınının bu kuramlardan biri ile açıklanabilmesi evrenin kompozisyonunun daha iyi anlaşılmasına yardımcı olacaktır.

Tekjet analizi için uygun tetiklemelerin belirlenmesi ve bunların verimliliğinin hesaplanması ilk adımdır. Tetikleme verimliliğinin hesaplanmasındaki amaç seçilen olayların maksimum sayıda olmasını sağlamaktır. Ayrıca tetikleyici verimliliği, analizde kullanılan fizik nesnelerinin doğru tespitinin yapılması ve bu tespitin hata payına olan etkisini belirlemek için de gereklidir. Bu kapsamda MET, elektron, müon ve foton tetikleme verimlilikleri hesaplanmıştır.

Tekjet araştırmalarında iki temel husus vardır. Bunlar, sinyal bölgesi olaylarının ve sinyali engelleyen arka plan (kontrol bölgesi) olaylarının belirlenmesidir. Sinyal Bölgesi (SB) ve Kontrol bölgesi (KB) olay seçim kriterleri farklı olup; tetikleyiciler, filtreler, enerji kısıtlamaları gibi kriterler ile belirlenir. Bunun için bir takım fizik nesnelerinin (veya parametrelerin) alınan verinin hem

ışıklılık hem de kütle merkezi enerjisine göre yeniden yapılandırılması gerekmektedir. Bu verilerden istenmeyen olayları (arka plan) sinyal olaylarından, ayırt etmek gerekmektedir. SM süreçlerinden gelen bu kirlilik beş farklı Kontrol Bölgesi (KB) olmak üzere analiz edilerek arka planın etkisi belirlendi. Bu bölgeler şunlardır;

1. İki müon KB $Z \rightarrow \nu\,\nu$ arka plan
2. İki elektron KB $Z \rightarrow \nu\,\nu$ arka plan
3. γ + jets KB $Z \rightarrow \nu\,\nu$ arka plan
4. Tek müon KB W + jets arka plan
5. Tek elektron KB W + jets arka plan

Her bir bölge için belirlenen olay seçim şartı farklıdır ve bu kısıt şartları SM süreçlerinden gelen kayıp dik enerji olaylarını belirlemek üzere seçildi. Tekjet araştırmasında en büyük kirliliğe neden olan arka plan olayları SM süreçlerindeki kayıp kütle oluşumuna neden olan $\mathrm{W}(l\nu) + \mathrm{jets}$ ve $\mathrm{Z}(\nu\nu) + \mathrm{jets}$ olaylarıdır. Tüm KB olaylarından gelen arka plan etkisi, verimlilikler ve sistematik belirsizlikler de hesaba katılıp maksimum olasılık (likelihood) fonksiyonu kullanılarak sinyal bölgesi olarak analiz edilen MC arka plan olaylarına düzeltme faktörü olarak uygulanır. Böylece veri ve MC verileri arasındaki uyum gözlemlenmiş olur. Veri ve MC arasında ki uyum veya uyumsuzluk analizin sonucunu belirleyecektir. Veri ve MC arasındaki farklılık, olay sayısı bazında karşılaştırılır. Elde edilen deneysel bulgular mevcut kuramsal modeller ile karşılaştırıldı. Mevcut kuramsal modellerde bir fazlalık görülemediği için sınır belirleme teknikleri kullanarak KM kütlesi üzerine limitler belirlenmiştir.

Yapılan tekjet analizi, SM arka planından, beklenen ve gözlemlenen olayların uyum içinde olması nedeniyle, mevcut veriler üzerinden sınır değerleri belirleme çalışmasıyla tamamlanmıştır. Sonuçlar basitleştirilmiş modellerden Fermiyon Kanalı Dirac KM modelinde, jetlerle ilişkili KM üretiminin limitleri açısından sunulmuştur. Bu dışarlama limitleri %95 güvenirlilik seviyesinde sinyal gücünün kesilmesine göre $M_{\phi} - M_{\chi}$ düzleminde gösterilmiştir. Dışlama limiti, medyatör (M_{ϕ}) kütlesi için yaklaşık 1.4 TeV'e kadar uzanır ve 600 GeV'e kadar olan KM (M_{χ}) kütle bölgesini dışarlar. Sonuçlar ayrıca, ek uzaysal boyutları öngören ADD modelinin Planck ölçeğindeki sınırlar açısından da yorumlanmıştır. 2'den 6'ya tüm boyutlar için ADD graviton üretiminin sinyal gücünün kesilme değerlerine göre üst limit değerleri belirlenmiştir. Bu limit değerleri Planck ölçeği (M_{D})' nin bir fonksiyonu olarak alt limitler şeklinde gösterilmiştir.

ACKNOWLEDGMENTS

I would like to thank my supervisor İsa DUMANOĞLU. I am particularly grateful to him for giving me a lot of autonomy to complete analysis. For being my advisor, teacher, mentor in many ways. I would like to thank him for always caring, listening, encouraging me to investigate my ideas to the fullest, for making me see the big picture. I accomplished many things with his support and suggestions.

Bayram TALİ, for being co-advisor, mentor and my friend in many ways. I would like to thank him for his support during my studies and contribution to this research and also critical reading of the thesis.

The members of my dissertation committee: Aysel KAYIŞ TOPAKSU, Sezgin AYDIN, Sefa ERTÜRK, and Eda EŞKUT. Thank you for following my progress over the years in the process.

I am especially indebted to Shuichi KUNORI who has been there for me throughout my graduate career. He has helped me tremendously not only with important critical reading of the thesis, but also he found time whenever I needed to discuss my analysis and for that I am very grateful.

I would like to thank my collaborators on the monojet group who helped me complete this thesis and also to those who worked together with me on this physics analysis in particular monojet group sub-convener Zeynep DEMIRAĞLI and Raffaele GEROSA.

My friends and colleagues who have provided endless support and encouragement. In particular, I would like to thank Semiray GİRGİS CHYLA and Roman CHYLA. I also would like to additionally thank my friends Sedat YURT and Ali Eren ŞİMŞEK for helping me with administrative matters.

I also would like thank to team members of High Energy Physics group of Çukurova University, Ayşe POLATÖZ, Gulsen ÖNENGÜT and students for their help.

Special thanks are to our funding agency, Turkish Atomic Energy Authority (TAEK) wich sponsored me during the time I have spent at CERN.

Finally my deepest gratitude is to my family for their unconditional love and encouragement throughout my life. This thesis is dedicated to my beloved family. Last but not least, I would like to thank my dear wife Emine. I am very grateful to her continuous support throughout my research period as well as during thesis write up.

CONTENTS **PAGE**

ABSTRACT I
ÖZ II
GENİŞLETİLMİŞ ÖZET III
ACKNOWLEDGMENTS VII
CONTENTS VIII
LIST OF TABLES XIV
LIST OF FIGURES XVI
ABBREVIATIONS XXVIII
1. INTRODUCTION 1
2. THEORETICAL OVERVIEW 3
2.1. The Standard Model 3
2.2. Particle Content and Interactions 3
2.3. Beyond the Standard Model 7
2.3.1. History of Dark Matter 8
2.3.1.1. Weakly Interacting Massive Particles 12
2.3.2. Experimental Dark Matter Searches 12
2.3.2.1. Direct Detection 13
2.3.2.2. Indirect Detection 13
2.3.2.3. Collider Searches 13
2.3.3. EFT for Dark Matter at Collider Searches 14
2.3.4. Simplified Models 15
3. CERN AND THE LARGE HADRON COLLIDER 17
3.2. Luminosity and Machine Parameters 21
3.3. The LHC Experiments 23
4. COMPACT MUON SELONOID 27
4.1. Tracker 31

4.2. Pixel Detector 32
4.3. Silicon Strip Detector 33
4.4. CMS Calorimeters 34
4.4.1. Electromagnetic Calorimeter 35
4.4.1.1. Electromagnetic Barrel 36
4.4.1.2. Electromagnetic Endcap 37
4.4.1.3. Preshower Detector 37
4.4.2. Hadron Calorimeter 38
4.4.2.1. Hadron Barrel 39
4.4.2.2. Hadron Outer 39
4.4.2.3. Hadron Endcap 40
4.4.2.4. Hadron Forward 40
4.5. Muon System 41
4.5.1. Drift Tube Chambers 42
4.5.2. Cathode Strip Chambers 44
4.5.3. Resistive Plate Chambers 45
4.6 Magnet 45
4.7. Trigger and Data Acquisition System 47
4.7.1. Level 1 Trigger 48
4.7.2. High Level Trigger 48
4.8. CMS Forward Calorimeters 49
4.8.1. Centauro And Strange Object Research Calorimeter 49
4.8.2. Zero Degree Calorimeter 50
5. ADD MODEL 53
5.1. ADD Extra Dimension Model 53
5.2. Large Extra Dimension 53
5.3. Simulation of the Graviton Production in ADD 55
6. FERMION PORTAL DARK MATTER 59

6.1. Fermion Portal Dark Matter 59
6.1.1. Collider Signatures 59
6.1.2. Signal Production 61
6.2. Relic Abundance 65
7. DATA SAMPLES 67
7.1. Data Taking Operations 67
7.2. Monte Carlo Samples for Background Simulation 67
8. TRIGGERS 71
8.1. E_T^{miss} Trigger Performance 72
8.2. Photon Trigger Performance 73
8.3. Electron Trigger Performance 74
9. RECONSTRUCTION of PHYSICS OBJECTS 77
9.1. Reconstruction of Primary Vertex and Pileup Reweighting 77
9.2. Missing Transverse Energy Reconstruction 77
9.3. AK4 Jets Reconstruction 79
9.4. B-tagged Jets Reconstruction 79
9.5. Muons 80
9.5.1. Muon Identification 80
9.5.2. Muon Reconstruction 83
9.6. Electrons 84
9.6.1. Electron Identification 84
9.6.2. Electron Reconstruction 87
9.7. Tau Reconstruction 87
9.8. Photons 88
10. MONTE CARLO REWEIGHTING 91
10.1. Pileup Reweighting for MC samples 91
10.2. Trigger Efficiency 91
10.3. Lepton and Photon Efficiency and Reconstruction Scale Factors 91

10.4. NLO Corrections 91
11. EVENT SELECTIONS 93
11.1. Signal Region 93
11.1.1. Kinematic Distributions in Signal Region 94
11.2. Control Regions 95
11.2.1. Single Muon Control Region 95
11.2.2. Single Electron Control Region 97
11.2.3. Double Muon Control Region 99
11.2.4. Double Electron Control Region 103
11.2.5. Photon+jets Control Region 106
12. BACKGROUND ESTIMATION 109
12.1. Sub-Dominant Backgrounds 109
12.2. Electroweak Background Estimation 109
12.3. Procedure 109
12.4. Transfer Factors 111
13. UNCERTAINTIES 115
13.1. Experimental Uncertainties on Transfer Factors 115
13.2. Theoretical Uncertainties on Transfer Factors 116
13.3. Systematic Uncertainties on Minor Backgrounds 120
13.4. Validation in Data 121
14. RESULTS 125
14.1. Control Region Only Fit 125
14.2. Control + Signal Region Background Only Fit 129
15. MODEL INTERPRETATIONS 133
15.1. Limit on ADD Model 133
15.2. Fermion Portal Dark Matter Model 135
15.2.1. Signal Efficiency 136
15.2.2. Validation of Dirac Fermion Dark Matter Signal 136

15.2.3 Limit on Dirac Fermion Portal Dark Matter Signal 137
16. CONCLUSION 139
REFERENCES 141
CURRICULUM VITAE 149

LIST OF TABLES **PAGE**

Table 3.1. Accelerator chain and corresponding beam energies. 18
Table 3.2. The machine parameters related to the LHC detectors..... 23
Table 4.1. The principal characteristics of the tracker..... 34
Table 4.2. The main characteristics of the CMS solenoid magnet 46
Table 5.1. Datasets are used for ADD signal analysis..... 57
Table 7.1. Data sets used in the analysis. 67
Table 7.2. Background Monte Carlo data sets produced in the Spring16 campaign. 69
Table 8.1. HLT paths, and the associated L1 seeds used in the analysis. '[X]' in the trigger path name stands for 90 or 100 or 110 or 120 GeV..... 71
Table 9.1. Loose electron identification criteria..... 85
Table 9.2. Tight electron identification criteria and HLT safe selection..... 86
Table 9.3. Loose photon identification criteria..... 88
Table 9.4. Tight photon identification criteria..... 89
Table 12.1. Five CRs for backgroun estimation..... 110
Table 13.1. Experimental uncertainties affecting transfer factors used in the analysis to estimate (W, Z, γ)+jets backgrounds in the SR... 115
Table 13.2. Normalisation uncertainties used in the analysis on minor backgrounds populating SR and CRs…... 121

Table 14.1. The SM background predictions and corresponding uncertainties compared to the data in each E_T^{miss} bin are reported in the monojet SR. The background yields and the corresponding uncertainties are obtained after performing a combined fit to data in all the control samples, but excluding data in the SR. 129
Table 15.1. ADD model acceptance for different *n* vs M_D. 133
Table 15.2. Signal efficiency of Dirac FP DM samples after monojet events selection in the M_ϕ - M_χ plane. 136
Table 16.1. Upper limits on the signal production cross section in the ADD model and lower limits on M_D as a functions of the number of extra spatial dimensions (*n*). 140

LIST OF FIGURES **PAGE**

Figure 2.1. Graphic representation of the particle content of the SM. 4

Figure 2.2. Chart representation of composition of Universe 8

Figure 2.3. Astrophysical evidence for Dark Mater. 9

Figure 2.4. Hubble Space Telescope in Abell 1689 indicates the existence of DM. Gravitationel lensing effects can be seen. 10

Figure 2.5. The Bullet Cluster is photographed via the Hubble Space Telescope. The mass distribution deduced from gravitational lensing is highlighted by the blue overlay, while the red overlay highlights X-ray emission as observed by the Chandra telescope X-ray: NASA/CXC/CfA/ 11

Figure 2.6. Illustration of different DM detection methods. 13

Figure 2.7. Illustration of an EFT interaction between DM and the SM..... 14

Figure 2.8. Collider production of DM in terms of a simplified model approach. 15

Figure 3.1. Overview of the Accelerator chain. The LHC is the last ring in a complex chain of particle accelerators. Proton injector chain is LINAC2 → Booster → PS → SPS (Cern accelerator complex) 18

Figure 3.2. Comparison between total integrated luminosity delivered to CMS during proton-proton stable beams collisions in different spans of LHC operation. 19

Figure 3.3. Official luminosity report for 2016. 20

Figure 3.4. The cross section and event rate as a function of the center-of - mass energy for a value of the luminosity $L = 10^{33}\,\mathrm{cm}^{-2}\,\mathrm{s}^{-1}$. 21

Figure 3.5. The LHC and experiments schema. 24

Figure 4.1. Perspective view of the CMS detector and its components. 28
Figure 4.2. A slice of the Compact Muon Solenoid detector. 29
Figure 4.3. Schematic view of the CMS coordinate system..... 30
Figure 4.4. Schematic view of the CMS tracker detector with its components: The Pixel Barrel and the Strip sections, Inner Barrel, Outer Barrel and Endcaps. 31
Figure 4.5. Geometrical layout of pixel detectors in the CMS tracker..... 32
Figure 4.6. Schematic cross section of the CMS tracker in the *r*-*z* plane..... 33
Figure 4.7. Schematic view of the ECAL and the HCAL detectors in and around the CMS magnet 35
Figure 4.8. One-quarter schematic cross sectional view of the CMS electromagnetic calorimeter..... 36
Figure 4.9. Sketch of the electromagnetic calorimeter: EB, EE and preshower Calorimeter..... 37
Figure 4.10. Left: The different HCAL components in the CMS detector. Right: Longitudinal segmentation of the HCAL towers in the central part of the detector. 38
Figure 4.11. Design overview of the CMS muon system. Drift tubes, cathode strip chambers, and resistive plate chambers are indicated..... 42
Figure 4.12. Layout of the CMS barrel muon DT chambers in one of the 5 wheels 43
Figure 4.13. Longitudinal view of one quarter of the detector. Cathode strip hambers of the Endcap Muon system are highlighted 44
Figure 4.14. Schematic view of a RPC chamber..... 45

Figure 4.15. Magnetic field map (left) and field lines (right) predicted for a longitudinal section of the CMS by a magnetic field model at a central magnetic flux density of 3.8 T. Each field line represents a magnetic flux increment of 6 Wb..... 46
Figure 4.16. CMS trigger and DAQ system..... 48
Figure 4.17. Geometry of the CASTOR Calorimeter and its components..... 50
Figure 5.1. Three different production modes for real gravitons *G* production in association with a colored parton (*q* or g) as predicted in the ADD extra dimensions model..... 55
Figure 5.2. Cross-section of ADD signals in pb as a function of MD $n_{ED}$for = 2, 3, 4, 5, 6. 56
Figure 6.1. Diagrams of the main production mechanisms of DM particles in the FP model in association with a single quark or gluon at the LHC. Diagram (a) has two jets in final state, while (b) and (c) provide monojet signatures…..... 60
Figure 6.2. The production cross-sections versus M_χ (left) and M_ϕ (right) for the Dirac DM case 61
Figure 6.3. The fraction of events as a function of M_ϕ for the associated production of mediators M_ϕ (left). (Right) summary fraction plot including also *t*-channel production..... 62
Figure 6.4. Total width of the mediator () in GeV as a function of M_ϕ and M_χ. The black line indicates roughly separation between the on-shell of and off-shell region ($M_\phi < 2\ M_\chi$)..... 63
Figure 6.5. Signal cross section times monojet selection efficiency, expressed in pb, expected different signal hypothesis in the M_ϕ, M_χ plane 64
Figure 6.6. Generator level E_T^{miss}distrubution for different M_ϕ and M_χ..... 65

Figure 6.7. Feynman diagram is showing the annihilation (freeze out) of DM in the early universe, indirect detection of DM and collider production of DM…… 66

Figure 8.1. E_T^{miss} trigger turn-on curve measured in single muon events (left) and single electron events (right). 72

Figure 8.2. Turn on curve, as a function of photon p_T, for the single photon triggers (black), and for the combination of the single photon and EcalHT800 triggers (red). The efficiency is measured in events passing the PFHT650 trigger. 73

Figure 8.3. Single electron trigger efficiency as a function of electron p_T and η. The left plot shows the trigger efficiencies measured using Z tag and probe starting with electron p_T of 20 GeV. The right one shows the electron trigger efficiency measured in the JetHT dataset using events passing the PFHT650 or PFHT800 trigger, starting at electron p_T of 100 GeV. 75

Figure 9.1. Data-MC scale factors for the loose muon selection in events with NPV $\leq$17 (left) and NPV > 17 (right) measured as a function of muon p_T and η. 82

Figure 9.2. Data-MC scale factors for the tight muon selection in events with NPV $\leq$ 17 (left) and NPV > 17 (right) measured as a function of muon p_T and η. 83

Figure 9.3. Data-MC scale factors for the muon tracking efficiency in events with NPV $\leq$ 17 (left) and NPV > 17 (right) measured as a function of muon p_T and η..... 84

Figure 9.4. Data-MC scale factors for the electron veto (left) and tight (right) identification criteria as measured in Z → ee events using a tag and probe method. 86

Figure 9.5. Data-MC scale factors for the electron reconstruction efficiency as a funtion of probe p_T (left) and η (right) as measured in Z → ee events via a tag and probe method. 87
Figure 9.6. The data-MC scale factors for the photon identification and isolation efficiency is measured by e-gamma POG as a function of photon probe p_T and η. 89
Figure 10.1. NLO Higher-order corrections on the Z (left), W(middle), and photon (right) p_T distributions. 92
Figure 11.1. Comparison of the recoil (left), and p_T distribution of the leading jet (right) for data and MC for the SR. 94
Figure 11.2. Comparison of the AK4 jet multiplicity (left), and H_T distribution of the leading jet (right) for data and MC for the SR. 95
Figure 11.3. Comparison of the recoil (left), and p_T distribution of the leading jet (right) for data and MC for the single muon CR. 96
Figure 11.4. Comparison of the AK4 jet multiplicity (left), and p_T distribution of the leading jet the H_T (right) for data and MC for the single muon CR. 96
Figure 11.5. Comparison of the muon p_T (left), and η (right) distribution for data and MC for the single muon CR. 97
Figure 11.6. Comparison of the recoil (left), and p_T distribution of the leading jet (right) for data and MC for the single electron CR. 98
Figure 11.7. Comparison of the AK4 jet multiplicity (left), and H_T distribution of the leading jet (right) for data and MC for the single electron CR. 98
Figure 11.8. Comparison of the electron p_T (left), and η (right) distributions for data and MC for the single electron CR. 99

Figure 11.9. Comparison of the dimuon mass (left), and dimuon p_T distribution (right) for data and MC for the double muon CR. 100
Figure 11.10. Comparison of the recoil (left), and p_T distribution of the leading jet (right) for data and MC for the double muon CR. 101
Figure 11.11. Comparison of the AK4 jet multiplicity (left), and distribution of jet the H_T (right) for data and MC for the double muon CR..... 101
Figure 11.12. Comparison of the leading muon p_T (left), and η (right) distributions for data and MC for the double muon CR. 102
Figure 11.13. Comparison of the subleading muon p_T (left), and η (right) distributions for data and MC for the double muon CR. 102
Figure 11.14. Comparison of the dielectron mass (left), and dielectron p_T distribution (right) for data and MC for the double electron CR. 104
Figure 11.15. Comparison of the recoil (left), and p_T distribution of the leading jet (right) for data and MC for the double electron CR..... 104
Figure 11.16. Comparison of the AK4 jet multiplicity (left) and distribution of jet the H_T (right) for data and MC for the double electron CR. 105
Figure 11.17. Comparison of the leading electron p_T (left) and η (right) distributions for data and MC for the double electron CR..... 105
Figure 11.18. Comparison of the subleading electron p_T (left) and η (right) distributions for data and MC for the double electron CR..... 106
Figure 11.19. Comparison of the recoil (left), and p_T distribution of the leading jet (right) for data and MC for the γ+jets CR..... 107
Figure 11.20. Comparison of the AK4 jet multiplicity (left), and distribution of jet the H_T (right) for data and MC for the γ+jets CR..... 107
Figure 11.21. Comparison of the photon p_T distribution for data and MC for the single photon CR..... 108

Figure 12.1. Transfer factors for the Z→ νν background as a function of the recoil using the dimuon (a), dielectron (b) and photon (c) CR in monojet final state. 113
Figure 12.2. Transfer factors for the W → ℓν background as a function of the *U* using the single muon (left) and single electron (right) CR for the monojet final state. 114
Figure 12.3. Transfer factors for the to estimate the Z(νν)+jets background from W+jets in the SR as a function of the recoil for the monojet final state. 114
Figure 13.1. QCD scale uncertainty as a function of *U* is displayed in (a) for the different *V*+jets processes, while (b) and (c) show the "QCD shape" and the so called "process dependent" uncertainty, respectively. Note that the process dependent uncertainty for W+jets and γ+jets are not onesided. Solid (dashed) lines in (c) are showing the positive (negative) one sigma shift of the related nuisance, which can cross zero as a function of $p_{T.}$ 118
Figure 13.2. Theoretical uncertainties on the Z/W transfer factors (left) nuisances related to the NLO-QCD re-weight + the mixing between QCD and EW corrections, (right) effect of the nuisance parameters related to NLO EW corrections. 119
Figure 13.3. Theoretical uncertainties on the Z/γ transfer factors (left) nuisances related to the NLO-QCD re-weight + the mixing between QCD and EW corrections, (right) effect of the nuisance parameters related to NLO EW corrections. Solid (dashed) lines in (left) are showing the positive (negative) one sigma shift of the nuisance parameters for which the Z/γ can flip sign wrt the nominal value as a function of p_T. 120

Figure 13.4. Comparison between data and MC simulation for the Z/γ+jets ratio as a function of the hadronic recoil in the monojet in electron (left), muon (middle) and combined (right) channels respectively. The gray bands represent include both the systematic uncertainties and also statistical uncertainty in the simulation..... 122
Figure 13.5. Comparison between data and MC simulation for the Z(ℓℓ)/W(ℓν) ratio as a function of the hadronic recoil in the monojet in electron (left), muon (middle) and combined (right) channels respectively. The gray bands represent include both systematic uncertainties and also statistical uncertainty in the simulation..... 123
Figure 13.6. Comparison between data and MC simulation for the W($\ell\nu$)/γ+jets) ratio as a function of the hadronic recoil in the monojet in electron (left), muon (middle) and combined (right) channels respectively. The gray bands represent include both systematic uncertainties and also statistical uncertainty in the simulation..... 123
Figure 14.1. Comparison between data and prediction in dimuon (left) and dielectron (right) CR before and after the simultaneous CR-only fit. Ratio plots with the gray band shows individual uncertainty with all systematics per-bin. 125
Figure 14.2. Comparison between data and prediction in γ+jets CR before and after the simultaneous CR-only fit. Ratio plots with the gray band shows individual uncertainty with all systematics per-bin..... 126

Figure 14.3. Comparison between data and prediction in single muon (left) and single electron (right) CR before and after the simultaneous CR-only fit. Ratio plots with the gray band shows individual uncertainty with all systematics per-bin..... 126

Figure 14.4. Observed E_T^{miss} distribution in the monojet SR compared with the background expectations for various SM processes evaluated after performing a combined maximum likelihood fit to the data in all the control samples, but excluding the SR. Black curve show E_T^{miss} s distributions from FP DM model with M_ϕ = 1 TeV and M_χ = 400 GeV according to λ_u= 1. The gray bands indicate the post-fit uncertainty in the background prediction on the ratio plots. 128

Figure 14.5. Comparison between data and prediction in dimuon (left) and dielectron (right) CR before and after the simultaneous CR+SR background only fit. Ratio plots with the gray band shows individual uncertainty with all systematics per-bin. 130

Figure 14.6. Comparison between data and prediction in the γ+jets CR before and after the the simultaneous CR+SR background only fit. Ratio plots with the gray band shows individual uncertainty with all systematics per-bin..... 131

Figure 14.7. Comparison between data and prediction in single muon (left) and single electron (right) CR before and after the simultaneous CR+SR background only fit. Ratio plots with the gray band shows individual uncertainty with all systematics per-bin. 131

Figure 14.8. Observed E_T^{miss} distribution are compared for data and SM in the monojet SR with the background expectations for various SM processes evaluated after applying a combined maximum likelihood fit to the data in all the control samples, as well as in the SR. Black curve shows E_T^{miss} distributions from FP DM model with M_ϕ = 1 TeV and M_χ = 400 GeV according to λ_u= 1. The fit is performed assuming the absence of any signal. For the monojet SRs, ratio of data and the post-fit background prediction is shown. The gray bands are indicative of the post-fit uncertainty in the background prediction in the lower panel, ratio plots. 132

Figure 15.1. The observed and expected upper limit on the graviton production cross section. Green ($\pm1\sigma$) and yellow ($\pm2\sigma$) bands show the on the expected limits. Black solid line which is showing theoretical cross section for comparision. 134

Figure 15.2. The 95% CL observed and expected upper limits on ADD graviton production (left), as a function of fundamental Planck scale (M_D) for n = 2, where n is the number of extra spatial dimensions. The 95% CL expected and observed lower limits (right) on M_D as a function of n in the ADD model. Comparison between the results and previous ones obtained by the CMS Collaboration with data corresponding to an integrated luminosity of 19.7 fb^{-1} at a centre-of-mass energy of 8 TeV (blue points). 135

Figure 15.3. Reconstracted level jet p_T (left) and MET (right) distrubitons for varios M_ϕ and M_χ. 135

Figure 15.4. Comparison between offcial sample (blue line) and privately production sample (red line) for dirac DM M_ϕ = 1 TeV and M_χ = 400 GeV..... 137

Figure 15.5. 95% CL expected (black dashed line) and observed (red solid line) upper limits on $\mu = \sigma/\sigma_{th}$ for Dirac DM with the coupling strength parameter for the up quark corresponding to λ_u = 1 in the M_ϕ – M_χ plane. Constraints from the Planck satellite experiment are shown with the dark blue contours. DM is overabundant in the shaded area. 138

ABBREVIATIONS

ALICE	: A Large Ion Collider Experiment
AOD	: Analysis Object Data
ATLAS	: A Toroidal LHC Apparatus
CASTOR	: Centrauro And Strange Object Research
CERN	: Conceil Europeenne pour la Recherche Nucleaire
CMS	: Compact Muon Solenoid
CMSSW	: CMS SoftWare
CSC	: Cathode Strip Chamber
DAQ	: Data AcQusition
DBS	: Dataset Bookeeping System
DT	: Drift Tube
EB	: Barrel Electromagnetic Calorimeter
ECAL	: Electromagnetic CALorimeter
EE	: Endcap Electromagnetic Calorimeter
EMF	: Electromagnetic Energy Fraction
EWSB	: Electroweak Symmetry Breaking
FSR	: Final State Radiation
HB	: Barrel Hadronic Calorimeter
HCAL	: Hadronic CALorimeter
HF	: Hadronic Forward
HLT	: High Level Trigger
HO	: Outer Barrel Hadronic Calorimeter
ISR	: Initial State Radiation
JEC	: Jet Energy Correction
JER	: Jet Energy Resolution
JES	: Jet Energy Scale

JPT	: Jet Plus Track
L1	: Level-1 Trigger
LEP	: Large Electron Positron Collider
LHC	: Large Hadron Collider
LHCb	: Large Hadron Collider Beauty Experiment
LO	: Leading Order
LS	: Luminosity Section
MC	: Monte Carlo
PDF	: Parton Density Function
PF	: Particle Flow
PMT	: Photo Multiplier Tube
POG	: Physics Object Group
PS	: Proton Synchrotron
PSB	: Proton Synchrotron Booster
QCD	: Quantum Chromo Dynamics
RBX	: Readout Box
RECO	: RECOnstruction
RF	: Radio Frequency
RPC	: Resistive Plate Chamber
SM	: Standard Model
SPS	: Super Proton Synchrotron
SR	: String Regge
TEC	: Tracker End Cap
TIB	: Tracker Inner Barrel
TID	: Tracker Inner Disks
TOB	: Tracker Outer Barrel
TRIDAS	: Trigger and Data Acquisition System
TP	: Trigger Primitive

VPT	: Vacuum Photo-Trioder
ZDC	: Zero Degree Calorimeter
WLCG	: Worlwide Large Hadron Collider GRID
WLS	: Wave Length Shifting

1. INTRODUCTION

The existence of the Dark Matter (DM) was firstly theorized by Fritz Zwicky in 1930. While examining the Coma cluster in 1933, he calculated the gravitational mass of the galaxies within the cluster and obtained a value at least 400 times higher than expected from their luminosity, which means that most of the matter in the Coma cluster must be out of sight and can not measured (Zwicky and Rotverschiebung, 1933). Nowadays we know that according to modern cosmology, the universe consists of three basic parts: baryonic matter, DM and dark energy. According to this, a very large part of the universe is still not fully understood. Several theoretical models such as Extra Dimensions, Super Symmetry and DM have been developed to explain these observations. In this thesis, some of the DM models which are theoretical approaches to the above problem have been investigated experimentally. There are many models in the literature try to explain the existence of DM. Weakly Interacting Massive Particles (WIMP) model (Steigman and Turner,1985) is one of the most widely accepted ones. The purpose of this model is to determine the magnitude of the interaction between the Standard Model (SM) and DM particles. The methods used to understand the properties of DM are: direct determination, indirect determination and production of DM in collisions. It is predicted that accelerators such as the Large Hadron Collider (LHC) can form the DM and its properties can be measured. Since DM will not interact directly with detectors such as CMS, it will show itself as missing energy in the detector. This missing energy may be signature of DM and can be measured at the CMS in many different physical channels. One of these physical channels is the MonoJet + Missing Transverse Energy (E_T^{miss}) channel. In this channel DM is seen as missing energy and due to energy momentum conservation, this missing energy should be balanced by a jet. In this context, the one-jet events plays an important role especially in the DM researches. In this thesis DM candidates are investigated using data from the

CMS experiment at LHC. The aim of this thesis, is to investigate whether DM exist using single jet events and to determine its characteristics if it is found.

The present document is designed as follows. Chapter 2 presents a brief introduction to SM and SM events which is considered background to DM. Chapter 3 contains description of the experimental setup: CERN and the LHC are introduced. The CMS experiment is described in its various sub detectors in chapter 4. The CMS Monojet analysis, including comparisons with the expectations of some well motivated theoretical models, are explained in the chapter 5 and 6. The detail of the analysis is given through chapters 7 to 13 step by step. Data and simulation samples, trrigger performance and event selection criteria, background estimation and uncertainties are introduced in these chapters. The results and their statistical interpretation are presented in chapter 14 and 15. We conlude with chapter 16.

2. THEORETICAL OVERVIEW

2. 1. The Standard Model

The SM, formulated in the 1970s, is a basic and comprehensive theory of fundamental interaction and particles that explains the building blocks of matter, and also describes three basic types of interactions (strong, electromagnetic, and weak) (Salam, 1964). The SM is based on the $SU(3)_C \otimes SU(2)_L \otimes U(1)_Y$ symmetry group, which explains interactions between fundamental particles by means of the strong ($SU(3)_C$) and electroweak (EW) forces ($SU(2)_L \otimes U(1)_Y$). Colour charge, weak isospin and the hypercharge are represented with C, L and Y respectively in the symmetry group.

2.2. Particle Content and Interactions

The SM has elementary particles organized into the chart as shown in Figure 2.1. The particles of the SM are divided in two classes, fermions and bosons, which can be distinguished by their spin. Fermions behave according to the Fermi-Dirac statistics and have 1/2 spin. Bosons differ from fermions, which obey Bose–Einstein statistic. Interactions among particles in the SM are mediated though the exchange of spin-1 gauge bosons: the electromagnetic, the weak, the strong the force. The SM describes all these interactions except for the gravitational force because gravity is extremely weak. If it is compared to the other three interactions at small distances, so its effects are totally negligible in particle physics experiments.

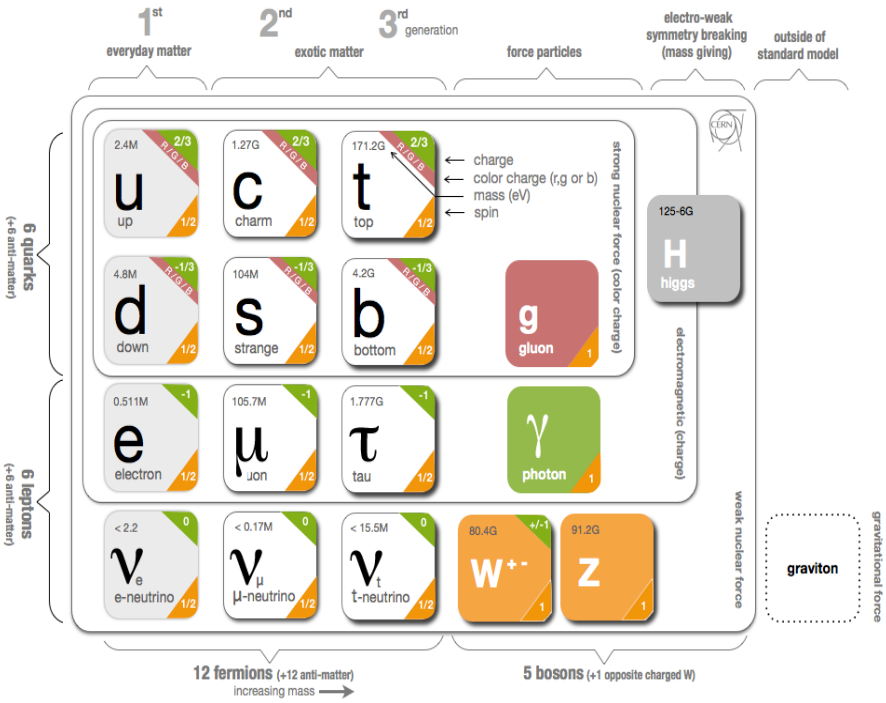

Figure 2. 1. Graphic representation of the particle content of the SM.

Fermions include all quarks and leptons. According to experimental observations, 12 physical fermions exist, 6 quarks (colour charged) and 6 leptons (colourless). There are 3 electrically charged leptons which are electron (e), muon (μ) and tau (τ) and three corresponding neutral which are electron neutrino (ν_e), muon neutrino (ν_τ) and tau neutrino (ν_μ), very light particles observed and do only attend the weak interactions. Leptons do not participate in the strong interaction. Three of the six observed quarks have an electrical charge of $+2/3e^+$ which are called up quark (u), charm quark (c) and top quark (t), the other three have a charge of $-1/3e^+$ and they are down quark (d), strange quark (s), bottom quark (b). Quarks take part in all three fundamental interactions included in the SM.

Six quarks and six leptons are organized in three generations, which are only differing in their mass. The first lepton generation is composed of the e and ν_e. The

second and third generations include the μ and τ as well as their corresponding neutrinos (ν_μ, ν_τ). The neutrinos are assumed to be massless within the SM. The first generation of quarks composed of the u and d quarks, while the second of c and s quarks. The last generation gather t and b quarks. As shown in Table 2.1, the fermion mass increases with the generation but the lifetime decreases except for c and b quarks because b quark has a longer lifetime with respect to the c quarks. All ordinary matter is consist of the first family of particles. The atoms of all chemical elements made up of electrons surrounding a nucleus of protons and neutrons which are a combinations of u and d quarks.

Table 2. 1. Properties of the spin-1/2 particles, the fermions (Tanabashi et al. 2018)

Quarks				**Leptons**		
Generation	**Name**	**Mass (GeV/c²)**	**Charge (*e*)**	**Name**	**Charge (*e*)**	**Mass (GeV/c²)**
1.	up (u) down(d)	2.4×10^{-3} 4.8×10^{-3}	2/3 −1/3	elektron(e) e-neutrino(ν_e)	−1 0	0.5×10^{-3} 0
2.	strange (s) charm(c)	0.1 1.27	−1/3 2/3	muon(μ) μ-neutrino(ν_μ)	−1 0	0.1 0
3.	bottom(b) top(t)	4.8 172.6	−1/3 2/3	tau(τ) τ-neutrino(ν_τ)	−1 0	1.7 0

Every particle has its own anti-particle with same mass but opposite charge with the corresponding particle. For example, the antiparticle of the electron is the positron and for all the other particles the antiparticle has the prefix "anti" in the name. Table 2.1 lists the elementary fermions of the SM and some of their properties.

Composite particles which are composed of several quarks, are called hadrons. All hadrons consist of either triple (qqq)or double quark ($q\bar{q}$) structures. All hadrons are colorless particles, and this is known as color confinement. The hadrons are classified into baryons and mesons. The proton and the neutron, which form the

nucleus, are made of the three quarks (uud, udd respectively) and they are both hadrons and baryons. They are all massive particles. There is another hadron family, called mesons which consists of a quark and antiquark. For example, a combination of π^0 meson is $(\frac{u\bar{u}-d\bar{d}}{\sqrt{2}})$.

The strong force is responsible for the quark interaction, leptons are not sensible to this interaction. It is mediated by the gluons which are massless spin 1 particles. The theory which describes the strong force is called Quantum Chromo Dynamics (QCD) and it is, mathematically a non-Abelian gauge theory.

Each quark carries a color charge: green, red and blue. The antiparticles of the quarks carry the anti-colour charges that are named anti-red, anti-green and anti-blue, in relevance to the choice for the names of the colour charges. The gluons carry both one color and one anticolor and have eight possible independent color-anticolor states.

The strong coupling constant is α_S which becomes weaker at higher energies. This property is responsible for the effect called the quark confinement. It explains why a quark cannot be observed as a free particle in nature. Quarks can either confine in three quarks or anti-quarks to constitute baryons, or in quark and anti-quark pairs to constitute mesons, as explained above.

The electromagnetic force is mediated by the photon and photon couples to electricaly charged leptons or quarks. It is defined in the SM by a quantum gauge theory called quantum electrodynamics (QED). It has infinite range. $W^{\pm}$ bosons as well as Z bosons are mediating the weak force, which acts on all fermions. The weak force is responsible for the β decay of radioactive nuclei. It also act a role in neutrino production in thermonuclear reactions inside the sun. Table 2.2 is of the described the spin-1 particles. Besides these five bosons, there is also Higgs boson which is the excitation of a so called Higgs field.

On 4 July 2012, two of the experiments at the LHC, CMS and ATLAS, reported that they found a new particle with a mass of about 125 GeV/c^2 which is

about 133 proton masses (Chatrchyan et all, 2012c). It is well consistent with the Higgs boson. It was later verified to be the searched Higgs boson which gives the SM particles their rest mass.

Table 2. 2. Properties of the spin-1 particles, the four gauge bosons of the SM (Tanabashi et al. 2018)

Force	Name	Charge (*e*)	Mass (GeV/c^2)
Electomagnetic	Photon(γ)	0	0
Weak	W boson($W^{\pm}$)	1	80.4
Weak	Z boson(Z^0)	0	91.2
Strong	gluon(g)	0	0

2.3. Beyond the Standard Model

Although SM explains very well the interactions of fundamental particles with each other, it still cannot answer some unknowns. Therefore, the SM is not a complete theory of nature. The so called Beyond the Standard Model (BSM) theories explains the theoretical developments needed to explain the shortcomings of the SM. The following physical phenomena points various of shortcomings of the SM:

- Gravity is not included in the SM .
- The hierarchy problem, which essentially relates the huge discrepancy between the electroweak force, on the order of 10^2 GeV and Planck scales around 10^{19} GeV.
- SM only explains about 5% of the energy present in the universe but it does not explain the rest of the universe. According to cosmological observations it should be dark energy and DM. There is strong astrophysical evidence that shows non-baryonic DM accounts for 26% of the energy density of the universe. Since this DM particles are only sensitive to the weak and

gravitational interactions, they are called WIMPs. Cosmological observations also show that the universe has an accelerated expansion. Which leads to the introduction of a mysterious dark energy, composing about 69% of our universe.

- There are also questions about the three generations of fermions. Why are there three generations?
- The reason why the matter and anti-matter in the universe is not equal, is one of the important questions to be asked. The SM cannot estimate completely the observed level of strong CP-violation.

2.3.1. History of Dark Matter

DM plays a leading role in our understanding of modern cosmology. But in spite of its importance we still know relatively little about its interesting history. According to the SM of cosmology, the content of the universe is comprised of three different types of energy/matter as shown in Figure 2.2. About 5 percent is composed of visible matter, is known as baryonic matter for example planets, stars, nebulae, dust, rocks and gas, as described in the SM of high energy physics. About 69 percent is the so-called dark energy and the remaining 26 percent is DM (Planck Collaboration., 2016).

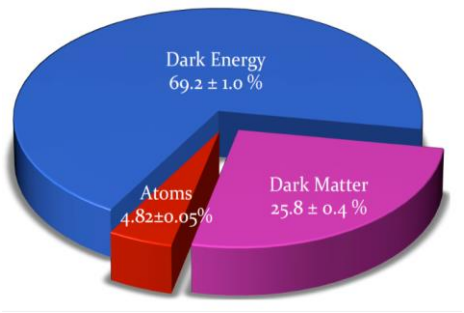

Figure 2. 2. Chart representation of composition of Universe (Planck Collaboration., 2016)

The existence of DM was suggested about 100 years ago by astronomers and is based on some credible astronomic measurements: First evidence was found by Fritz Zwicky who measured different velocities of objects in the Coma cluster in the 1933's (Zwicky and Rotverschiebung, 1933). He applied the virial theorem to the Coma Cluster and got proof of unseen mass. He examined its mass based on the motions of galaxies near its edge and compared to its luminosity and number of galaxies. He calculated roughly that the mass of this cluster had about 400 times more mass than was visually observed.

In the 1960s–1970s, Vera Rubin and Kent Ford obtained additional strong evidence using galaxy rotation curves. They observed different spiral galaxies and also measured orbital speeds of stars with regard to their distance r to the galactic center (Rubin et al., 1980). The stars at the outside of the galaxy were moving as fast as the ones in the middle which is not consistent with Newtonian gravitational theory. The results indicate a constant mean velocity $v(r)$ for radi r in the outer regions as shown Figure 2.3. This is in contradiction to the expectation of a decreasing rotational velocity.

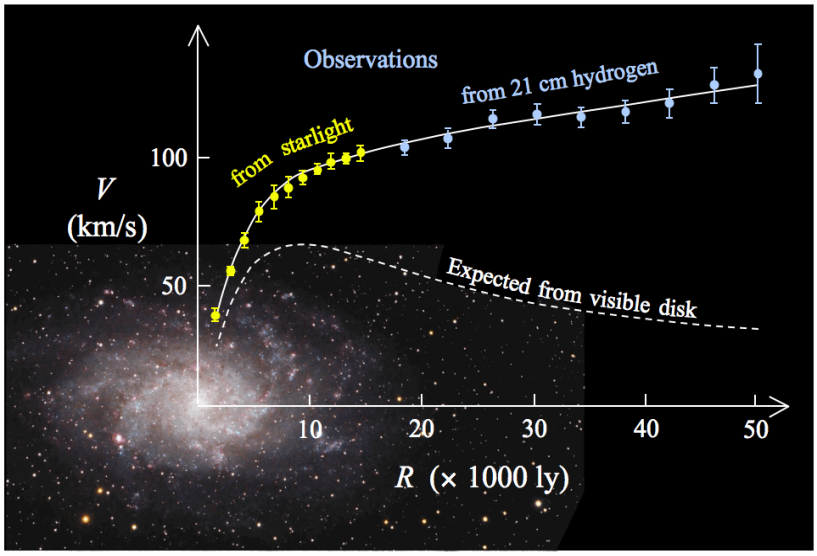

Figure 2. 3. Astrophysical evidence for Dark Mater.

Observations of the Cosmic Microwave Background (CMB) and gravitational lensing effect are another evidence for DM. Gravitational lensing effect is where light is deflected by the curvature of space-time because of heavy objects such as galaxies. This effect is described in Einstein's Theory of Relativity. This makes the illusion of seeing the distant object in an optical ring around the lens. The existence of DM can explaine gravitational lensing effect (Massey and Kitching, 2010). A picture pointing so-called arcs because of gravitational lensing can be seen in Figure 2.4.

Figure 2. 4. Hubble Space Telescope in Abell 1689 indicates the existence of DM. Gravitationel lensing effects can be seen.

The Bullet cluster, which is located in the constellation Carina and is the result of the collision of two clusters of galaxies that happened 150 million years ago, is shown in Figure 2.5. The blue overlay which is deduced from gravitational lensing is highlighted and it is hinting the existence of DM while the red overlay highlights X-ray emission due to hot gasses (Graham et al., 2015). The study of this

collision started in August 2006 and indicated one of the strongest proofs of the existence of DM.

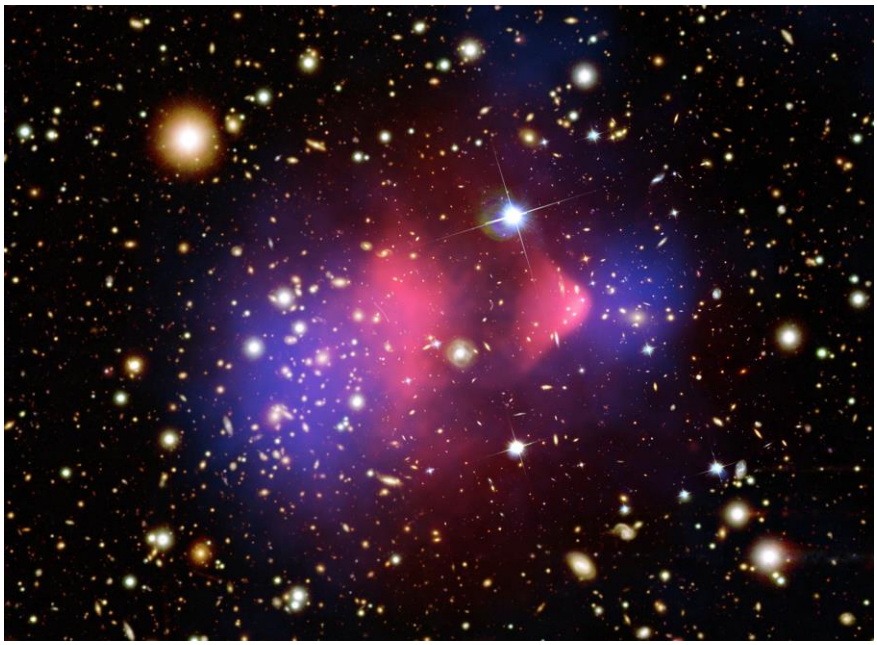

Figure 2. 5. The Bullet Cluster is photographed via the Hubble Space Telescope. The mass distribution deduced from gravitational lensing is highlighted by the blue overlay, while the red overlay highlights X-ray emission as observed by the Chandra telescope X-ray: NASA/CXC/CfA/ (Markevitch et al., 2006).

Dark Matter Properties: While its presence supported with a number of astrophysical observations, DM has never been directly observed. Because it does not emit radiations or interact electromagnetically with matter. Moreover, the DM is not in the form of dark sector of normal matter. If so, then we could detect it due to absorption of radiation passing through them. It is also not in the form of antimatter since we do not see any special gamma radiations due to matter-antimatter annihilation (NASA,2006).

2.3.1.1. Weakly Interacting Massive Particles

The Weakly Interacting Massive Particles (WIMPs) which is a candidate of a DM, was originally introduced by Steigman & Turner (1985). They interact with matter by gravity and the weak nuclear force, but not by the electromagnetic or the strong nuclear force. Their mass is in the range of 100 GeV to 1 TeV and they are assumed to be much heavier than the known SM particles. The neutralino is an example of a WIMP candidate, which is the supersymmetric partner of the neutrino.

At the beginning of the universe, particles were produced as thermal relic and the WIMP density parameter is calculated under the following assumptions. SM particles and WIMPs were in thermal balance in the beginning of universe. When the universe temperature T dropped below the DM mass M_χ, the number of WIMP started decreasing as $e^{-\mathrm{m}\chi/\mathrm{T}}$. However, its abundance did not drop to zero because of the concomitant expansion of the universe. This process orginally caused a decrease of the rate of annihilation of DM into SM particles. The WIMPs abundance then got to a constant value (freeze out), as explained in more detail in (Hooper, 2010). The expected WIMP relic density can be approximated by:

$$\Omega_\chi h^2 \cong \frac{3.10^{-27} cm^3 s^{-1}}{\langle \sigma_A v \rangle} \tag{2.1}$$

where $\langle \sigma_A v \rangle$ is the thermal averaging of the DM annihilation cross section σ_A and the relative velocity v of the interacting WIMPs.

2.3.2. Experimental Dark Matter Searches

There are three possible ways of detection of WIMP (see Figure 2.6):

- measurement of DM-Nucleon cross section (direct detection)
- anhilation products of DM (indirect detection)
- production of DM (collider searches)

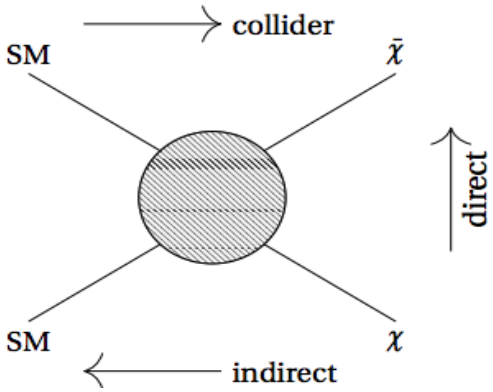

Figure 2. 6. Illustration of different DM detection methods.

2.3.2.1. Direct Detection

In direct detection experiments, physicists measure the interaction of a DM particle with the nuclei of the detector material, which is caused by the recoil of DM from SM matter. Namely, it refers to the investigation of the effects of a WIMP-nucleus collision as the DM passes over a detector in an Earth laboratory. Examples for such a search are XENON (Aprile et al., 2012), DAMA/LIBRA (DAMA/LIBRA Collaboration, 2018) and the LUX experiments (Akerib et al., 2014).

2.3.2.2. Indirect Detection

Experiments which measure the production of SM matter (neutrinos, gamma rays, positrons, antiprotons and their antiparticles) caused by the annihilation of two DM particles are called indirect detection experiments. IceCube (Aartsen et al, 2018. IceCube Collaboration.) neutrino detector is very famous experiment about indirect DM detection.

2.3.2.3. Collider Searches

Another way to search is to produce a DM pair at collider experiments. Interaction of two SM particles producing two DM particles are performed in the CMS (Sirunyan et al., 2018) and ATLAS (Aaboud et a, 2016) experiments at the

LHC. In the following, two approaches are presented in collider DM searches studied at LHC: The Effective Field Theory (EFT) approach and The Simplified model approach.

2.3.3. EFT for Dark Matter at Collider Searches

EFT is a strong and economical method to describe physical processes happening at a given energy scale with regards to a tower of interactions, involving only the degrees of freedom present at such scale. (Simone and Jacques, 2016), (DiFranzo et al, 2013). It is one of the approaches used in DM research at colliders as a parameterisation of missing energy in data analysis. If DM is created alongside with one or more energetic SM particles, then the P_T of visible transverse momentum will not be zero, indicating the existence of particles invisible to the detector, such as DM, neutrinos or long-lived undetected particles. The force of the interaction is ruled by an energy scale M_* taken to the convenient power for an operator. EFTs are a reasonable definition of DM interactions with the SM, if the interactions are outside the kinematic access of the collider by a heavy particle. In EFT approach, each operator and energy scale explain a range of processes, according to the direction of the arrow of time in Figure 2.7.

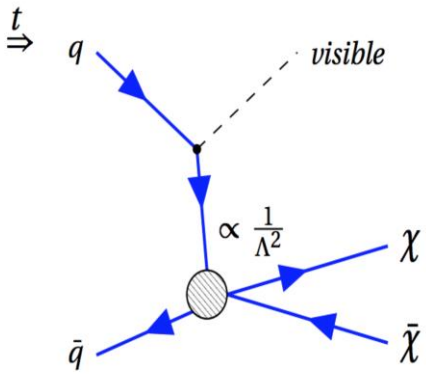

Figure 2. 7. Illustration of an EFT interaction between DM and the SM.

2.3.4. Simplified Models

Simplified model approach is more complicated than the EFT approach and is based on a larger number of assumptions. In general, the simplified models of DM have five free parameters: Mass of the DM particle χ defined by M_{χ}, the mass of the mediator particle M_{med}, and the two couplings of the mediator which are the coupling to the DM particles g_{χ}, coupling to quarks g_{q} and the mediator width Γ_{ϕ} (Abercrombie et al, 2015). The coupling g_{q} is assumed to be universal to all quarks. It is also possible to consider other models where mixed vector and axialvector couplings are considered, for instance the couplings to the quarks are axial-vector whereas those to DM are vector (Abdallah et. al, 2016).

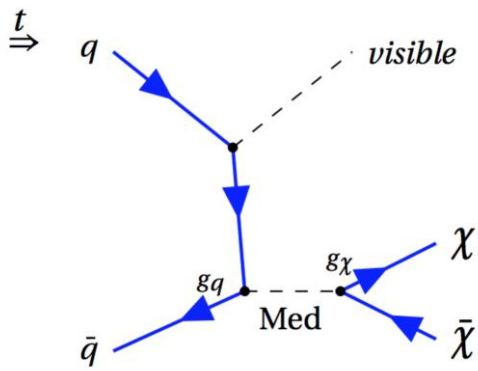

Figure 2. 8. Collider production of DM in terms of a simplified model approach.

Here, a pair quarks produces a particle which is detectable (marked by "visible" in the Figure 2.8, e.g. Z boson) and also a heavy mediator, which is denoted by "Med". The mediator then decays into two DM particles χ and $\overline{\chi}$. The coupling strength of DM to the mediator particle is denoted by g_{χ}, the coupling strength of the mediator particle to the quarks is denoted by g_{q}. Further parameters are the mass of the mediator particle typically denoted by M_{med} and the mass of the DM particle M_{χ}.

Simplified DM model approach is the better choice to develop the model-independent paradigm. The generality of existing studies in the literature have the mediator particle couples to two DM particles at the same time: Higgs portal (Shrock and Suzuki, 1982), axion-portal (Nomura and Thaler, 2009), 2HDM portal (Bai, 2013), Z′-mediated (Cheung and Yuan, 2007), gravity-mediated (Lee, Park, and Sanz, 2013) and dilaton-assisted (Bai, Carena and Lykken, 2009). In this thesis, we study simplified DM models with SM fermions as the portal particle, which we call Fermion Portal DM which will be discussed in more details in section 6.

3. CERN AND THE LARGE HADRON COLLIDER

The LHC is a ring accelerator desinged to collide protons and heavy ions with center of mass energy of 14 TeV although so far operateded at 7, 8 and now operating at 13 TeV. The accelerator complex is located at the European Organization for Nuclear Reserch (CERN) near Geneva, on the border between Switzerland and France. It is a hadron-hadron collider situated roughly 100 m underground and installed in a 27 km long circular tunnel which is used for LEP Collider until 2000. LHC is a collaboration over 100 countries established to test and verify the SM of particle physiscs, in particular to study the Higgs Boson, and find any hints of new physiscs.

LHC uses two beam pipes surrounded by superconducting magnets to accelerate counter-rotating proton beams. Proton beams are obtained by stripping electrons from hydrogen atoms, injected into the LHC from a long chain of pre-accelerators which starts out with linear accelerator (LINAC2). They are accelerated to 50 MeV at LINAC2 before reaching the Proton Synchrotron Booster (PSB). Here protons reach 1.4 GeV and are injected to Proton Synchrotron (PS) that in turn accelerates them to an energy of 25 GeV. Then as a last pre-acceleration step, the proton beams are further accelerated up to 450 GeV in the Super Proton Synchrotron (SPS). At the end, proton beams are transferred to the LHC and accelerated to the energy of 7 TeV per beam. A sketch of LHC accelerator complex is shown in Figure 3.1 and a short summary of the accelerator chain and corresponding beam energies in each of the different acceleration steps is given in Table 3.1

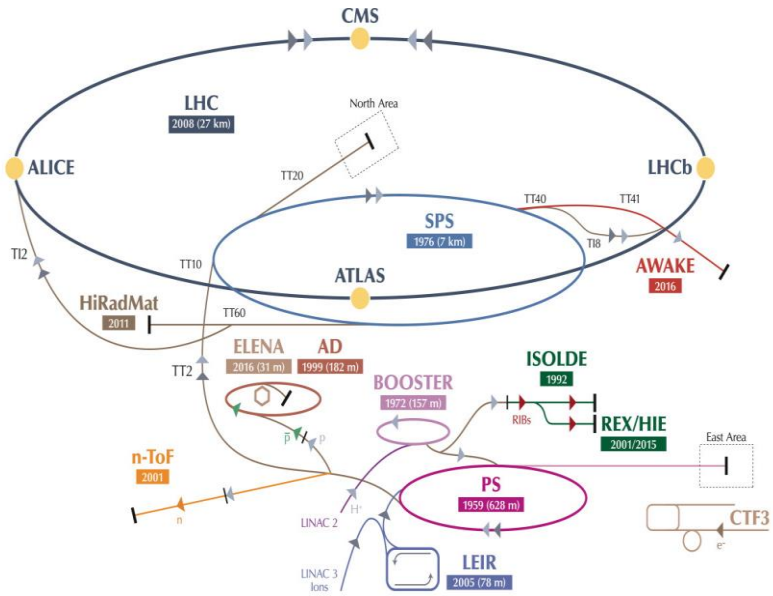

Figure 3. 1. Overview of the Accelerator chain. The LHC is the last ring in a complex chain of particle accelerators. Proton injector chain is LINAC2 → Booster → PS → SPS (Cern accelerator complex)

Table 3. 1. Accelerator chain and corresponding beam energies.

Accelerator	**Injection Energy**	**Final Energy**
LINAC2	750 keV	50 MeV
PSB	50 MeV	1.4 GeV
PS	1.4 GeV	26 GeV
SPS	26 GeV	450 GeV
LHC	450 GeV	7 TeV

LHC's construction was completed in 2008 and first beams were observed on September 2008 in an inaugural commissioning run. In the first set of years of continuous data taking, which was called LHC Run I ((March 2010 to February 2013), the center-of-mass energy was constant at 7 TeV for 2010 and 2011 and LHC

delivered L=45 pb^{-1} and L= 6.1 fb^{-1} of data respectively. Then energy was increased to 8 TeV for 2012 and 23.3 fb^{-1} data was collected from the CMS experiment. The time between consecutive colliding proton bunches, so called bunch spacing, was fixed to 50 ns. The time during the first Long Shutdown (LS1- February 2013 to April 2015) was utilized to upgrade certain parts of accelerator and detectors and carry out necessary repairs. The LHC Run II started in 2015 (from April 2015 through 2016) with an increased energy of 6.5 TeV per beam and delivered L= 4.2 $fb^{-1}$of the data by the end of 2015, finally it started to operate at a center-of-mass energy of 13 TeV, and a bunch spacing of 25 ns. In 2016 and 2017 LHC continued operating at $\sqrt{s}$=13TeV. The integrated luminosity and beam energy of the LHC for proton-proton collisions for different years of the operation is shown in Figure 3.2.

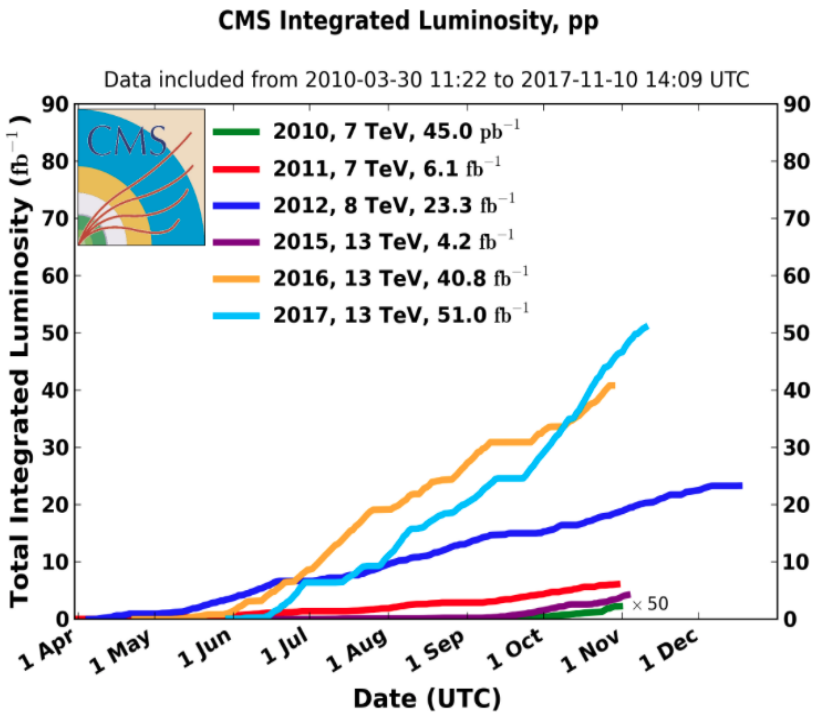

Figure 3. 2. Comparison between total integrated luminosity delivered to CMS during proton-proton stable beams collisions in different spans of LHC operation.

The measurement reported in this dissertation is based on data collected by the CMS detector from the LHC proton-proton collisions in 2016 at $\sqrt{s}$=13TeV. The LHC delivered 40.82 $fb^{-1}$of collision data during the 2016 run, 37.76 $fb^{-1}$of these were recorded by the CMS experiment and approximately 35.9 $fb^{-1}$of collision data passed quality tests and were approved for analyses. Official luminosity report for 2016 data taking is shown in Figure 3.3. This figure indicates the difference between the delivered luminosity and the recorded luminosity. The correction is due to the efficiency of the detectors.

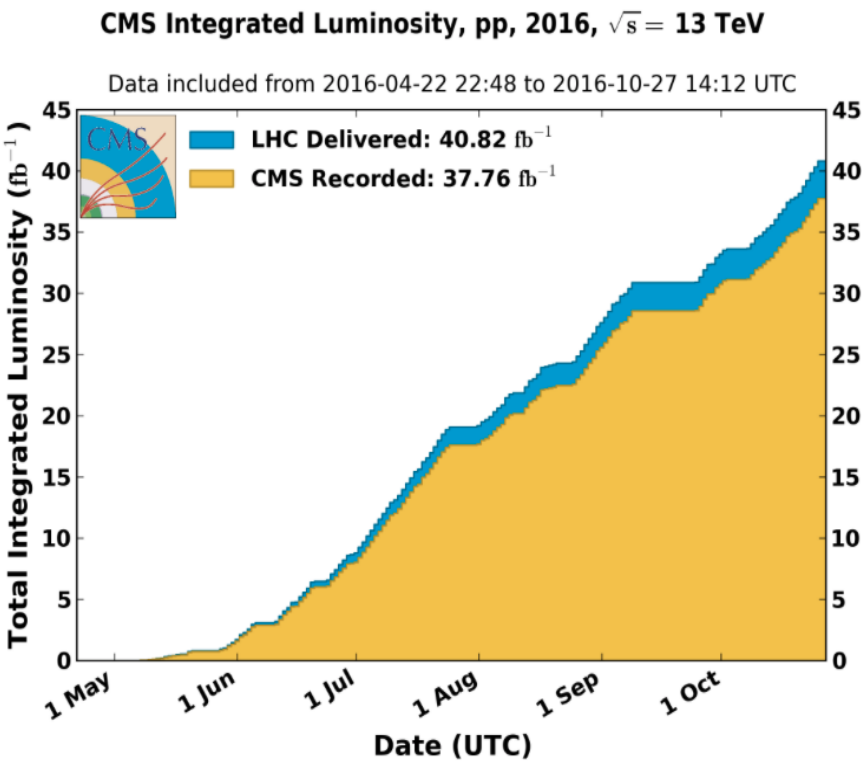

Figure 3.3. Official luminosity report for 2016.

3.2. Luminosity and Machine Parameters

To study physics processes at the TeV scale, LHC must be able to accelerate particles at high energy and, at the same time, provide a very high rate of interaction - luminosity. The design luminosity of the LHC is 10^{34} $\mathrm{cm}^{-2}\mathrm{s}^{-1}$. Accelerating protons with very short bunch crossing interval (25 ns or 40 MHz) and the high number of proton bunches (2808 per beam, each made of 1.15×10^{11} protons) in the LHC allows to reach a design peak luminosity. This high luminosity is important to compensate for the low cross section of the studied processes. The cross section and event rate in proton-proton collisions as a function of the center-of-mass energy is shown in Figure 3.4.

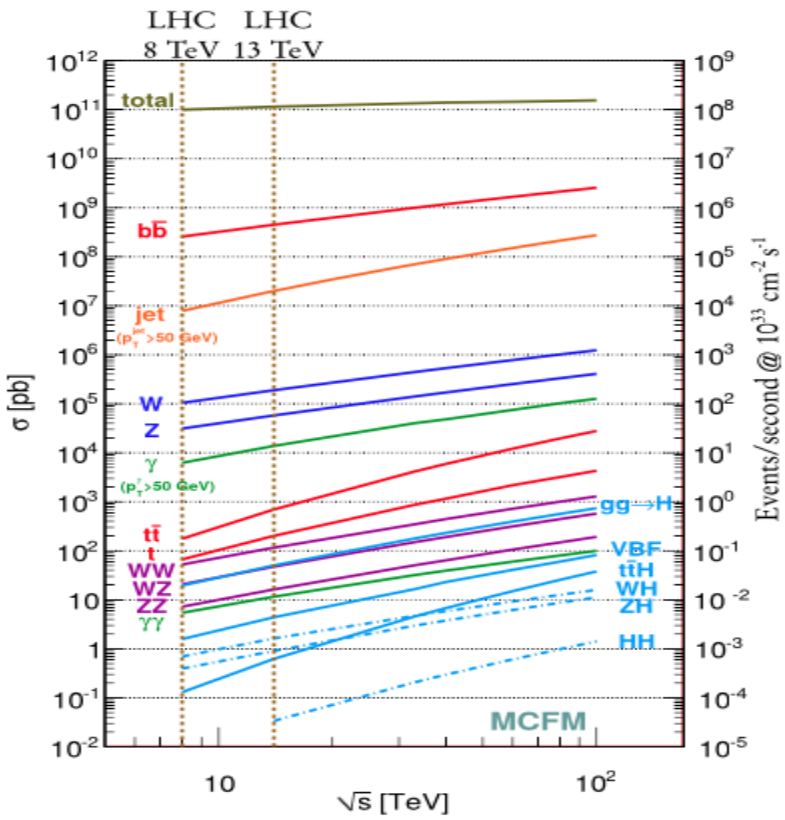

Figure 3. 4. The cross section and event rate as a function of the center-of -mass energy for a value of the luminosity $L = 10^{33}\,\mathrm{cm}^{-2}\,\mathrm{s}^{-1}$.

Figure 3.4 indicates the expected energy dependence of the total cross section. In this figure left scale shows some physics processes which have much smaller cross sections, while the right scale is the event rate of the physics processes at a typical luminosity of $10^{33}\,\mathrm{cm}^{-2}\mathrm{s}^{-1}$.

The cross section σ of a physical process determines the event rate R according to the Equation 3.1,

$$R = L\sigma \tag{3.1}$$

where L is the instantaneous luminosity. σ is the cross section which represents the number of collisions per unit of time and Luminosity can be characterized as in Equation 3.2,

$$L = \frac{\gamma f k_B N_p^2}{4\pi\varepsilon_n\beta^*}F \tag{3.2}$$

where γ is the Lorentz factor, f is the revolution frequency, k_b is the number of bunches, N_p is the number of protons per bunch, ε_n is the normalized transverse emittance.

The variables describing the interaction point are the betatron function β^* and the geometric luminosity reduction factor F (CERN/LHCC 2006-001).

The most important parameters of the LHC collider are summarized in Table 3.2.

Table 3. 2. The machine parameters related to the LHC detectors.

		pp	HI	
Energy per nucleon	E	7	2.76	TeV
Dipole field at 7 TeV	B	8.33	8.33	T
Design Luminosity	L	10^{34}	10^{27}	$cm^{-2}s^{-1}$
Bunch seperation		25	100	ns
Number of bunches	k_B	2808	592	
Number of particles per bunch	N_p	1.15 x10^{11}	7.0 x10^{7}	
Collisions				
β-value at IP	β^*	0.55	0.5	m
RMS beam radius at IP	α^*	16.7	15.9	μm
Luminosity lifetime	τ_L	15	6	hr
Number of collisions/crossing	n_c	≈ 20	$-$	

3.3. The LHC Experiments

There are four main experiments that are located at the collision points of the LHC. These detectors are ATLAS (A Toroidal LHC ApparatuS), CMS (Compact Muon Solenoid), LHCb (LHC beauty) and ALICE (A Large Ion Collider Experiment). Figure 3.5 shows the schematic layout of the LHC and the location of the four main experiments.

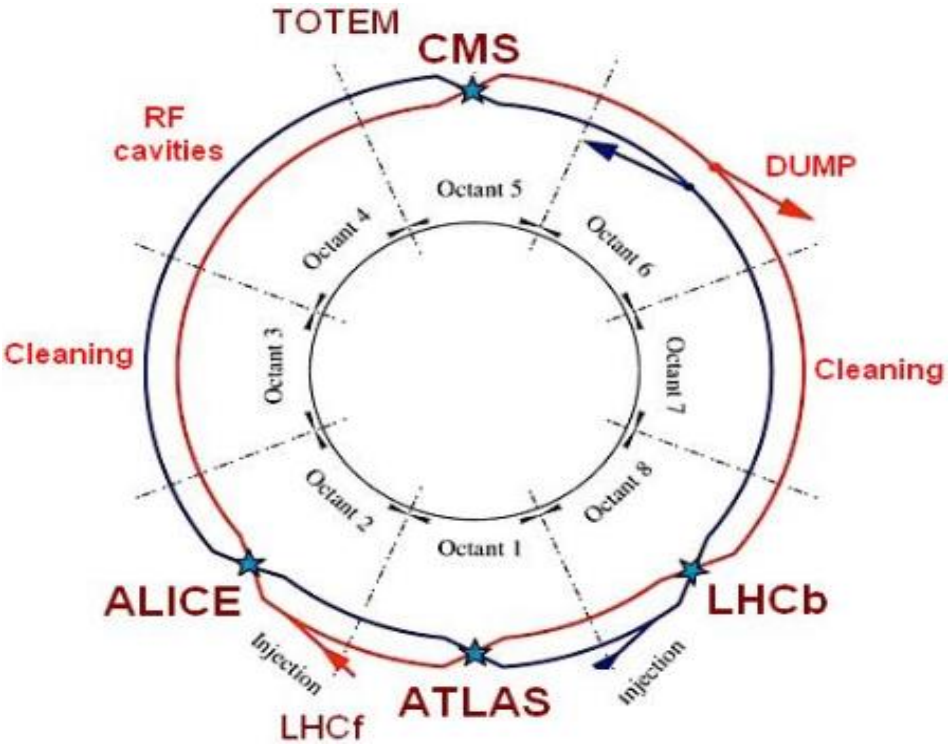

Figure 3. 5. The LHC and experiments schema.

CMS is one of the two multi-purpose experiments at the LHC together with ATLAS. These two detectors are designed for the Higgs boson and BSM physics searches. LHCb is specifically dedicated to *b*-physics and Charge Parity (CP) violation while ALICE is specialized to search for quark gluon plasma in remnants of heavy ion collisions. There also exist two smaller LHC experiments namely TOTal Elastic and Diffractive Cross Section Measurement (TOTEM) and Large Hadron Collider forward (LHCf). These experiments focus on forward particles. Lastly, near the LHCb there is Monopole and Exotic detector (MoEDAL) that will search for the magnetic monopole. CMS experiment will be described in more detail in the next chapter while the other six experiments namely ATLAS, ALICE, LHCb, LHCf, TOTEM and MoEDAL will be mentioned only briefly.

ALICE : ALICE is a general-purpose, heavy-ion detector which is designed for the high-multiplicity environment of *Pb–Pb* collisions (Aamodt et al., 2008). The aim of this detector is to study the confinement of the quarks via Quark-Gluon Plasma created in heavy ion collisions and investigating QCD processes. ALICE composes of a central barrel part which measures electrons, hadrons and photons, and a forward muon spectrometer which measures muons emitted in the forward region. Its overal sizes are 16×16×26m with a total weight of about 10.000 t.

ATLAS: ATLAS is the largest volume collider detector ever built, measuring 44 m in length, 25 m in diameter and weighing 7000 metric tonnes (Aad et al., 2008). It is designed to search for both SM and BSM physics processes. Detector has the toroidal shaped magnet system that provides a homogeneous magnetic field inside the torus. ATLAS is divided into four main parts: the inner detector (ID) which consist of three subdetectors namely the pixel and silicon-strip (SCT) tracker and the transition radiation tracker, calorimeter - which encloses the ID and the solenoidal magnet - and consist of two detectors: namely electromagnetic calorimeter and hadronic calorimeter. Muon spectrometer which is the largest component of the ATLAS integrates four detector subsystems: monitored drift tube (MDT), CSC, Resistive Plate Chamber (RPC), thin gap chambers (TGC), and magnet system. The basic design criteria of ATLAS can be summarized as follows:

- High-P_T lepton-momentum tracking efficiency, identify electron and photons, *t*-leptons and heavy-flavours, and provide full reconstruction capabilities of full events at lower luminosities.
- Very good electromagnetic calorimetry to measure and identify electron and photons.
- Very effective hadron calorimetry to identify jet and missing transverse energy measurements.
- Very efficient muon system to measure the properties of muon.

LHCb: The LHC beauty experiment is a forward spectrometer, it covers $2 < \eta < 5$ pseudorapidity region and provide an opportunity to study heavy flavour physics at the LHC (Alves et. al., 2008). Its main aim is to search indirect evidence of new physics in CP violation and rare decays of beauty and charm hadrons.

LHCf: LHC forward is a small experiment which consist of two detectors (Arm1 and Arm2) and is built inside the ATLAS underground cavern 140 m off the interaction point 1 (IP1) of LHC (Aaij et al., 2015). It is dedicated to measurements in the very forward region and will allow to test and tune the hadronic interaction models used by ground-base cosmic ray experiments.

TOTEM: The TOTEM is a small experiment, located at the LHC Interaction Point (IP) 5 together with the CMS experiment, and is dedicated to the measurement of the total proton-proton cross-section using a luminosity independent method, elastic scattering and diffractive processes (Anelli et al., 2008). TOTEM consist of three detectors namely T1, T2 and Roman Pots (RPs). T1 and T2 are trackers positioned close to the CMS end caps and measure particles escaping the IP at the medium angles. RPs are silicon detectors placed symmetrically on both sides of the crossing region and measurement of elastic proton-proton scattering is accomplished by these detectors.

MoEDAL: MoEDAL is the latest experiment located at Interaction Point 8 (IP8) along with the single arm forward LHCb detector at the LHC (Pinfold et al., 2009). It provides Magnetic Monopole and other highly ionizing Stable (or pseudo-stable) Massive Particles (SMPs) searches at the LHC.

4. COMPACT MUON SELONOID

The CMS (Compact Muon Selonoid) is a multi-purpose detector located at Point 5 on the LHC accelerator complex and positioned at approximately 100 m underground in Cessy, France (Chatrchyan et al, 2010). It is one of the biggest experiments ever constructed with the overall dimensions 21.6 m in length, 14.6 m in diameter, and 14000 tonnes in mass. It was designed to investigate proton-proton collisions at high center-of-mass energies and luminosities. One of the primary motivation to build the CMS detector was to study the mechanism of electroweak symmetry breaking. Another aim was to verify existence of Higgs Boson (which was confirmed in in 2012) and the other goal was to discover physics BSM. To reach the purposes of the LHC physics plans the detector requirements for CMS can be summarised as follows:

- Very efficient inner tracking system to reconstruct the secondary vertices of particle decays and estimate charged particle trajectories.
- Good electromagnetic energy resolution and also good diphoton and dielectron mass resolution with wide geometric coverage ($|\eta| < 2.5$), and efficient photon and lepton isolation at high luminosities.
- Good missing transverse energy and dijet mass resolution with a large hermetic geometric coverage ($|\eta| < 5$).
- Good muon identification and momentum resolution, to precise measurements of charged particle momenta (Chatrchyan et al., 2008).
- Good trigger system.

The CMS has a hermetic cylindrical shape with multi-layered onion structure and each layer is designed to measure the momentum and energy of specific particles. A schematic layout of the CMS detector is given in Figure 4.1.

The CMS detector conceptuallyconsists of 2 regions: the central region where $\eta < \sim 1$, also called the barrel of the detector, and the endcap region $\eta < \sim 1.2$. The sub-detectors of the CMS from the innermost to outermost parts are Inner Traker System, Electromagnetic Calorimeter, Hadronic Calorimeter, Solenoid and Muon System. In addition, the trigger system is developed to process and store only interesting events for physics analysis.

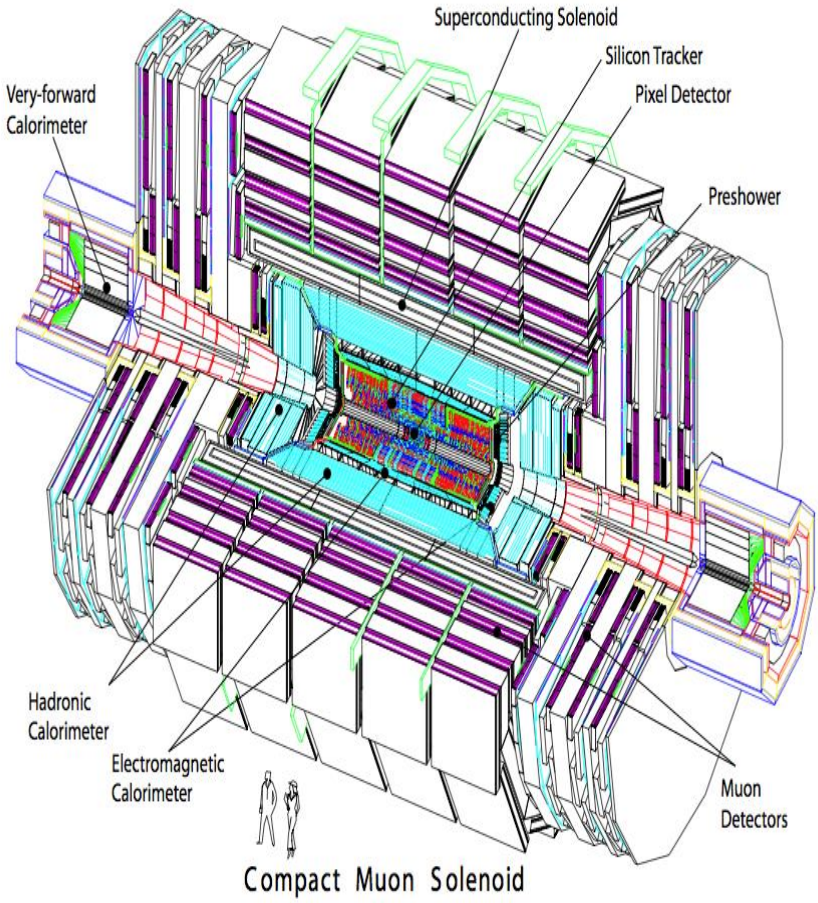

Figure 4. 1. Perspective view of the CMS detector and its components (Bayatian et al., 2006).

Silicon tracking detector is the innermost part of the CMS. It measures the charged particle's momentum in the magnetic field. The tracker is surrounded by the ECAL which measures the energy of electrons and photons. Behind the ECAL, HCAL absorbs hadrons and measures their energy. The tracker and both calorimeters are inside a solenoid magnet that generate a 3.8 T magnetic field. The coil of the superconducting solenoid magnet surrounds the inner subdetectors. Muon detector system is located outside the magnet and it tracks and measures the momentum of muons. Figure 4.2 shows trajectories of different particles as they pass through the detector.

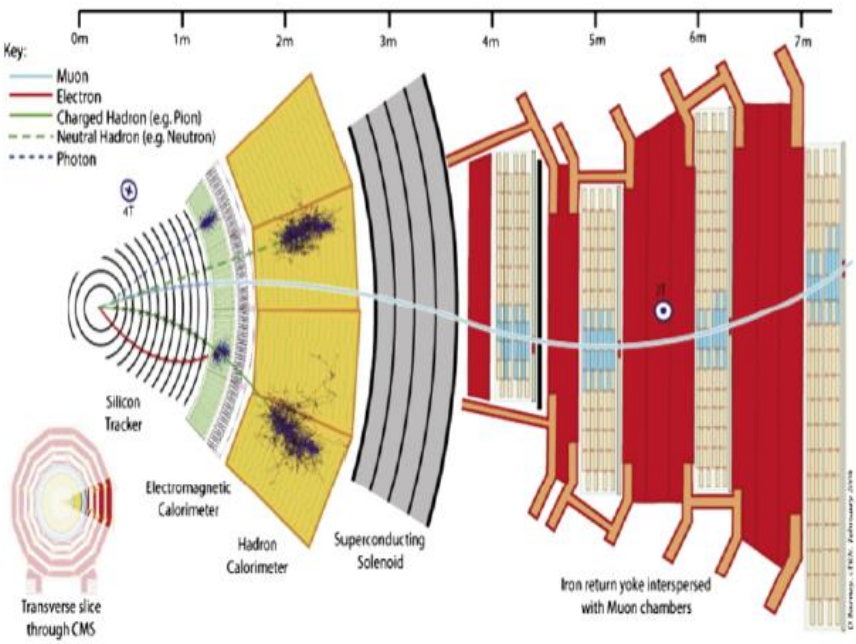

Figure 4. 2. A slice of the Compact Muon Solenoid detector.

CMS Coordinate System: CMS uses a right-handed coordinate system which is oriented such that the *x*-axis points south to the centre of the LHC ring, the *y*-axis points vertically upward, and the *z*-axis points in the anticlockwise proton beam direction. In the *x*-*y* plane the azimuthal angle ϕ is measured from the *x*-axis

while the radial coordinate in this plane is stated by R. CMS coordinate system is given in Figure 4.3.

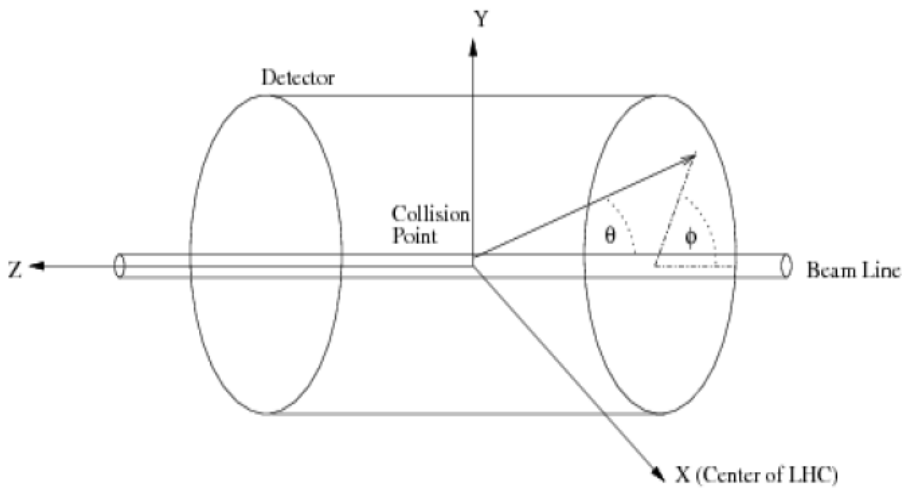

Figure 4. 3. Schematic view of the CMS coordinate system.

In CMS a spherical coordinate system (r, ϕ, θ) is commonly used. Instead of the θ we use the pseudo-rapidity η which is defined as:

$$\eta = -ln tan\left(\frac{\theta}{2}\right) = \frac{1}{2} ln\left(\frac{|p|+p_z}{|p|-p_z}\right) \tag{4.1}$$

where θ is polar angle, p is momentum and $p_z = pcos\theta$ is the z component of the momentum.

Another commonly used measure is the angular distance (ΔR) between two objects and it can be given as:

$$\Delta R = \sqrt{(\Delta\eta)^2 + (\Delta\phi)^2} \tag{4.2}$$

In the following part, a description of the different subdetectors and their capabilities will be given.

4.1. Tracker

The Tracker is the innermost subdetector and is closest to the beam line around the interaction point (Bayatiyan et al., 1998). It is designed to measure precisely the momentum of the charged particles and provide a high momentum resolution and a high efficiency in the range of $\eta < 2.4$. Primary and secondary vertices identification and charged particle's reconstruction is also performed by the CMS tracker. The tracker system has a cylindrical shape of 5.8 m long and a diameter of 2.5 m as shown in Figure 4.4. It comprises of two sub part, the silicon pixel and the silicon strip detector.

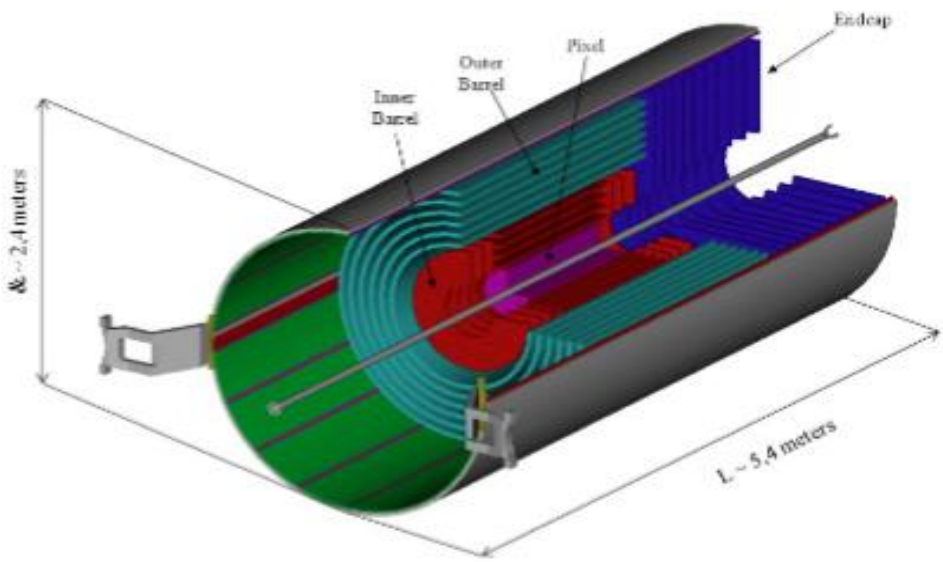

Figure 4. 4. Schematic view of the CMS tracker detector with its components: The Pixel Barrel and the Strip sections, Inner Barrel, Outer Barrel and Endcaps.

Since the tracker is closest to the IP it is subject to both large particle fluxes but also to highly energetic particles and intense potential radiation damage. For this reason the material must be stable enough to run in this environment. To build the tracker detector, two different technologies have been employed:

- **Pixel technology** has been used due to the innermost part needs to be more granular, resistant to radiation and providing a better position resolution.
- **Silicon strip** has been used because at a larger distance from the interaction point, the requirements on occupancy and radiation hardness are less stringent, thereby making silicon strips the most cost-effective solution.

4.2. Pixel Detector

The pixel detector as shown in Figure 4.5 is the first layer of the tracker system and is situated closest to the beam pipe. The innermost pixel detector covers a range of $2.5 < \eta < 2.5$. It is made of silicon semiconductor sensors which are connected to pixelated readout chips (ROCs). The pixel has three barrel layers at radius of 4.4 cm, 7.3 cm and 10.2 cm called Barrel Pixel (BPIX) and has two endcap disks on each side of the barrel called Forward Pixel (FPIX) which are located at distances of ±32.5 cm and ±46.5 cm from the collision point. It also has 1440 modules with 66 million hybrid pixel sensors. Each module has 16000 readout chips. The total number of pixels or readout channels is 45×10^6. The cell size of the pixel detector is $100 \times 150\ \mu m^2$ and in total the pixel detector covers an area of about $1m^2$.

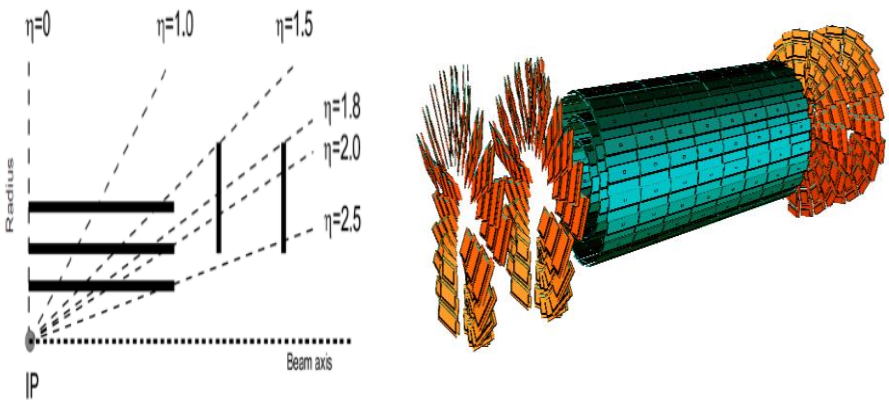

Figure 4. 5. Geometrical layout of pixel detectors in the CMS tracker (Chatrchyan et. al, 2010).

The pixel detector is surrounded by the silicon stripe tracker starts where the particle density is decreased.

4.3. Silicon Strip Detector

The pixel is encircled by silicon strip tracker with 10 barrel detection layers extending outwards to a radius of 1.1m. Silicon strip trackers are composed of 9.6 millions silicon strip sensors and four modules namely the TIB, TOB, TID and TEC. Schematic overview of the CMS tracker detector in the *r*-*z* plane is illustrated in Figure 4.6. The figure shows all four components. The pixel detector is shown in red while strip detector layers are marked in blue. The nominalmcollision point is indicated by a star. TIB and TID occupy the space $r < 55$ cm and $|Z| < 118$ cm. The barrel is composed of four layers of silicon strip modules in the TIB and the three layers in each disk. The TOB which incorporates six modules, covers $r > 55$ cm and $|Z| < 118$ cm while TEC covers the region $124 < |Z| < 282$cm. Each of the endcaps consists of nine disks with seven concentric rings of silicon strip modules per disks.

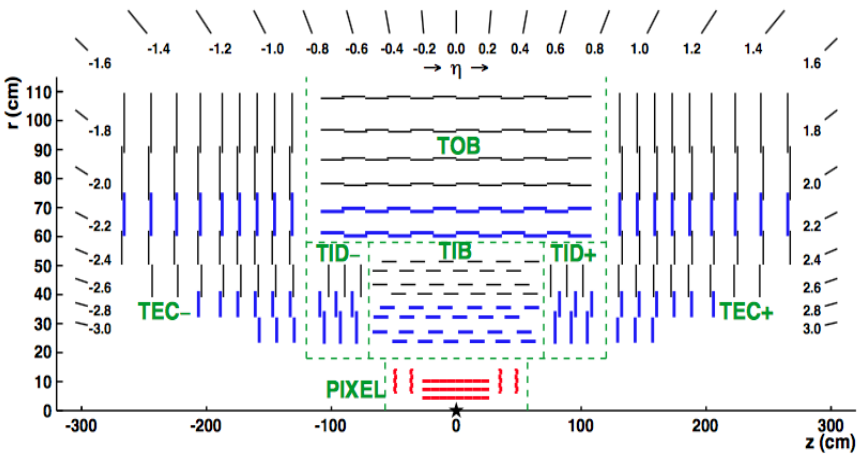

Figure 4. 6. Schematic cross section of the CMS tracker in the *r*-*z* plane (The CMS Collaboration, 2014,. *JINST* 9 P10009).

A summary of the principal characteristics of the various tracker subsystems is given in Table 4.1. In this table locations indicate the region in r (Z) taken up by each barrel (endcap) system.

Table 4. 1. The principal characteristics of the tracker (The CMS Collaboration, 2014,. *JINST* 9 P10009).

Tracker subsystem	**Layers**	**Pitch**	**Location**
Pixel tracker barrel	3 cylindrical	$100\times150\mu m^2$	$4.4 < r < 10.2$cm
Strip tracker inner barrel (TIB)	4 cylindrical	$80-120\mu m$	$20 < r < 55$cm
Strip tracker outer barrel (TOB)	6 cylindrical	$122-183\mu m$	$55 < r < 116$cm
Pixel tracker endcap	2 disks	$100\times150\mu m^2$	$34.5 < \lvert Z \rvert < 46.5$cm
Strip tracker inner disks (TID)	3 disks	$100-141\mu m$	$58 < \lvert Z \rvert < 124$cm
Strip tracker endcap (TEC)	9 disks	$97-184\mu m$	$124 < \lvert Z \rvert < 282$cm

4.4. CMS Calorimeters

Calorimeters absorb the particle's kinetic energy by creating particle cascades, and provide a signal that is proportional to the deposited energy. The energy resolution of calorimeters depends on the number of particles in the cascade, therefore the energy of the particle can be given as:

$$\left(\frac{\sigma_E}{E}\right)^2 = \left(\frac{a}{\sqrt{E}}\right)^2 + (b)^2 + \left(\frac{c}{E}\right)^2 \tag{4.3}$$

where a is the stochastic term related to shower development and detector's response, b is the constant term specified by the calibration and uniformity of the crystal, and c is the noise term which comes from electronics.

The CMS calorimeter system composes of two diferrent subsystems namely the ECAL which is designed to measure the energies of electromagnetically interacting particles and HCAL which measures the neutral or charged hadrons. Figure. 4.7 shows the locations of the ECAL and HCAL (quarter slice-longitudinal cross section) in and around the CMS magnet.

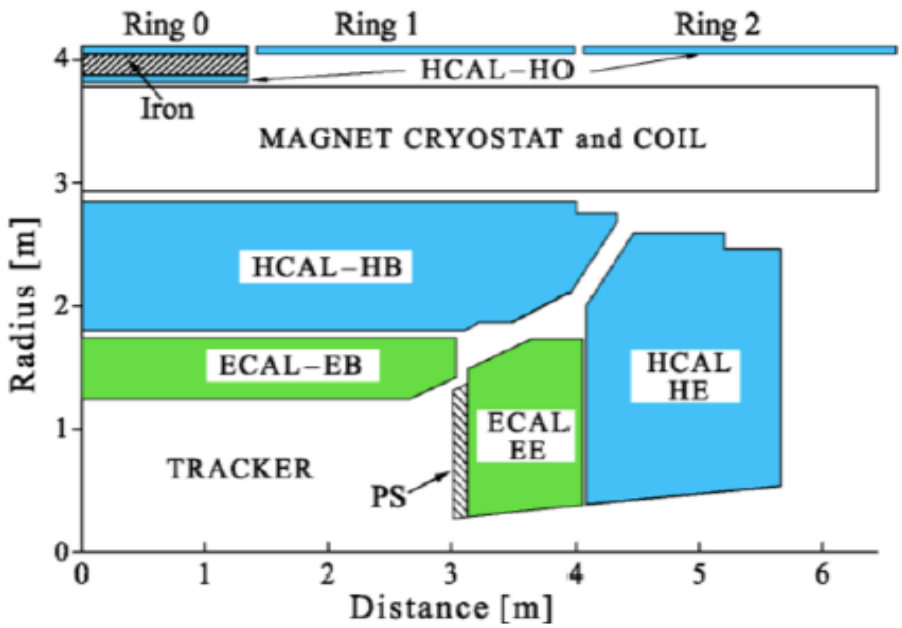

Figure 4. 7. Schematic view of the ECAL and the HCAL detectors in and around the CMS magnet (Abdullin et. al., 2009).

4.4.1. Electromagnetic Calorimeter

The Electromagnetic Calorimeter (ECAL) is located around the tracker and inside the solenoid system (Bayatian et. al, 1997a). It is designed to measure the energy of electrons and photons with a high resolution. The ECAL is a hermetic and homogeneous $PbWO_4$ crystal calorimeter. It uses 75848 scintillating $PbWO_4$ crystal. $PbWO_4$ has a short radiation length (X_0 = 8.8 mm) and small Moliere radius (R_M = 22 mm) and it is a very fast scintillator with 80% of light signal being emitted in 25 ns which is the time between two bunch crossings at the LHC. This feature of

ECAL makes the calorimeter to offer the best performance for energy resolution since most of the energy from electrons or photons is deposited within the homogeneous crystal volume of the calorimeter. ECAL plays an important role in the study of the physics of electroweak symmetry breaking, large variety of SM and other new physics processes as well as for the search in the two photon decay channel of the Higgs boson. The coverage of the ECAL ranges to a pseudorapidity up to $|\eta| = 3.0$ and is divided into a barrel ECAL region (EB), covering $|\eta| < 1.479$, and an endcap ECAL region (EE), covering $1.479 < |\eta| < 3$ as shown in Figure 4.8.

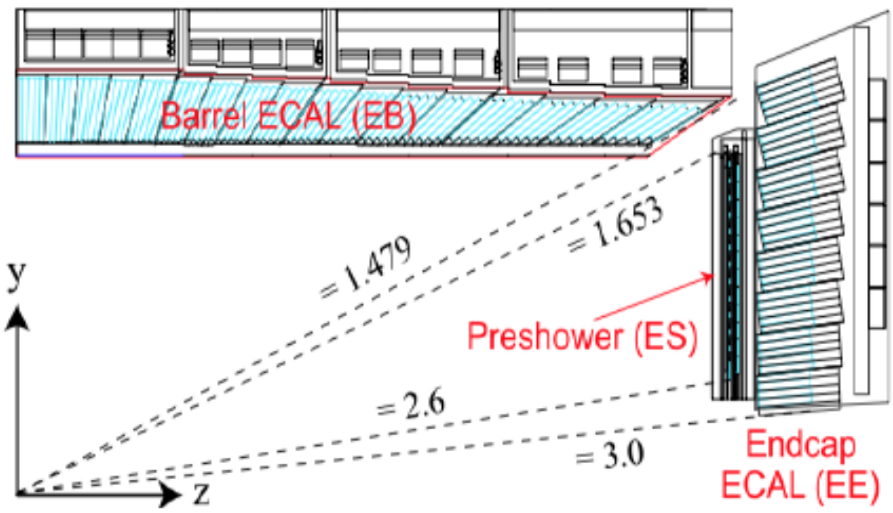

Figure 4. 8. One-quarter schematic cross sectional view of the CMS electromagnetic calorimeter (Bayatian et al., 2006).

4.4.1.1. Electromagnetic Barrel

The Electromagnetic Barrel (EB) covers the pseudorapidity range $\eta < 1.479$. It is divided in two halves. Each halve has 18 supermodules containing 1700 crystals. The EB crystals have a length of 230 mm, which corresponds to approximately 26 radiation lengths. In EB the scintillation light is collected by avalanche photo diodes (APD) that are able to provide gain in the existence of the high transverse magnetic field.

4.4.1.2. Electromagnetic Endcap

The Electromagnetic Endcap (EE) covers pseudorapidity regions of $1.479 < |\eta| < 3.0$. Due to the high radiation levels all materials used in this region must tolerate very large doses and neutron fluences, for this reason the APDs have been replaced by the less efficient, but more resistant vacuum phototriodes (VPT). The crystals are grouped into supercrystals of 5×5 and installed at a distance of 315.4 cm to the interaction point. Each endcap consists of two large halves so called *Dees* consisting of 3662 identical shaped crystals.

4.4.1.3. Preshower Detector

The Preshower (ES) is installed in front of the EE within the the range of $1.653 < |\eta| < 2.6$. It is a cylindrical shape detector with 0.18 m length and with a total 1850 kg weight. ES is a sampling calorimeter consisting of two layers of lead radiator and silicon strips. Its main goal is to measure the position of electromagnetic showers, and identify neutral pions as well as to improve the discrimination of electrons against minimum ionizing particles. All subdetectors of ECAL are shown in Figure 4.9.

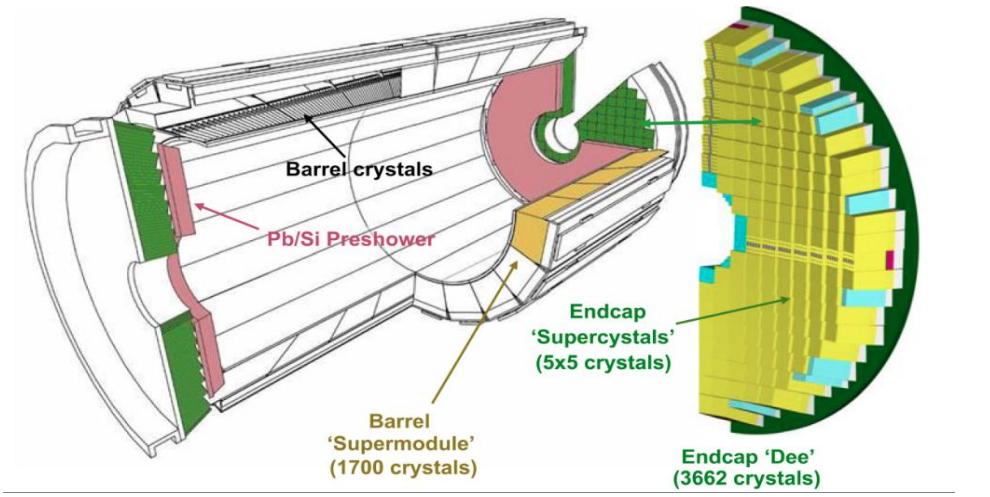

Figure 4. 9. Sketch of the electromagnetic calorimeter: EB, EE and preshower Calorimeter.

4.4.2. Hadron Calorimeter

The main aim of the Hadronic Calorimeter (HCAL) is to measure the hadron jets and other hadronic fragments, from the proton-proton interaction (Bayatian et al, 1997b). It is designed to provide good resolution for dijet events and plays very important role in the measurement of the missing transverse momentum. Additionally HCAL allows the indirect detection of weakly interacting particles by measuring the missing energy.

Because heavy particles (like hadrons) can not be stopped in ECAL, long lived hadrons such as kaons, pions are mostly detected by HCAL. HCAL is a sampling calorimeter that consists of absorber plates for showering and scintillators as the active material. There are 16 layers of absorbers made from brass. The absorber depth of the HCAL corresponds to a minimum of 5.8 radiation lengths. The scintillating tiles are made from plastic and their thickness is 3.7 mm. As shown in Figure 4.10, the HCAL consists of four sections, the hadron barrel (HB), the hadron endcap (HE), hadron outer (HO) and the hadron forward (HF) calorimeters.

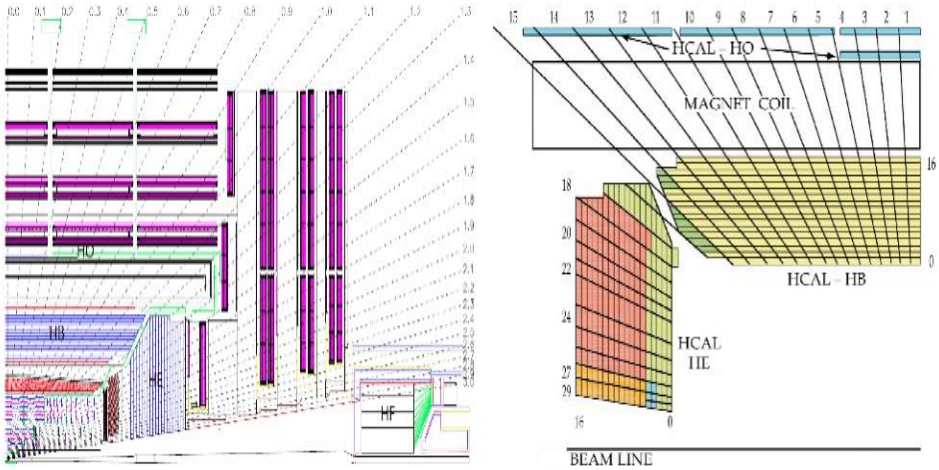

Figure 4. 10. Left: The different HCAL components in the CMS detector. Right: Longitudinal segmentation of the HCAL towers in the central part of the detector.

4.4.2.1. Hadron Barrel

The HB covers pseudorapidity range of $|\eta| < 1.4$ and contains 15 brass plates. It is divided into 2304 segments called "towers", each covering 0.087 in $\Delta\phi$ and $\Delta\eta$. The barrel consists of two halves, HB+ and HB− that are composed of 36 wedges. Each wedge is segmented into four azimuthal angle (ϕ) sectors and contains brass alloy absorber plates and 16 layers of active plastic scintillator tiles located in between the stainless steel and brass absorber plates. The innermost and outermost plates are made of stainless steel for structural strength. The scintillation light is collected by wavelength-shifting fibres and guided by optical cables to hybrid photodiodes (HPDs) (Bayatian et al., 2006).

HB is contained between ECAL and the magnet, for this reason maximization of absorber material is very important for detection of the complete hadronic showers. Since the HB alone can not provide a sufficient containment for hadron showers in the central pseudorepidity region, the hadron calorimeter is extended outside the solenoid by addition of extra scintillator layers called the HO calorimeter.

4.4.2.2. Hadron Outer

The HO covers $|\eta| < 1.3$ and located in the barrel region, It is embedded in the muon system, outside of the solenoid magnet. Its main goal is to measure the energy leakage from the HCAL and ECAL. HO increases the thickness of the calorimeter system to about 10 hadronic interaction lengths. It is composed of arrays of scintillator located outside the magnet coil and includes five rings. The rings are identified by the numbers −2, −1, 0, +1, +2. The numbering increases with *z* and the nominal central *z* positions of the five rings are respectively −5.342 m, −2.686 m, 0, +2.686 m and +5.342 m. At $\eta = 0$, HB has the minimal absorber depth. Therefore, the central ring (ring 0) has two layers of HO scintillators while other rings have a single HO layer (Chatracyan et al., 2008). Each ring of the HO is divided into 12 identical ϕ sectors and each sector has 6 slices in ϕ.

4.4.2.3. Hadron Endcap

The HE is a sampling calorimeter located inside the CMS magnet, covers the region $1.3 < |\eta| < 3.0$ and has a depth of about 10 interaction lengths. It overlaps with the HB in tower 16. The tower size in HE is the same as for HB till $|\eta| < 1.74$ while for the higher η region, the tower sizes are increasingly enlarged to a maximal $\Delta\eta \times \Delta\phi$ size of 0.350×0.174. HE is consist of absorber plates alternated with scintillator disks. The scintillation light is collected by wavelength shifting (WLS) fibres and photo detectors, multipixel hybrid photodiodes (HPD) are used, because of low sensitivity to magnetic fields and their large dynamical range.

4.4.2.4. Hadron Forward

The HF Calorimeter is in the forward region of the CMS in 11.2 m distance from the interaction point. It covers the pseudorapidity region $3 < |\eta| < 5$ which is very important for heavy Higgs, SUSY and low-x QCD s-earches. The HF's main goal is to detect and identify events that produce forward jets. It also improves the determination of the missing transverse energy. Since HF is very close to the beam and experiences an extreme particle flux, it has to be extremely radiation hard. HF is composed of steel absorbers and radiation hard quartz fibers with a fast collection of the emitted Cherenkov light within the fibres. There are two different types of fiber that are used in HF namely Long (1.65 m) and short (1.43 m) quartz fibers. They are placed separately and carry signal from the photo multiplier tubes (PMT). When incoming particles interact with the atomic nuclei of the absorbers, secondary particles are created. Electrically charged particles pass the quartz fibers and cause the emission of Cerenkov light. Then the fibers redirect the produced light to PMT, which extract the signal.

HF also has tower geometry. There are 13 towers in η, all with a size given by $\Delta\eta \approx 0.175$, while the lowest-η towers with $\eta \approx 0.1$and the highest-η towers with $\eta \approx 0.3$.

4.5. Muon System

Muons hardly lose energy when transversing the detector, for this reason muons are able to penetrate the calorimeters and reach the outer part. As the middle name of the experiment indicates, muons are a signature of many searches for new physics and detection of them are very significant for CMS physics analyses especially for ZZ decay channel in the Higgs analysis, with ZZ further decay to four muons. The muon detector is primarily important for muon identification (Bayatian et al. 1997d). The information which comes from the muon system are also used in the trigger system of the CMS. The time resolution for all muon subdetector systems is about 3 ns, providing excellent trigger capabilities. The muon system is located outside the solenoid magnet and covers the pseudorapidity region $|\eta| < 2.4$. It is the largest subdetector at the CMS and provides 25000 m^2 of active detection plane. Due to the shape of the solenoid, the system has a cylindrical Barrel section and two planar Endcap regions. In the barrel section of the CMS, drift tubes (DT) are used in the endcap regions and cathode strip chambers (CSC) as well. Both of these detectors make it possible to measure the trajectories of muons passing through the detector and therefore, together with the information from the inner tracking system, the muon tracking system provide an accurate measurement of the muon momentum. DT and CSC are complemented by Resistive Plate Chamber (RPC). These three different systems are gaseous detectors. Their measurement principle is based on creating a strong electric field in a cell filled with gas. The gas is ionized at the path of the particle, and turn into ions, then ions are accelerated, and start an avalanche of charged particles. The avalanche is finally detected as an electric signal. In Figure 4.11 cross sectional view of the CMS muon system is shown. In total, there are 1400 muon chambers including 250 DTs, 540 CSCs and 610 RPCs.

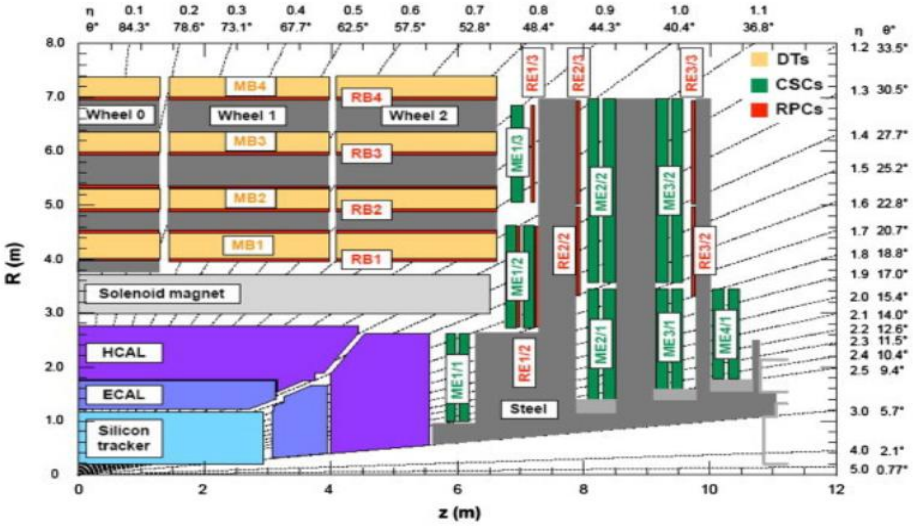

Figure 4. 11. Design overview of the CMS muon system. Drift tubes, cathode strip chambers, and resistive plate chambers are indicated.

4.5.1. Drift Tube Chambers

The DTs are located in the barrel region of the detector where the track density and the residual magnetic field is low. It has dimensions of $13\times42\text{mm}^2$ of cross sectional area and provides a very high reconstruction efficiency for muon hits. DTs cover a pseudo rapidity of $|\eta| < 1.2$and consists of four concentric stations around the beam line. The three inner stations have 60 drift chambers while outer station has 70 chambers. The stations are segmented in the azimuthal angle into twelve sectors. Along the *z*-axis there are five wheels namely YB/$+2,+1,0,-1,-2$. In each of the 12 sectors of the yoke there are 4 muon chambers per wheel, labeled MB1, MB2, MB3, and MB4 as shown in Figure 4.12.

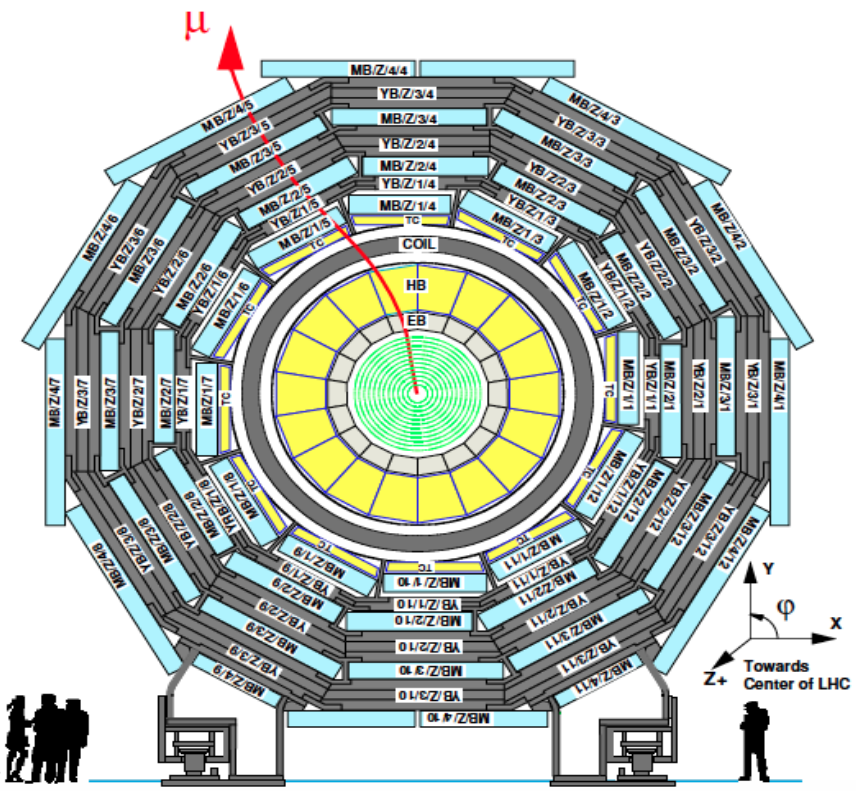

Figure 4. 12. Layout of the CMS barrel muon DT chambers in one of the 5 wheels (Chatrchyan et al., 2008).

DT chamber is made of 3 (or 2) super layers (SL) which is the smallest independent unit of the design. Each is made of four layers of rectangular drift cells staggered by half a cell. There are about 172 000 sensitive wires. The wires in the two outer SLs are parallel to the beam line and supply a track measurement in the magnetic bending plane (r-ϕ) while in the inner SL, the wires are orthogonal to the beam line and measure the z position along the beam. The SL is not present in the fourth station.

4.5.2. Cathode Strip Chambers

The CSCs are placed in the endcaps of the detector covering a pseudo rapidity region of $1.2 < |\eta| < 2.4$ where the muon rate, the neutron-induced background and the magnetic field is large. Muon endcaps are made of 468 CSCs and each consists of four stations with chambers, labeled ME1, ME2, ME3 and ME4 as shown in figure 4.13.

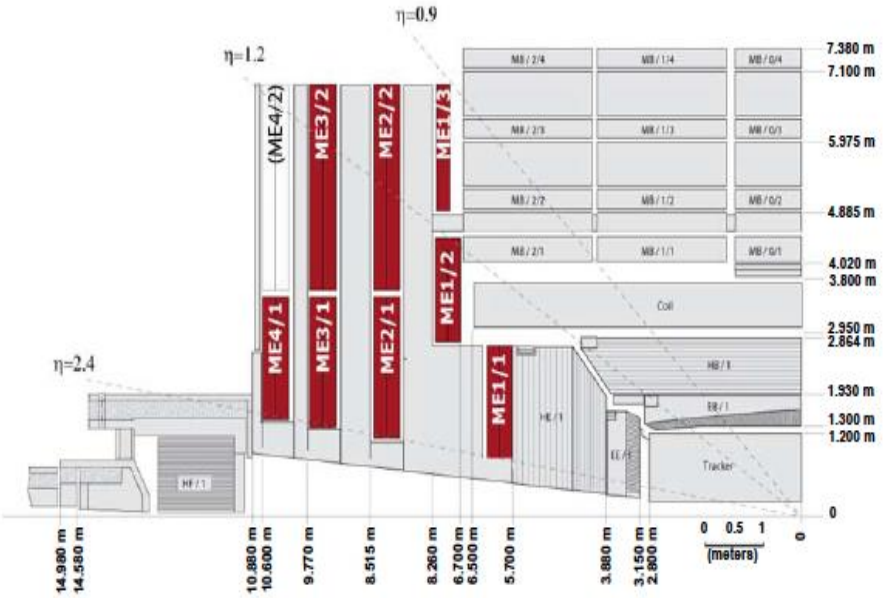

Figure 4. 13. Longitudinal view of one quarter of the detector. Cathode strip hambers of the Endcap Muon system are highlighted (Chatrchyan et al., 2008).

Each Endcap region consists of four disks. The inner most disk has three rings of chambers, while the other three disks are comprised of two rings of chambers. Each ring is segmented into 18 azimuthal sections, except the outer ring which has 36 chambers.

4.5.3. Resistive Plate Chambers

The RPCs are gaseous parallel-plate detectors installed in both regions of the detector to provide complementary trigger information and a very precise timing measurement of a muon (much smaller than 25 ns). The Barrel region has 480 RPC modules while the endcaps have 432 RPC modules. RPCs cover the pseudorapidity region $|\eta| < 1.6$ and are made of two parallel plates separated by a 2 mm gas volume and covered with a 2 mm resistive Bakelite plate, as shown in Figure 4.14.

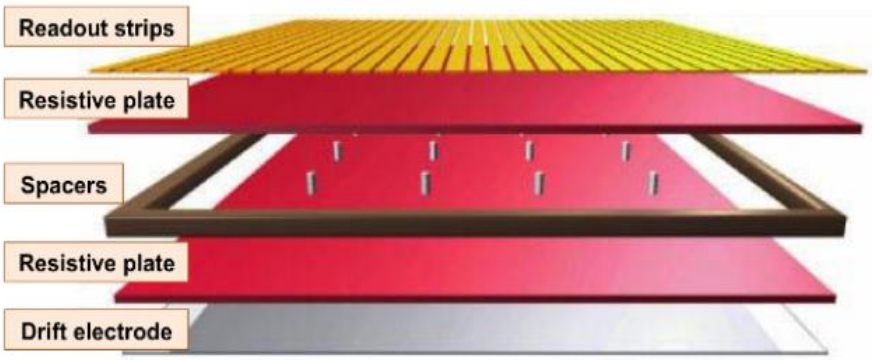

Figure 4. 14. Schematic view of a RPC chamber.

4.6 Magnet

CMS has an enormous super conducting selonoid magnet as shown in Figure 4.15 (Bayatian et al, 1997c). The superconducting solenoid sits between the HCAL and the muon system and is designed to generate an uniform 4T magnetic field. Its main goal is to bend the particles‘ direction coming from the high energy collisions. The total weight of magnet system is 12000 tonnes and It has a diameter of 6 m and a length of 12.5 m.

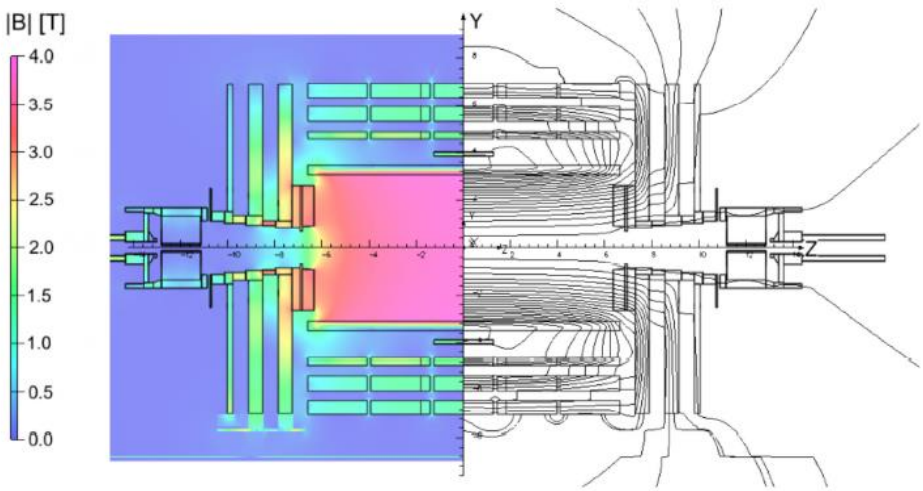

Figure 4. 15. Magnetic field map (left) and field lines (right) predicted for a longitudinal section of the CMS by a magnetic field model at a central magnetic flux density of 3.8 T. Each field line represents a magnetic flux increment of 6 Wb (Chatrchyan et al., 2013).

At full magnetic field, the magnet contains a stored energy of 2.6 GJ. To get this high field, magnet runs at 19.1 kA current. The principal parameters of the CMS solenoid magnet is given in Table 4.2.

Table 4. 2. The main characteristics of the CMS solenoid magnet.

Magnetic length	12.5 m
Cold bore diameter	6.3 m
Central magnetic induction	3.8 T
Nominal Current	19.14 kA
Inductance	14.2 H
Stored Energy	2.6 GJ
Operating temperature	1.8 K
Yoke magnetic induction	1.8 T

4.7. Trigger and Data Acquisition System

The CMS Trigger and DAQ (Data Acquisition) system collects and analyses the detector information at the 40 MHz LHC bunch crossing frequency (Bayatian et al., 2000b). DAQ system operates the Detector Control System (DCS) for the operation, and controls all detector components for the experiment (Bayatian et al., 2000a). LHC machine produces a very high event rate in proton-proton collisions. Each bunch crossing results in about 20 particle interactions (bunch crossing rate means approximately10^9 interactions per second). In proton-proton collision the nominal event size is about 1.5 MB and 100 TB of data are generated per second. Technically it is not possible to store and process such a large amount of data in any storage, moreover we don't need most of these events for physics measurement since most of them are not interesting for further physics process. In order to select only interesting events and reduce the event rate, a trigger system was developed.

CMS trigger system consists of two stages:

- Level-1 Trigger (L1)
- High-Level Trigger (HLT)

The DAQ stores the events that pass the L1 trigger and sends them to a computer farm where the HLT events are processed. Schematic view of the CMS trigger and DAQ system is illustrated in Figure 4.16.

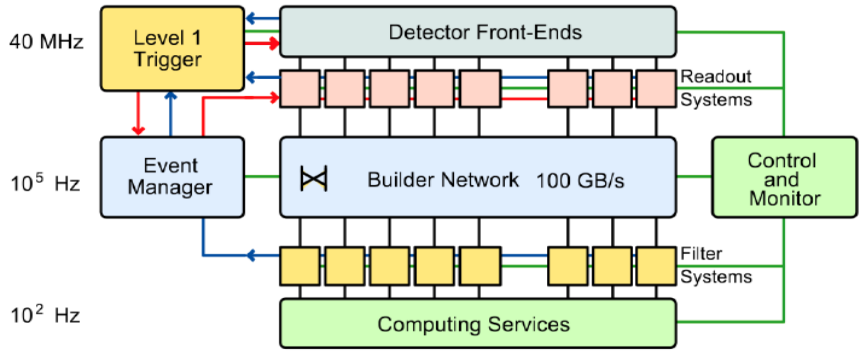

Figure 4. 16. CMS trigger and DAQ system (Bayatian et al., 2006).

4.7.1. Level 1 Trigger

The L1 trigger is a hardware based trigger that uses information from ECAL, HCAL and muon system. Hardware based L1 decides whether event deserve to save or not, directly after data have been collected from the detector. If events pass the L1 trigger then they will be stored temporarily for further check, if events don't pass the L1 trigger then they will be discarded forever. L1 trigger reduces the frequency of coming events from 40 MHz to 100 kHz to save and transfer them a to a computer farm.

4.7.2. High Level Trigger

High Level Trigger **(**HLT) is a software-based offline trigger which uses information from all subdetectors and runs fast reconstruction and identification algorithms to specify types of particles and their kinematics. It reduces the event rate from 100 kHz to 1000 Hz. Events that did not pass the HLT are lost forever. Events that pass HLT are arranged into appropriate datasets according to the HLT selection criteria they passed and stored for physics measurements.

4.8. CMS Forward Calorimeters

4.8.1. Centauro And Strange Object Research Calorimeter

The CASTOR detector is a quartz-tungsten sampling calorimeter (Panagiotou et al., 2008). The main features of the quartz calorimeters are radiation hardness, fast response and compact detector dimensions (Chatrchyan et al., 2008). CASTOR is designed for the very forward rapidity region for the heavy ion and proton-proton collisions at the LHC. It is located at 14.38 m from the interaction point, covering the pseudorapidity range $5.2 < |\eta| < 6.6$. Its main goals are to search for strangelets and centauro events in heavy ion collisions, and diffractive and low-x physics in proton-proton collisions at the LHC.

CASTOR is constructed from layers of tungsten (W) plates as absorber and fused silica quartz (Q) plates as active medium. The combination of one W and one Q plate is called a sampling unit (SU). CASTOR composed of Electromagnetic (EM) and Hadronic (HAD) sections. It is azimuthally divided into 16 sectors, and longitudinally 14 parts, 2 for the EM and 12 for the HAD sections as shown in Figure 4.17. In EM section each Readout Unit (RU) consists of 5 SUs and is 10.05 X_0 (0.385 λ_I) deep and in HAD section each RU consists of 5 SUs and is $0.77\lambda_I$ deep. In total CASTOR has 224 channels.

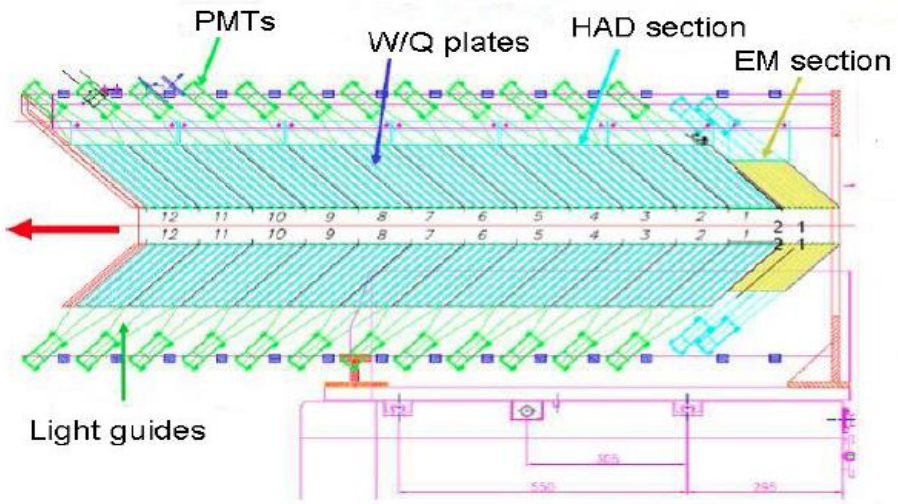

Figure 4. 17. Geometry of the CASTOR Calorimeter and its components (Chatrchyan et al., 2008).

CASTOR detector is a Cerenkov-based calorimeter as HF. In order to maximize the Cerenkov light the W/Q plates are sloped 45° according to the direction of the impinging particles. When the high energy particles are showered in the tungsten plate, the Cerenkov light is produced by the passage of relativistic charged particles through the quartz medium. Then Cerenkov light is collected in sections (RUs) along the length of the calorimeters and transmitted to the photodetector devices through air-core light guides.

4.8.2. Zero Degree Calorimeter

There are two identical ZDC calorimeters in the very forward region of CMS with a pseudorapidity coverage of $|\eta| \geq 8.3$. ZDCs are positioned between the two LHC beam pipes at ~140 m on each side of the CMS interaction region (Grachov et al., 2006). They are inside the neutral particle absorber which is called TAN. The design of the ZDC includes two independent calorimeter sections: an electromagnetic section (EM section) and a hadronic section (HAD section). These

sections are sampling calorimeters and are composed of a tungsten plate/quartz fiber ribbon stack to make the calorimeter compact, extremely fast, and radiation hard. The HAD section consists of 24 layers of 15.5 mm thick tungsten plates and 24 layers of 0.7 mm diameter quartz fibers while the EM section is made of 33 layers of 2 mm thick tungsten plates and 33 layers of 0.7 mm diameter quartz fibers (Chatrchyan et al., 2008). ZDC is designed for heavy ion and proton-proton diffractive studies. Its main goals are measuring neutrons and very forward photons for the heavy ion and low luminosity (up to 10^{33} cm^{-2} s^{-1}) proton-proton collisions.

5. ADD MODEL

5.1. ADD Extra Dimension Model

The monojet signature has been proposed as a discovery channel for Large Extra Dimensions in the framework of the Arkani-Hamed, Dimopoulos, and Dvali (ADD) model (Arkani-Hamed, Dimopoulos and Dvali, 1998). The ADD model accommodates the large difference between the electroweak and Planck scales by introducing a number d of extra spatial dimensions, which in the simplest scenario are compactified over a multidimensional torus of common radius R. In this framework, the SM particles and gauge interactions are confined to the ordinary $3+1$ space-time dimensions, whereas gravity is free to propagate through the entire multidimensional space. The strength of the gravitational force in 3 + 1 dimensions is effectively diluted. The fundamental Planck energy scale M_D of this 4+δ dimensional theory is related to the apparent four-dimensional Planck scale M_{Pl} according to $M_{\mathrm{PI}}^2 \approx M_{\mathrm{D}}^{\delta+2} R^{\delta}$. The production of gravitons is expected to be greatly enhanced by the increased phase space available in the extra dimensions. Once produced, the graviton escapes undetected into extra dimensions and its presence must be inferred from $E_{\mathrm{T}}^{\mathrm{miss}}$.

5.2. Large Extra Dimension

As previously described above, the ADD model attempts to solve the hierarchy problem by explaining existence of two widely different fundamental scales of nature: the electroweak scale (M_{EW} ~ 10^3 GeV) at which the electromagnetic and weak interaction unify, and the Plank scale (M_{PI}) (~10^{19} GeV) at which gravity becomes as strong as the gauge interactions. It was proposed by Nima Arkani-Hamed, Savas Dimopoulos, and Gia Dvali (1998). The ADD model assumes a 4+ n_{ED} dimension spacetime with n_{ED} toroidal dimensions with the concept of physics on branes. In this framework, all SM particles and gauge

interactions are confined on a 3 + 1 dimensional subspace (the brane), whereas it is assumed that gravity can propagate in the full (n_{ED} + 3) + 1 dimensional spacetime (the bulk). The freedom of gravity to propagate by way of the all dimensions causes the dilution of the gravity and the reduction in the gravitational field flux. The ordinary Planck scale of gravity in 4-dimensions (M_{PI}) is related to the fundamental Planck scale in 4 + n_{ED}dimensions (M_{D}) according to the formula:

$$M_{\mathrm{PI}}^{2} \approx M_{\mathrm{D}}^{\delta+2} R^{\delta} \tag{5.1}$$

where R is the size of the extra dimensions. M_{D} and n_{ED} are the parameters of this model.

In the ADD model, gravitons can be produced in association with colored particles (quarks or gluons) and suddenly escape from the detector (Berry, 2005). Its existence would be discoverable by the presence of a sizable missing transverse energy in the detector. The cross-section for this process depends primarly on the number of extra dimensions. The monojet + $E_{\mathrm{T}}^{\mathrm{miss}}$ signature, in the context of the ADD model, can arise from the following processes:

qq → gG, qg → qG and gg →gG

Where q is quark, g is gluon and G is graviton. Feynman diagrams are sketched in Figure 5.1 for these processes.

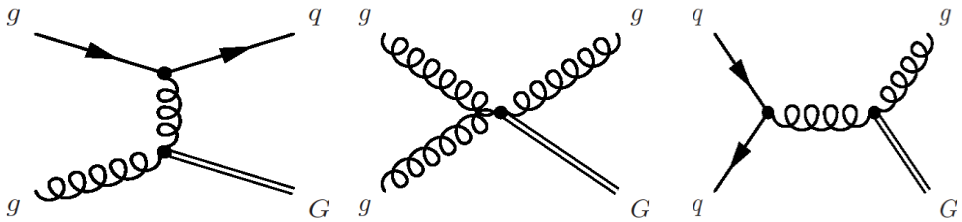

Figure 5. 1. Three different production modes for real gravitons G production in association with a colored parton (q or g) as predicted in the ADD extra dimensions model.

5.3. Simulation of the Graviton Production in ADD

In order to study the monojet analysis sensitivity in the relevant ADD parameter space, ADD samples with M_{D} ranging from 3 to 12 TeV and n_{ED} = 2, 3, 4, 5, 6 have been processed as part of the official Summer16 CMS production campaign. Simulated samples for ADD model are generated using PYTHIA 8. Only one signal point is missing (n_{ED}= 2 M_{D} = 6 TeV) and it has been produced privately with CMSSW full detector simulation. The corresponding ADD samples are listed in Table 5.1. Cross-sections are computed at Leading Order (LO) QCD and their trend as a function of n_{ED} and M_{D} are shown in Figure 5.2, as well as reported numerically (in pb) in Table 5.1.

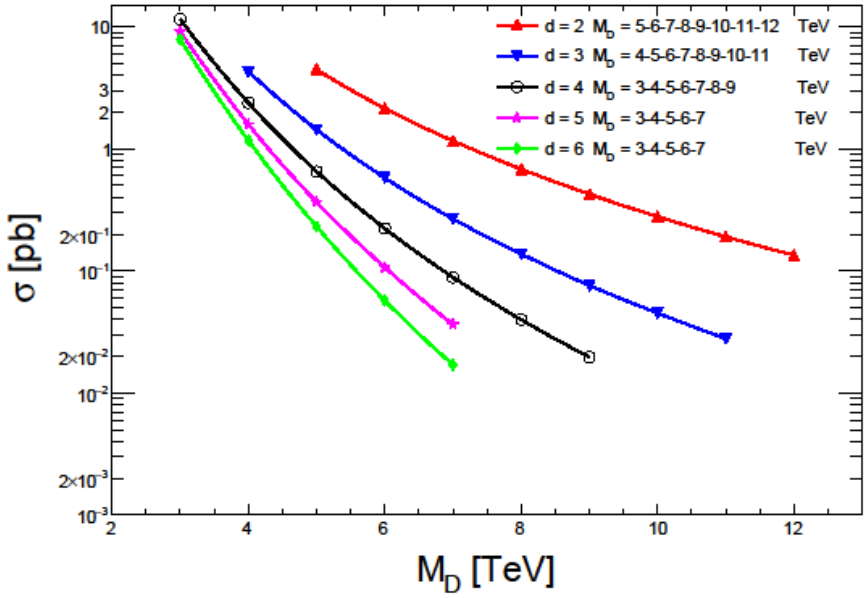

Figure 5. 2. Cross-section of ADD signals in pb as a function of M_D for n_{ED} = 2, 3, 4, 5, 6.

PYTHIA internal truncation is used in generation, setting the CutOffmode to 1. Since the implementation in PYTHIA is an effective theory that holds for energies well below the M_D scale, the cross section for the signal is suppressed by a factor $M_D^2/\hat{s}$ when the center-of-mass energy of the partonic interaction $\hat{s}$ exceeds this scale.

Table 5. 1. Datasets are used for ADD signal analysis.

ADD Signal Samples	Cross-section (pb)	Events
ADDMonoJet_MD-5_d-2_TuneCUETP8M1_13TeV-pythia8	4.445	99923
ADDMonoJet/gurpinar-d2MD6_TCUETP8M1_13TeV-pythia8	2.138	49761
ADDMonoJet MD-7 d-2TuneCUETP8M1_13TeV-pythia8	1.161	97454
ADDMonoJet MD-8 d-2TuneCUETP8M1_13TeV-pythia8	0.681	99105
ADDMonoJet MD-9 d-2TuneCUETP8M1_13TeV-pythia8	0.423	98430
ADDMonoJetMD-10 d-2TuneCUETP8M1_13TeV-pythia8	0.277	99422
ADDMonoJet MD-11 d-2TuneCUETP8M1_13TeV-pythia8	0.190	99244
ADDMonoJet MD-12 d-2TuneCUETP8M1_13TeV-pythia8	0.134	99926
ADDMonoJet MD-4 d-3 TuneCUETP8M1 13TeV-pythia8	4.280	97582
ADDMonoJet MD-5 d-3 TuneCUETP8M1 13TeV-pythia8	1.434	98596
ADDMonoJet MD-6 d-3 TuneCUETP8M1 13TeV-pythia8	0.577	99907
ADDMonoJet MD-7 d-3 TuneCUETP8M1 13TeV-pythia8	0.266	99271
ADDMonoJet MD-8 d-3 TuneCUETP8M1 13TeV-pythia8	0.137	99909
ADDMonoJet MD-9 d-3 TuneCUETP8M1 13TeV-pythia8	0.759	99932
ADDMonoJet MD-10 d-3 TuneCUETP8M1 13TeV-pythia8	0.451	99282
ADDMonoJet MD-11 d-3 TuneCUETP8M1 13TeV-pythia8	0.278	99920
ADDMonoJet MD-3 d-4 TuneCUETP8M1 13TeV-pythia8	10.15	98685
ADDMonoJet MD-4 d-4 TuneCUETP8M1 13TeV-pythia8	2.373	99085
ADDMonoJet MD-5 d-4 TuneCUETP8M1 13TeV-pythia8	0.651	98364
ADDMonoJet MD-6 d-4 TuneCUETP8M1 13TeV-pythia8	0.223	98649
ADDMonoJet MD-7 d-4 TuneCUETP8M1 13TeV-pythia8	0.0885	95523
ADDMonoJet MD-8 d-4 TuneCUETP8M1 13TeV-pythia8	0.3988	99905
ADDMonoJet MD-9 d-4 TuneCUETP8M1 13TeV-pythia8	0.0196	95914
ADDMonoJet MD-3 d-5 TuneCUETP8M1 13TeV-pythia8	9.096	99906
ADDMonoJet MD-4 d-5 TuneCUETP8M1 13TeV-pythia8	1.585	99101
ADDMonoJet MD-5 d-5 TuneCUETP8M1 13TeV-pythia8	0.365	99008
ADDMonoJet MD-6 d-5 TuneCUETP8M1 13TeV-pythia8	0.106	99920
ADDMonoJet MD-7 d-5 TuneCUETP8M1 13TeV-pythia8	0.036	97464
ADDMonoJet MD-3 d-6 TuneCUETP8M1 13TeV-pythia8	7.867	99310
ADDMonoJet MD-4 d-6 TuneCUETP8M1 13TeV-pythia8	1.168	97271
ADDMonoJet MD-5 d-6 TuneCUETP8M1 13TeV-pythia8	0.230	98425
ADDMonoJet MD-6 d-6 TuneCUETP8M1 13TeV-pythia8	0.057	97374
ADDMonoJet MD-7 d-6 TuneCUETP8M1 13TeV-pythia8	0.017	99918

6. FERMION PORTAL DARK MATTER

6.1. Fermion Portal Dark Matter

Fermion Portal (FP) DM (χ) is one of the simplified DM models in which one DM particle couples with a scalar mediator (ϕ) and a SM fermion. Since the DM couples directly to quarks, it can be produced at colliders. In addition, the colored mediator may be produced as well, yielding strong constraints both from associated and pair production mechanisms. Except in the regime of an extremely heavy mediator, Dirac fermion, Majorana fermion, complex scalar DM channels provide the dominant constraints (Bai and Berger, 2013). Fermionic DM couples to right-handed quarks as portal to the DM sector. Dirac or Majorana fermion, χ, that is an SM gauge singlet can be candidate of the DM. The mediator is an $SU(3)_c$ triplet with an properly chosen hypercharge. The renormalizable operators are:

$$\mathcal{L}_{fermion} \supset \lambda_{ui}\, \phi_{ui}\, \bar{\chi}_L u_R^i + \lambda_{di} \phi_{di} \bar{\chi}_L\, d_R^i + \text{h.c.}\,, \tag{6.1}$$

where u_i = u, c, t (d_i = d, s, b) are different SM quarks. The partner masses M_ϕ must be larger than the DM mass M_χ because χ is the DM candidate. The branching ratio of the decay $\phi_u \rightarrow \chi\, u^i$ *and* $\phi_d \rightarrow \chi\, d^i$ is assumed to be 100% (Bai and Berger, 2013).

In this thesis, the DM candidate is assumed only couple to up-type quarks with a coupling constant λ_u, which is universal in flavour i.e. identical for (u, c, t). The associated production of the mediator (ϕ) and the DM particle (χ), along with radiative contributions from DM pair production, yield a monojet signature, while pair production of mediators can be observed as jets plus missing transverse energy.

6.1.1. Collider Signatures

At hadron colliders, the signature of FP models can come from pair productions of the scalar mediator, which then decays into DM particles and quarks

(Bai and Berger, 2013), as shown in Figure 6.1 (a). Moreover, the scalar mediator can be produced in association with the DM candidate product a typical monojet like signature as reported in Figure 6.1 (b). Eventually, DM candidates can be produced by a t-channel exchange of the scalar mediator. This particular production mode may be accessible at colliders only when partons are radiated from the initial state (ISR), as displayed in Figure 6.1 (c). The production mechanism and collider phenomenology for the scalar-mediated models is indeed similar to a minimal "simplified" SUSY scenario. One difference in this case is that there is additional freedom to adjust the couplings λ_q which can lead to enhanced single mediator production, i.e. enhanced monojet signal rate, since the model parameters are no longer constrained by supersymmetry. In addition, we discuss fermion-mediated models, which have a different production cross-section and somewhat different phenomenology. In the limit of a small DM-mediator coupling, $\lambda_u \sim 0$, the only significant diagram yielding this final state is Figure 6.1 (a), producing dijet+MET signature. The production cross section is identical to that of a single squark production in the MSSM. As λ_u increases, the diagram Figure 6.1 (b) becomes significant, producing monojet signal.

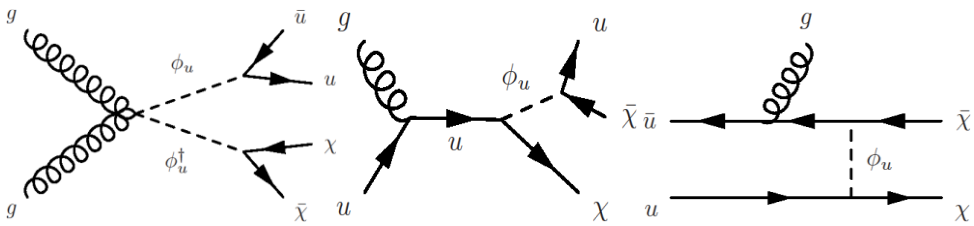

(a) (b) (c)

Figure 6. 1. Diagrams of the main production mechanisms of DM particles in the FP model in association with a single quark or gluon at the LHC. Diagram (a) has two jets in final state, while (b) and (c) provide monojet signatures.

The current couplings were chosen high enough to allow for all interesting production modes, but low enough to not break perturbation expansion indicated by the original theory paper where the theorists are providing limits for $\lambda_u = 1.0$ and 0.5. In our analysis we have considered $\lambda_u = 1.0$ (Bai and Berger, 2013).

6.1.2. Signal Production

Since the Dirac scenario is the most interesting for collider searches, the monojet analysis re-interpretation is focusing only FP Dirac DM signals. Signal events are generated using MadGraph5 at Leading Order (LO), showered by Pythia 8 and finally passed trought the CMS full simulation. The parton-level cross sections as a funtion of (M_χ, M_ϕ) are shown in Figure 6.2. In particular, Figure 6.2 (left) shows the total production cross section, considering all the three different production modes discussed in the previous section, vs DM mass (M_χ) for different values of mediator mass (M_ϕ). Similarly, Figure 6.2 (right) shows the trend vs mediator mass. The cross sections decrease exponentially with M_ϕ, while the dependence on M_χ is only linear.

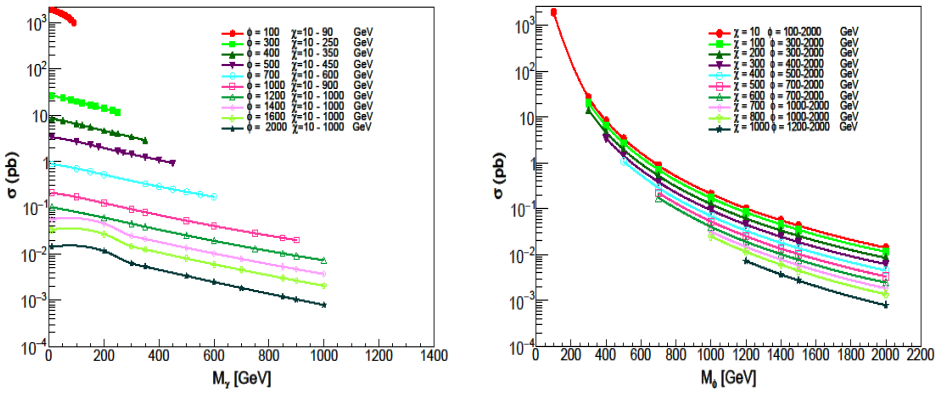

Figure 6. 2. The production cross-sections versus M_χ (left) and M_ϕ (right) for the Dirac DM case.

The cross section of the "two ϕ state", decreases rapidly as shown in Figure 6.3. The associated production, labelled as "one mediator final state", represents the main production mechanism for small M_ϕ values, i.e. below 1 TeV, while the t-channel production becomes the largest contribution to the total cross section for $M_\phi > 1$ TeV. Thus, for high mediator masses, this leads to production of low E_T^{miss} events reducing the overall signal acceptance. In the signal generation, λ_u has been fixed to one, which is defined according to the following equation:

$$\Gamma(\phi \rightarrow \chi + \bar{u}) = \frac{\lambda_u^2}{16\pi} \frac{\left(M_\phi^2 - M_\chi^2\right)^2}{M_\phi^3} \tag{6.2}$$

Figure 6.4 shows the trend of the total width in GeV as a function of M_ϕ and $M\chi$ and the black line indicates roughly separation between the on-shell and off-shell region. Figure 6.5 shows signal cross section times monojet selection efficiency (E_T^{miss} > 250 GeV) , expressed in pb, expected different signal hypothesis in the $M_\phi - M_\chi$ plane.

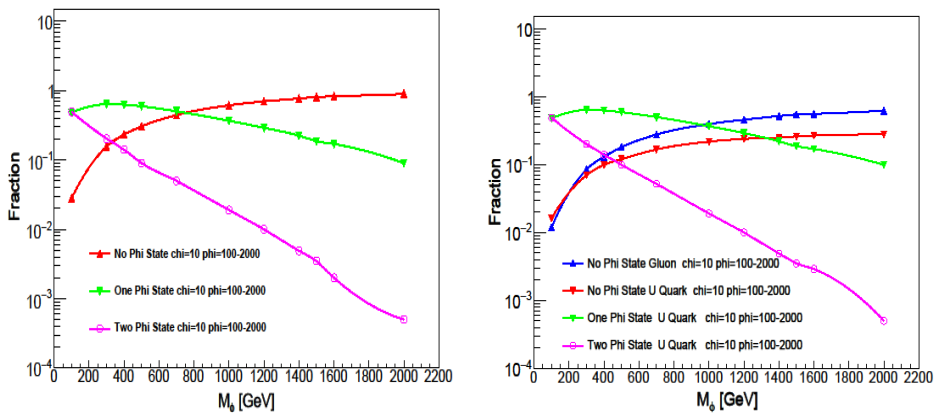

Figure 6. 3. The fraction of events as a function of M_ϕ for the associated production of mediators M_ϕ (left). (Right) summary fraction plot including also *t*-channel production.

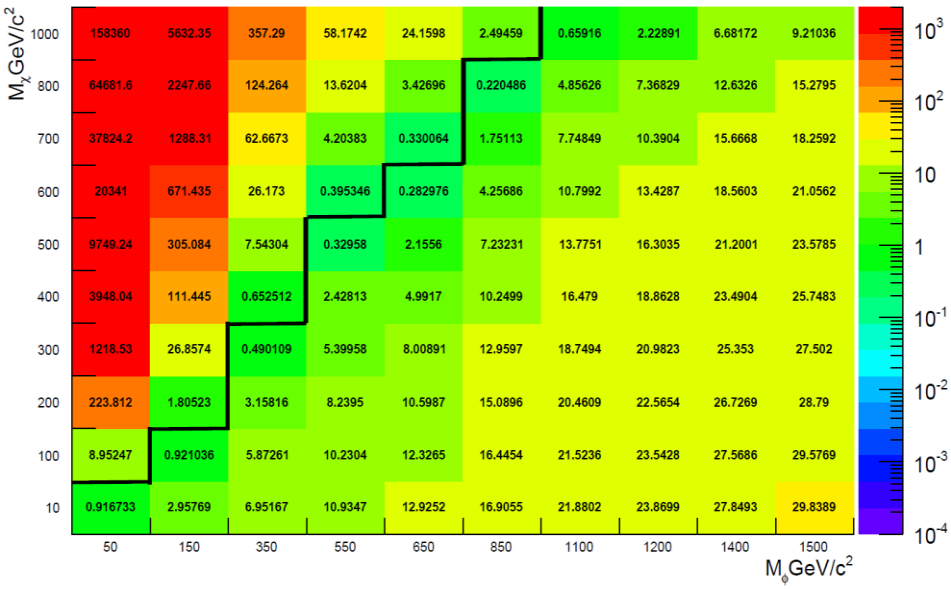

Figure 6. 4. Total width of the mediator (M_ϕ) in GeV as a function of M_ϕ and M_χ. The black line indicates roughly separation between the on-shell of and off-shell region ($M_\phi < 2\ M_\chi$).

Since the sensitivity in the off-shell region ($M_\phi < 2M_\chi$) is expected to be reduced, only the t-channel production will contribute to the total cross section. Since we expect a drop in sensitivity in any case, we have decided not to produce signal sample in the off-shell region.

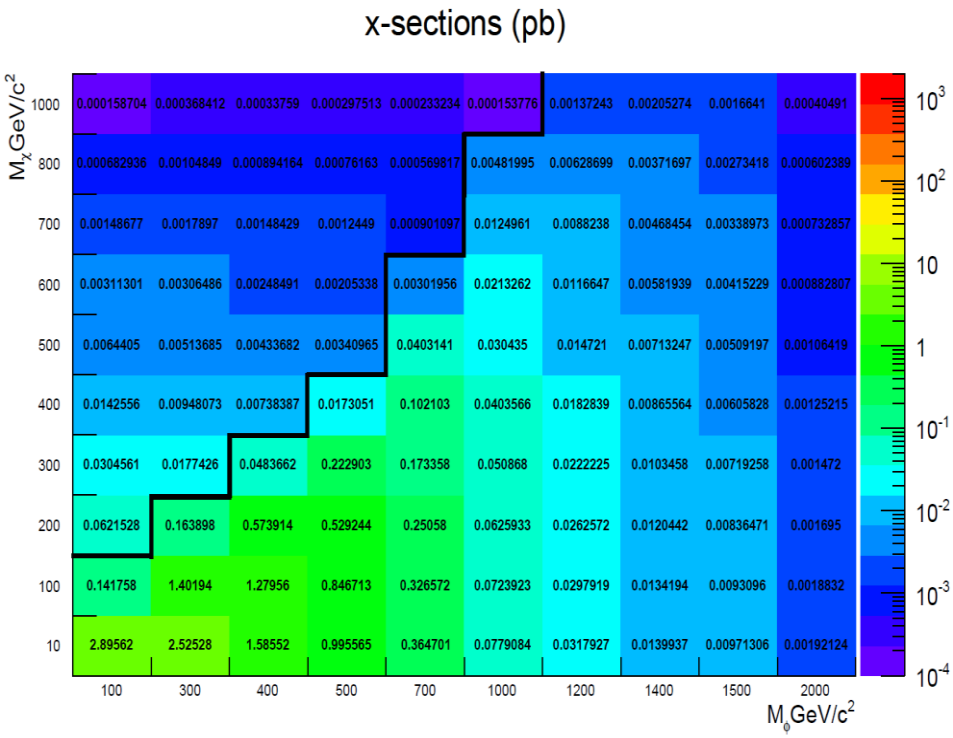

Figure 6. 5. Signal cross section times monojet selection efficiency, expressed in pb, expected different signal hypothesis in the M_ϕ, M_χ plane.

Generator level E_T^{miss} distributions for a subset of the (M_ϕ, M_χ) grid are shown in Figure 6.6. Jet from the decay of $\phi \rightarrow \chi +$ jet are energetic and the E_T^{miss} distributions shows a Jacobian-like peak at around $M_\phi/2$ for a small M_χ values. For a larger M_χ, i.e. off-shell mediators ($M_\phi < 2M_\chi$), the Jacobian peak disappears and the expected E_T^{miss}distribution becomes a falling spectra.

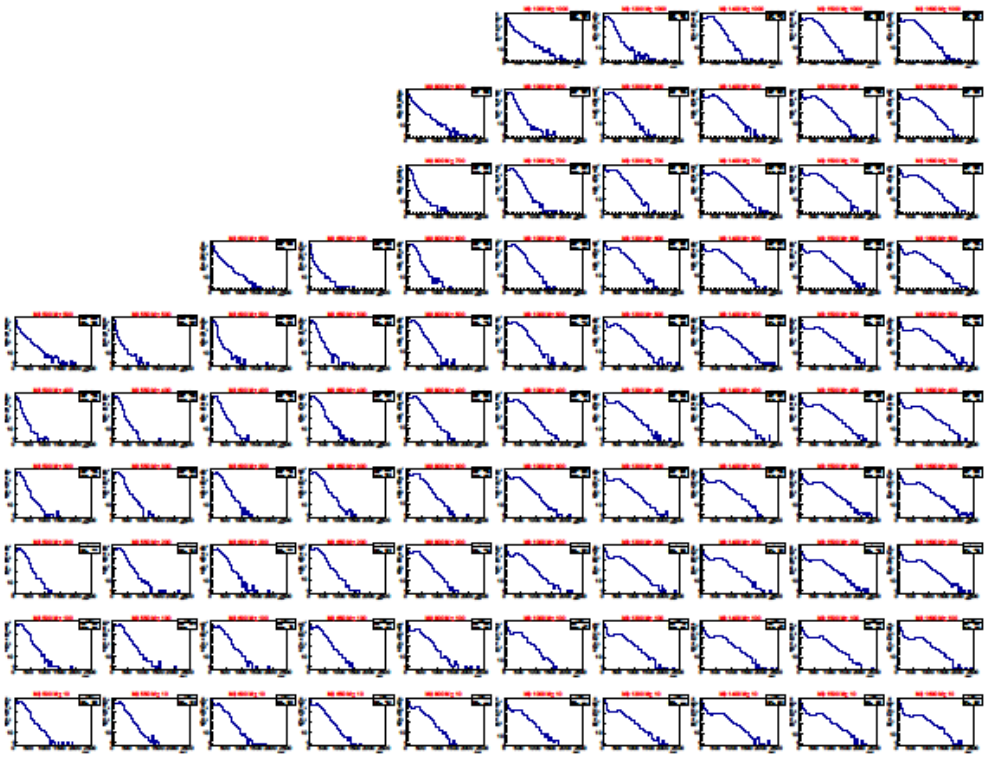

Figure 6. 6. Generator level E_T^{miss}distrubution for different M_ϕ and M_χ.

6.2. Relic Abundance

The relic abundance of non-baryonic matter is completely determined by cosmological restrictions to be $\Omega\chi h^2 = 0.1199 \pm 0.0027$ (Planck Collaborations, 2013). In our model, we assume that the DM is entirely composed of the χ particle. According to the supposition that χ particles were in thermal equilibrium in the early universe, its existing relic density is determined by freeze-out from the annihilation process $\bar{\chi}\chi \rightarrow \bar{q}q$shown in Figure 6.7. At temperatures $T_f \sim m_\chi/25$,the relic abundance is specified by the thermally averaged annihilation cross section $\langle\sigma(\bar{\chi}\chi \rightarrow \bar{x}qq)v\rangle$ (Spencer et al., 2014).

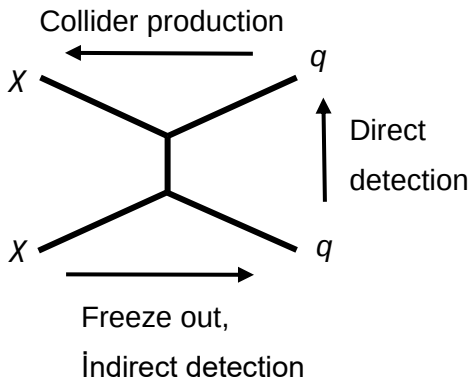

Figure 6. 7. Feynman diagram is showing the annihilation (freeze out) of DM in the early universe, indirect detection of DM and collider production of DM.

7. DATA SAMPLES

7.1. Data Taking Operations

The data related to this study corresponds to an integrated luminosity of 35.9 fb^{-1}collected by the CMS data taking campaign at 13 TeV in 2016. From Run2016B to Run2016G the 23rd September re-reco has been considered, while Run2016H era was based on prompt calibration and alignment conditions were used to reconstruct the used data. The list of datasets used in this analysis are given in Table 7.1, together with the corresponding integrated luminosity. The Missing Transverse Energy (E_T^{miss}) dataset is used for the Signal Region (SR), Single Muon Control Region (CR) and double muon CR analysis. Single electron dataset is used for both single electron and double electron CR analysis. And single photon dataset is used for calibrations and background single photon CR**.**

Table 7. 1. Data sets used in the analysis.

Dataset Name	Event Selected For
MET-Run2016*-23Sep2016 MET-Run2016H-PromptReco-v*	Signal region, Single muon CR, Double muon CR
/SingleElectron/Run2016*-23Sep2016 /SingleElectron/Run2016H-PromptReco-v*	Single electron CR and Double electron CR
/SinglePhoton/Run2016*-23Sep2016 /SinglePhoton/Run2016H-PromptReco-v*	γ+jets CR
/JetHT/Run2016*-23Sep2016 /JetHT/Run2016H-PromptReco-v*	Single electron CR, Double electron CR and γ+jets CR

7.2. Monte Carlo Samples for Background Simulation

There are several SM processes similar to DM signals. These processes are given below and simulated datasets can be seen in Table 7.2.

Z(νν) + jets : This process create main background for the mono jet analysis. For this background MC samples have been produced using the MadGraph generator in several bins of hadronic transverse (H_{T}) energy sum.

W + jets: The second largest background comes from this process in the analysis. This background can be reduced by applying a veto on events in which the presence of leptons is detected. MC samples have been generated at LO in QCD using the MadGraph generator in several bins of H_{T} for this background.

Z(*ll*) + jets: This process passes the analysis selection and hence mimics signal-like events in the case where the leptons from the Z boson decay pass undetected. In addition, Z(ee) + jets and Z(μμ) + jets events are also used as control samples for estimating the Z(νν) + jets background. MC samples for this process have been generated at LO in QCD using the MadGraph generator in several bins of H_{T}.

γ + jets: This process events are used as a control sample in the analysis in order to estimate the Z(νν) + jets background. MC samples for this process have been generated at LO in QCD using the MadGraph generator in several bins of H_{T}.

Top: Top-quark decays (both tt and single top) also constitute as backgrounds in this analysis. tt MC samples have been produced with the aMC@NLO and Powheg generators at next-to-leading order (NLO), while Single-top events have been generated with the Powheg generator at NLO.

Diboson: An other source of background to this analysis are decays of diboson pairs (WW, WZ, ZZ). WZ and ZZ MC samples have been generated at LO with the PYTHIA 8, while WW production is generated via the Powheg-box at NLO-QCD.

QCD: QCD events typically do not have large genuine E_T^{miss}. However given the large cross section with which these events are produced, even a very small fraction of events in which a high momentum jet is mismeasured or goes undetected can serve as a background to this analysis. QCD MC samples have been generated at LO in QCD using the MadGraph generator in several bins of H_{T}.

Table 7. 2. Background Monte Carlo data sets produced in the Spring16 campaign.

Dataset Name	Cross-section (pb)	Cross-section Order in QCD
/ZJetsToNuNu HT-100To200 13TeV-madgraph	280.5	LO
/ZJetsToNuNu HT-200To400 13TeV-madgraph	77.7	LO
/ZJetsToNuNu HT-400To600 13TeV-madgraph	10.71	LO
/ZJetsToNuNu HT-600To800 13TeV-madgraph	2.562	LO
/ZJetsToNuNu HT-800To1200 13TeV-madgraph	1.183	LO
/ZJetsToNuNu HT-1200To2500 13TeV-madgraph	0.286	LO
/ZJetsToNuNu HT-2500ToInf 13TeV-madgraph	6.976×10^{-4}	LO
/WJetsToLNu_HT-100To200_TuneCUETP8M1_13TeV-madgraphMLM-pythia8	1343	LO
/WJetsToLNu_HT-200To400_TuneCUETP8M1_13TeV-madgraphMLM-pythia8	359.6	LO
/WJetsToLNu_HT-400To600_TuneCUETP8M1_13TeV-madgraphMLM-pythia8	48.85	LO
/WJetsToLNu_HT-600To800_TuneCUETP8M1_13TeV-madgraphMLM-pythia8	12.05	LO
/WJetsToLNu_HT-800To1200_TuneCUETP8M1_13TeV-madgraphMLM-pythia8	5.501	LO
/WJetsToLNu_HT-1200To2500_TuneCUETP8M1_13TeV-madgraphMLM-pythia8	1.329	LO
/WJetsToLNu_HT-2500ToInf_TuneCUETP8M1_13TeV-madgraphMLM-pythia8	0.03216	LO
/DYJetsToLL_M-50_HT-100to200_TuneCUETP8M1_13TeV-madgraphMLM-pythia8	148	LO
/DYJetsToLL M-50_HT-200to400_TuneCUETP8M1_13TeV-madgraphMLM-pythia8	40.94	LO
/DYJetsToLL M-50_HT-400to600 _TuneCUETP8M1_13TeV-madgraphMLM-pythia8	5.497	LO
/DYJetsToLL M-50_HT-600to800_TuneCUETP8M1_13TeV-madgraphMLM-pythia8	1.354	LO
/DYJetsToLLM-50_HT-800to1200_TuneCUETP8M1_13TeV-madgraphMLM-pythia8	0.625	LO
/DYJetsToLLM-50_HT-1200to2500_TuneCUETP8M1_13TeV-madgraphMLM-pythia8	0.151	LO
/DYJetsToLL M-50_HT-2500toInf_TuneCUETP8M1_13TeV-madgraphMLM-pythia8	3.647×10^{-3}	LO
/GJets HT-100To200 TuneCUETP8M1 13TeV-madgraphMLM-pythia8	9235	LO
/GJets HT-200To400 TuneCUETP8M1 13TeV-madgraphMLM-pythia8	2298	LO
/GJets HT-400To600 TuneCUETP8M1 13TeV-madgraphMLM-pythia8	277.6	LO
/GJets HT-600ToInf TuneCUETP8M1 13TeV-madgraphMLM-pythia8	93.47	LO
/TTJets TuneCUETP8M1 13TeV-amcatnloFXFX-pythia8	831.76	NNLO+NNLL
/TT TuneCUETP8M1 13TeV-powheg-pythia8	831.76	NNLO+NNLL
/ST s-channel 4f leptonDecays 13TeV-amcatnlo-pythia8 TuneCUETP8M1	3.4	NLO
/ST t-channel top 4f leptonDecays 13TeV-powheg-pythia8 TuneCUETP8M1	44.1	NLO
/ST t-channel antitop 4f leptonDecays 13TeV-powheg-pythia8 TuneCUETP8M1	26.2	NLO
/ST tW top 5f inclusiveDecays 13TeV-powheg-pythia8 TuneCUETP8M1	35.6	NNLO
/ST tW antitop 5f inclusiveDecays 13TeV-powheg-pythia8 TuneCUETP8M1	35.6	NNLO
/WWTo2L2Nu 13TeV-powheg	12.18	NLO
/WWTo4Q 13TeV-powheg	49.99	NLO
/WWToLNuQQ 13TeV-powheg	51.72	NLO
/WW TuneCUETP8M1 13TeV-pythia8	118.7	NNLO
/WZ TuneCUETP8M1 13TeV-pythia8	47.2	NLO
/ZZ TuneCUETP8M1 13TeV-pythia8	16.6	NLO
/QCD HT100to200 TuneCUETP8M1 13TeV-madgraphMLM-pythia8	2.75×10^{7}	LO
/QCD HT200to300 TuneCUETP8M1 13TeV-madgraphMLM-pythia8	1.735×10^{6}	LO
/QCD HT300to500 TuneCUETP8M1 13TeV-madgraphMLM-pythia8	3.67×10^{5}	LO
/QCD HT500to700 TuneCUETP8M1 13TeV-madgraphMLM-pythia8	2.937×10^{4}	LO
/QCD HT700to1000 TuneCUETP8M1 13TeV-madgraphMLM-pythia8	6524	LO
/QCD HT1000to1500 TuneCUETP8M1 13TeV-madgraphMLM-pythia8	1064	LO
/QCD HT1500to2000 TuneCUETP8M1 13TeV-madgraphMLM-pythia8	121.5	LO
/QCD HT2000toInf TuneCUETP8M1 13TeV-madgraphMLM-pythia8	25.42	LO

8. TRIGGERS

The data was collected using several triggers designed to select events that have large E_T^{miss} and Missing Hadronic Transverse (H_T^{miss}) energy for this study. These triggers use the online version of the particle-flow algorithm. In the trigger algorithm, identified particle flow muons are removed from the event before the E_T^{miss} and the H_T^{miss} objects are calculated. By this way, dimuon (mainly $Z \rightarrow \mu^+\mu^-$) and single muon (mainly $W \rightarrow \mu\nu$) events are also selected using the same triggers. These events are used as a control sample for the Z(νν) + jets background. The others CRs used in the analysis contain dielectron, single electron and γ + jets events. Dielectron, single electron events are selected using the single electron trigger while γ + jets events are selected using the single photon trigger. The single electron and photon triggers are affected by some inefficiency in high electron/photon transverse momentum (p_T) (several hundred GeV) because of a misconfiguration of the L1 seed during the first part of the data, Run2016B (about 4 fb^{-1}) but this inefficiency almost negligible in the full 2016 dataset, which can be partially recovered by adding the EcalHT800 trigger. All triggers which are used in the analysis, are shown in Table 8.1.

Table 8. 1. HLT paths, and the associated L1 seeds used in the analysis. '[X]' in the trigger path name stands for 90 or 100 or 110 or 120 GeV.

HLT path	L1 seed	Primary dataset
HLT_PFMET170_*	L1_ETM70 or L1_ETM100	MET
HLT_PFMETNoMu[X]_PFMHTNoMu[X]_IDTight	L1_ETM70 or L1_ETM100 L1_ETM60_NotJet52WdPhi2	MET
HLT_Ele27_WPTight	L1_SingleEG20 L1_SingleIsoEG18er	SingleElectron
HLT_Ele105_CaloIdVT_GsfTrkIdT	L1_SingleEG40 L1_SingleJet200	SingleElectron
HLT_Photon165_HE10	L1_SingleEG40 L1_SingleJet200	SinglePhoton
HLT_Photon175	L1_SingleEG40 L1_SingleJet200	SinglePhoton
HLT_EcalHT800	L1_ETM70	JetHT

8.1. E_T^{miss} Trigger Performance

We measure performance of the E_T^{miss} triggers (in an OR) using single electron and single muon events ($W \rightarrow l\nu$ decays) after requiring the whole monojet selections. Especially, single electron events are selected from the SingleElectron dataset, where the p_T of the reconstructed electron is required to be larger than 40 GeV and the electron is required to pass certain tight identification criteria. Similarly, the single muon events are selected from the SingleMuon dataset, wherein the muon is required to be well-identified and have $p_T > 20$ GeV.

In both the single muon and single electron events, a central jet ($p_T > 100$ GeV) is required in addition to the lepton. In the case of the single muon events, the trigger efficiency is computed with respect to the E_T^{miss} recoil i.e. E_T^{miss} computed without including the muon. In the case of the single electron events, the efficiency is computed as a function of the E_T^{miss}.

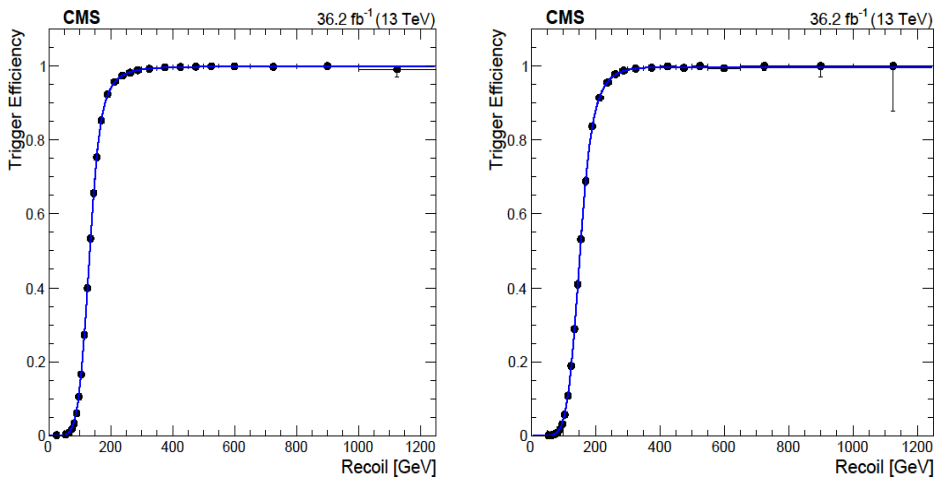

Figure 8. 1. E_T^{miss} trigger turn-on curve measured in single muon events (left) and single electron events (right) (Daci et al., 2016).

Figure 8.1 shows the turn-on curves for the E_T^{miss} triggers measured in these single lepton events. The turn-on curves in the single-muon and single-electron

events agree very well in the plateau region, differing by at most 1-2% for $E_T^{miss} > 200$ GeV

8.2. Photon Trigger Performance

For the γ + jets CR, we used single photon triggers to select events that pass a logical OR of two single photon triggers. One of these triggers is with p_T threshold of 165 GeV and another is with p_T threshold of 175 GeV. The performance of the trigger is measured in events passing the PFHT650. These events are required to have at least a high p_T central jet ($p_T > 100$ GeV) and also to have a single photon in the barrel ($|\eta| < 1.4442$) passing the identification criterion imposed by this analysis. Figure 8.2 shows the efficiency of the single photon triggers as a function of the hadronic recoil of the event using black points. The trigger efficiency is around 98% for events with hadronic recoil larger than 400 GeV. Besides, the red points in Figure 8.2 shows the trigger efficiency of a logical OR of the single photon triggers with the EcalHT800 trigger which is the lowest un-prescaled H_T trigger.

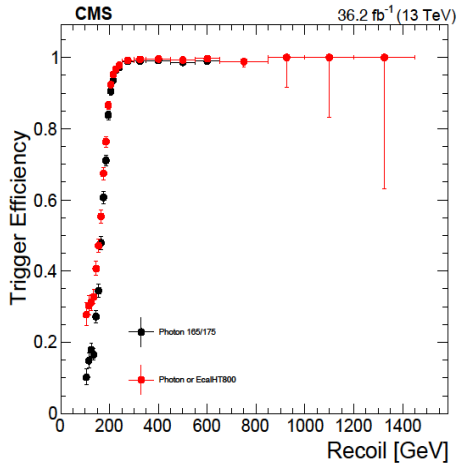

Figure 8. 2. Turn on curve, as a function of photon p_T, for the single photon triggers (black), and for the combination of the single photon and EcalHT800 triggers (red). The efficiency is measured in events passing the PFHT650 trigger (Daci et al., 2016).

As it was expected, EcalHT800 allows for a small recovery of trigger efficiency at high recoil once the full 2016 dataset is explored. We see that some residual loss in efficiency (2-3%) for recoil between 300 to 600 GeV, however beyond that range the efficiency goes up to unity.

8.3. Electron Trigger Performance

For dielectron and single-electron CR, events are selected with algorithms Ele27 and Ele105 triggers with a p_{T} threshold of 27 GeV combined with a nonisolated single-electron trigger with a p_{T} threshold of 105 GeV. The Ele105 trigger algorithm has just a loose identification and no isolation requirements whereas the Ele27 trigger algorithm has tight identification and isolation requirements . For selection of the data those two approaches of algorithm are used for the efficiency of the electron triggers. For low p_{T}electrons, we used “tag and probe” technique in which the trigger efficiency is measured on an electron leg of the Z boson. Selected events have one tag electron which fires the single electron triggers and passes the tight identification requirements. After that a second probe electron is required in the event as well. The probe electron should pass the tight selection too, and the invariant mass of the dielectron pair should be consistent with the Z-boson peak. Then the fraction of events where the probe electron fires the trigger gives the trigger efficiency. The trigger efficiency were calculated in bins of the $p_{\mathrm{T}}$and η of the electron. The drawback of the tag and probe approach is that we run out of Z events at high electron p_{T}. Therefore, to complement this measurement we measure the electron efficiency in events from the JetHT passing the PFHT800 trigger. This procedure is similar to the efficiency measurement of the photon triggers. Figure 8.3 shows the trigger efficiency measured in bins of electron p_{T} and η. In the case of electrons with p_{T} less than 100 GeV the trigger efficiency is taken from the Z tag and probe measurement (left plot) while for electrons with p_{T} greater than 100 GeV, the trigger efficiency is taken from the JetHT data (right plot).

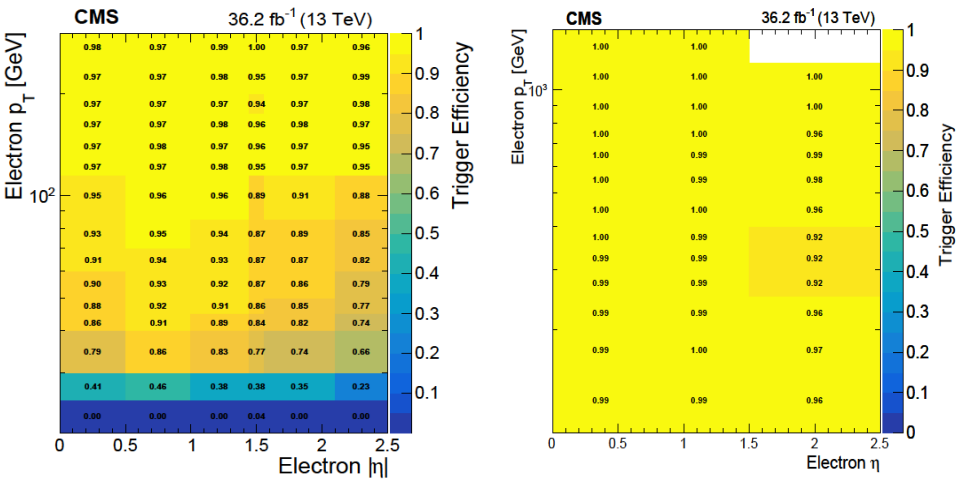

Figure 8. 3. Single electron trigger efficiency as a function of electron p_T and η. The left plot shows the trigger efficiencies measured using Z tag and probe starting with electron p_T of 20 GeV. The right one shows the electron trigger efficiency measured in the JetHT dataset using events passing the PFHT650 or PFHT800 trigger, starting at electron p_T of 100 GeV (Daci et al., 2016).

9. RECONSTRUCTION of PHYSICS OBJECTS

All significant physics objects are used to identify signal-like events, suppress backgrounds and define CRs in data. Generaly, we adhere to CMS Physics Objects Group (POG) recommendations. Physics objects and the selection necessities imposed on them are described below.

9.1. Reconstruction of Primary Vertex and Pileup Reweighting

Owing to pileup, several primary vertices are typically reconstructed in an event. A loose set of selection criteria are used to select well-reconstructed primary vertices and the vertex with the highest sum of p_T of component tracks is chosen as the one corresponding to the hard interaction.

9.2. Missing Transverse Energy Reconstruction

The missing transverse energy vector is calculated as the negative vector sum of the transverse momenta of all particles reconstructed in the event. In this analysis, the E_T^{miss} is calculated excluding the muons. Corrections applied to momenta of reconstructed jets are also applied to E_T^{miss} as a correction (Type-1 corrections) in a given event. To mimic the E_T^{miss} in the SR, CRs are constructed by selecting either photon, a lepton or pairs of leptons. These correspond to regions where either γ+jets production, W-boson or Z-boson production is dominant. The hadronic recoil against the bosons can be calculated by removing the p_T of the leptons and photons from the E_T^{miss} calculation. Officially, the recoil is given as follows:

$$\vec{U} = \vec{E}_T^{miss} + \vec{p}_T^{ll,l,\gamma} \tag{9.1}$$

where the $\vec{p}_T$ is transverse momentum of one of the following objects depending upon the CR: dilepton, lepton, photon.

In the case of Z→νν decays, $\vec{U} = E_T^{miss}$. We can use Z→ νν events in the CR to recognize fake E_T^{miss} events present in the SR. For this reason, we present the results

for the rest of the analysis in terms of the hadronic recoil. Due to detector noise, mis-reconstruction and beam backgrounds events in data can result in large fake E_T^{miss}. In order to remove these events a few E_T^{miss} filters, as listed below, have been recommended by JetMET POG (CMS Jet/MET POG) and have been used in the analysis (Daci et al., 2016).

- Good Vertex Filter, i.e. at least one good primary vertex in the event.
- 2016 Global Halo Filter, used to reject beam backgrounds.
- HBHE Noise Filter.
- HBHEIso Noise Filter.
- EE Bad SC Filter.
- ECAL Dead Cell Trigger Primitive Filter.
- Updated Bad Muon Filter.
- Updated Bad Charged Hadron Filter.

In addition to these filters some other precautions are also performed to suppress the anomalous E_T^{miss}events as follows:

- The analysis is not directly affected by fake E_T^{miss} events induced by extra/fake muons because we use the recoil variable for the muon final states.
- We apply a loose muon veto both in SR and CRs.
- To minimise the effect of fake Particle Flow (PF) E_T^{miss}, we look at the variable $\left|{E_T^{miss}}_{calo} - {E_T^{miss}}_{PF}\right| / U$ which is the difference between calorimetric or calorimeter (calo) $E_T^{miss}$and PFE_T^{miss} relative to the recoil. This variable typically has a large value (1 or higher) for events in which PFE_T^{miss} is mismeasured. We require$\left|{E_T^{miss}}_{calo} - {E_T^{miss}}_{PF}\right| / U < 0.5$. The PF E_T^{miss} for events with the fake tracks can be very large.

9.3. AK4 Jets Reconstruction

We use jets reconstructed by clustering the particle flow candidates in the event using the anti-*kt* algorithm in this analysis. In the monojet analysis we use jets that are referred to as AK4 jets which were reconstructed with a distance parameter of 0.4. Only those charged particle flow candidates that are associated with the chosen primary vertex are used for clustering the jets (Charged Hadron Subtraction). In addition, we apply L1 correction in which jets are corrected for neutral particle from pileup interactions by using the event by event energy density estimation. L2 correction and L3 correction are also applied. These corrections are applied as a function of jet pseudo-rapidity (η) to equalize the jet energy response with respect to the central barrel region, and transverse momentum to equalize central jet response with respect to reference objects like leptonically decaying Z-bosons or prompt photons in γ+jets events. Moreover residual jet energy corrections are applied to jets in data to match their response with the simulation.

Sept23 re-reco residual corrections are used for data while Sprin16 MC-truth JECs are used to calibrate jets for simulated events. The AK4 jets considered in this analysis have p_{T}larger than 30 GeV and $|\eta| < 2.5$. The jets are subjected to the loose jet identification requirements as suggested by the Jet-MET POG. While we apply E_T^{miss} filters to remove a lot of fake E_T^{miss}events arising from detector noise and beam halo, we also need to implement additional cleaning to remove the residual background arising from anomalous jets. Charged hadron fraction > 0.1 and neutral hadron fraction < 0.8 requirements are applied on the leading AK4 jet to remove backgrounds due to detector noise and beam backgrounds.

9.4. B-tagged Jets Reconstruction

B-jets are defined and tagged by requiring the value of the "CombinedSecondaryVertexv2" (CSVv2) tagger to be bigger than 0.84 from the AK4 jets. While identifying *b*-jets, the adopted p_{T} threshold on the jets is set to 20

GeV and they should be inside the tracker coverage ($|\eta| < 2.4$). Events which includes b-jets are removed for this analysis in order to suppress tt and single top production (top backgrounds). The top background is thus reduced by a factor of 3 inside the SR. Efficiency corrections (b- tagging scale factors) are applied on the simulated samples as measured and recommended by the BTV group (CMS BTV POG).

9.5. Muons

Muon reconstruction and identification efficiency in both data and MC will be described in this section.

9.5.1. Muon Identification

Events containing muons are rejected in the analysis to suppress the electroweak backgrounds. Muon candidates must have a p_{T} of at least 10 GeV and $|\eta| < 2.4$. True muon events are determined by applying specific loose selection conditions (CMS Muon POG). which are as follows:

- Muon reconstructed as a global or tracker muon
- Muon reconstructed as a particle flow muon
- $\Delta\beta$ relative isolation less than 0.25

The isolation variable is calculated as the p_{T}sum of all PF charged hadrons associated to the primary vertex, PF neutral hadrons and PF photons in a ΔR cone ($\Delta R^2 = \Delta\eta^2 + \Delta\phi^2$) of 0.4 around the muon track. The isolation value is corrected for pileup by applying the $\Delta\beta$ correction and is taken relative to the p_{T} of the muon. Muons used in control samples are required to pass tighter identification criteria compared to those listed above (CMS Muon POG).
These are as follows:

- Muon reconstructed as a global muon
- Muon reconstructed as a particle flow muon
- Normalised χ^2 of the global track less than 10
- At least one muon chamber hit included in the global track fit
- Muon segments in at least two muon stations
- Transverse impact parameter w.r.t. the primary vertex less than 2 mm
- Longitudinal impact parameter w.r.t. the primary vertex less than 5 mm
- At least one pixel hit
- Hits on at least 5 tracker layers
- $\Delta\beta$ relative isolation less than 0.15

The efficiency of these selection requirements is measured separately in data and simulation using the tag and probe method, and accordingly scale factors are applied to the simulation. In the "tag and probe" method events with a pair of opposite-charged muons are considered. If one of the these muons passes tight selection criteria and is matched to the single muon trigger then it is considered a "tag muon" and even if the other muon pass the loose selection it is considered as a "probe muon" and it is used to test the selection efficiency. The mass of the tag-probe muon pair is required to be consistent with the Z boson peak. Events are then categorised as "passing" if the probe muon passes the selection requirements or "failing" if the probe muon fails the selection. The mass distribution of the tag and probe pair in data is fit to a resonance (representing the Z peak) sitting on a monotonically falling background. This is done separately for the passing and failing probes. The fit information can then be used to extract the number of prompt muons from the Z resonance that either pass or fail the selection requirements. This successively helps to establish the efficiency of the muon selection. Muon selection

efficiency can be computed for different ranges of muon p_T, muon η and number of vertexes (NPV) in the event.

The muon selection efficiency in simulation can be obtained directly from the generator-level information.The efficiency of the selection is given by:

$$E = (N_{pass}) / (N_{fail})$$

Here N_{pass} and N_{fail} are number of events with passing and failing probes respectively. Finally the scale factors are applied to the simulation and an overall 1% uncertainty is assigned on these scale factors. Figure 9.1 shows the data to MC scale factors measured for the loose muon identification criterion in low (NPV ≤17, left) and high pileup events (NPV ≥ 17, right). Instead, Figure 9.2 reports similar results for the tight identification working point.

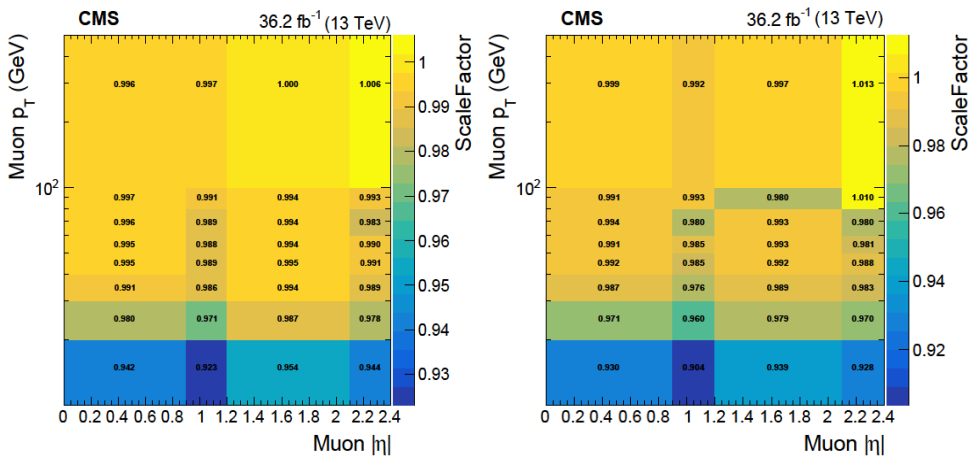

Figure 9. 1. Data-MC scale factors for the loose muon selection in events with NPV ≤17 (left) and NPV > 17 (right) measured as a function of muon p_T and η (Daci et al., 2016).

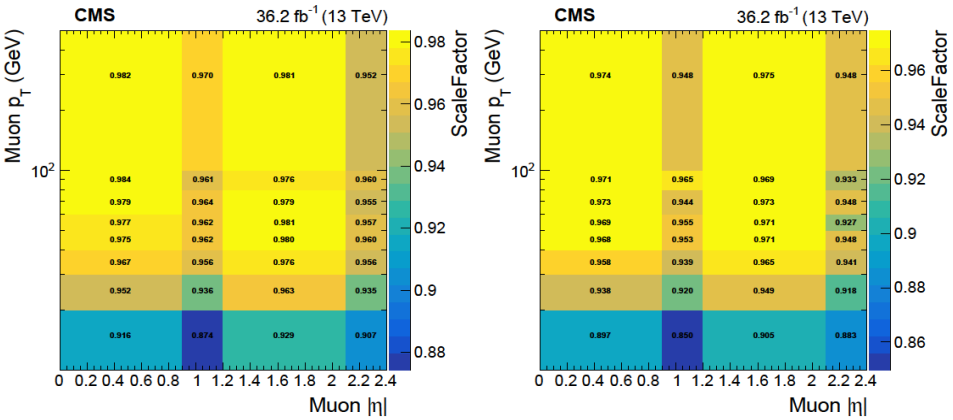

Figure 9. 2. Data-MC scale factors for the tight muon selection in events with NPV ≤ 17 (left) and NPV > 17 (right) measured as a function of muon p_T and η (Daci et al., 2016).

9.5.2. Muon Reconstruction

During data taking around 21 fb^{-1} from Run2016B to Run2016F, the tracking performance was strongly affected by deadtime in the silicon strip sensors bacause of Highly Ionizing Particles (HIPs), whose effect was raised by the large number of colliding bunches during 2016 data taking. This problem has been fixed in the second part of the data taking, starting from Run2016G. HIPs are known to lower the reconstruction efficiency for both muons and electrons, in addition lowering the *b*-tagging efficiency.

We measure the muon tracking efficiency using the "tag and probe" method on Z → μμ candidates separately in data and simulation for the full 2016 luminosity. Figure 9.3 shows the scale factors for the muon tracking efficiency in low ($NPV \leq 17$, left) and high pileup events (NPV ≥17, right). As expected, the inefficiency is larger for:

- Low p_T muon candidates.
- Muons in the barrel region (i.e. $|\eta| < 1.5$), because HIPs are mostly affecting the first two layers of TOB.

- Muons in events with a larger number of in-time interactions (pileup).

0.5% systematic uncertainty on the muon reconstruction scale factors in this analysis is assigned.

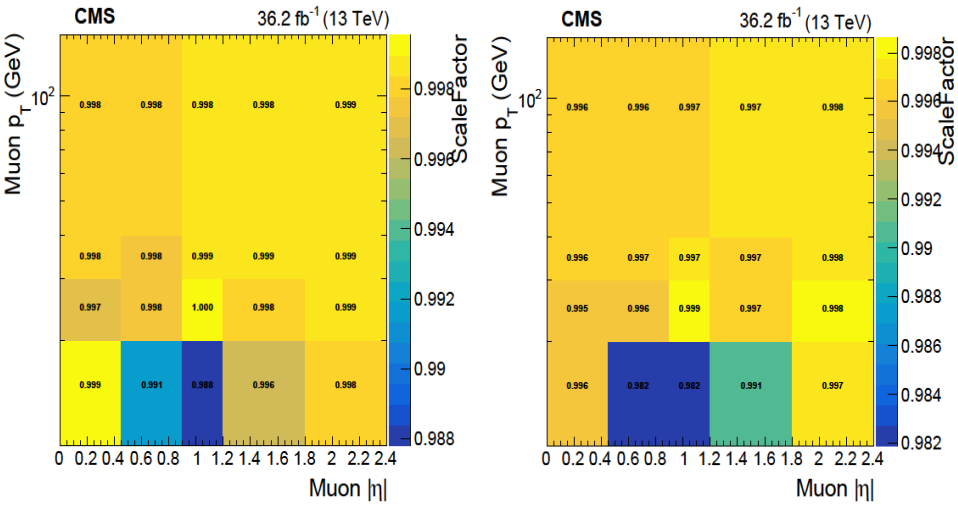

Figure 9. 3. Data-MC scale factors for the muon tracking efficiency in events with NPV ≤ 17 (left) and NPV > 17 (right) measured as a function of muon p_T and η (Daci et al., 2016).

9.6. Electrons

Electron reconstruction and identification efficiency in both data and MC are measured and descibed in this section.

9.6.1 Electron Identification

To suppress the electroweak backgrounds, well-reconstructed electrons events are vetoed. Electron candidates are required to have a minimum p_T of 10 GeV and $|\eta| < 2.5$. In order to identify real electrons in the event, loose identification and isolation is required (CMS EGamma POG).These are listed in Table 9.1.

Electrons are also used in defining certain CRs (W → eν and Z → ee) for estimating the key backgrounds in a data-driven manner. Electrons used in these

control samples are exposed to tighter identification and isolation requirements compared to those listed above (CMS EGamma POG). These are given in Table 9.2.

Table 9. 1. Loose electron identification criteria.

Variable	Selection (Barrel)	Selection (Endcaps)
Full 5x5 $\sigma_{i\eta i\eta}$	< 0.0115	< 0.0370
$\lvert\Delta\eta_{in}\rvert$	< 0.0749	< 0.0089
$\lvert\Delta\phi_{in}\rvert$	< 0.228	< 0.213
H/E	< 0.356	< 0.211
Relative isolation (ρ correction)	< 0.175	< 0.159
1/E - 1/p	< 0.229	< 0.150
$\lvert d_{xy}$ (vtx)$\rvert$	< 0.050	< 0.100
$\lvert d_z$ (vtx)$\rvert$	< 0.100	< 0.200
Expected Inner Missing Hits	<= 2	<= 3
Pass conversion veto	Yes	Yes

The electron efficiency is also measured with the “tag and probe” method that is similar to the case of the muons. The scale factors are taken from e-gamma POG covering the whole 2016 data taking period and defined with respect to Summer-16 MC. Further details can be found in the e-gamma twiki (CMS EGamma POG). Figure 9.4 shows the scale factors for the electron veto id (left) and tight id (right) as a function of the electron probe p_{T} and η. Overall an uncertainty of 2% on these scale factors used to correct electron identification efficiency.

Table 9. 2. Tight electron identification criteria and HLT safe selection.

Variable	Selection (Barrel)	Selection (Endcaps)
Full 5×5 $\sigma_{i\eta i\eta}$	< 0.00998	< 0.0292
$\lvert\Delta\eta_{in}\rvert$	< 0.00308	< 0.00605
$\lvert\Delta\phi_{in}\rvert$	< 0.0816	< 0.0394
H/E	< 0.0414	< 0.0641
Relative isolation (ρ correction)	< 0.0588	< 0.0571
Ecal PF cluster isolation	-	-
Hcal PF cluster isolation	-	-
Tracker isolation	-	-
χ^2 / ndf	-	-
1/E - 1/p	< 0.0129	< 0.0129
$\lvert d_{xy}$ (vtx)$\rvert$	< 0.050	< 0.100
$\lvert d_z$ (vtx)$\rvert$	< 0.100	< 0.200
Expected Inner Missing Hits	<= 2	<= 1
Pass conversion veto	Yes	Yes

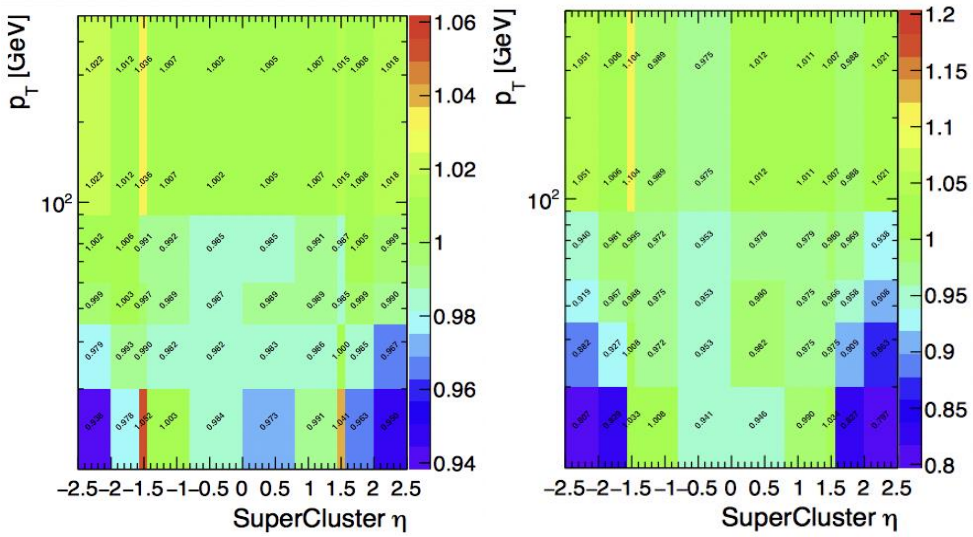

Figure 9. 4. Data-MC scale factors for the electron veto (left) and tight (right) identification criteria as measured in Z → ee events using a tag and probe method (Daci et al., 2016).

9.6.2. Electron Reconstruction

The scale factors for electron reconstraction are taken from e-gamma POG covering the whole 2016 data taking period and defined with respect to Summer-16 MC as reported in their twiki (CMS EGamma POG). Figure 9.5 shows the scale factors as a function of the electron probe p_{T} (left) and η (right). Overalll we assign a 1% systematic uncertainty on the electron reconstruction scale factors in this analysis as recomended by the POG.

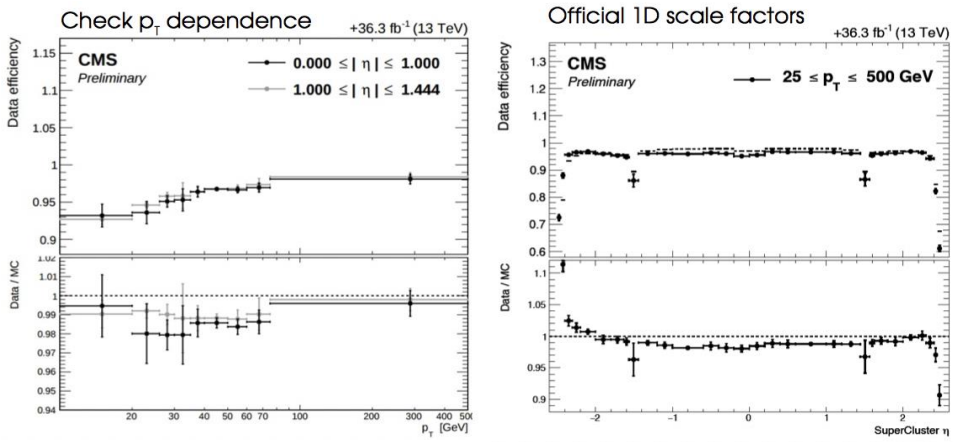

Figure 9. 5. Data-MC scale factors for the electron reconstruction efficiency as a funtion of probe p_{T} (left) and η (right) as measured in Z → ee events via a tag and probe method (Daci et al., 2016**)**.

9.7. Tau Reconstruction

Events which contain tau leptons are removed to suppress the electroweak backgrounds. The selection criteria for taus are as follows:

- $p_{\mathrm{T}} > 18$ GeV, $|\eta| < 2.3$.
- New DecayModeFinding
- Very loose MVA isolation working point provided by TAU POG (tau-POG) and labelled as “byVLooseIsolationMVArun2v1DBnewDMwLT”.

In addition to these criteria, TAU POG group have measured data to MC efficiency correction on $Z \rightarrow \tau\tau$ events for the chosen identification criteria, which is found to be 0.99 ± 0.05, then we use it to estimate our tau-veto uncertainty. Lastly, the muon and electron rejection vetoes are removed from the tau-id because leptons are vetoed in any case in the analysis selection.

9.8. Photons

To suppress backgrounds ($Z(\nu\nu)+\gamma$ + jet, $W(l\nu) + \gamma$ + jet) and to ensure clean separation from the mono-photon final state, the photon veto is applied in the analysis. If events with one or more photons with $p_T > 15$ GeV and $|\eta| < 2.5$ pass certain loose identification criteria, they are vetoed. The loose photon identification criteria is described in Table 9.3.

Table 9. 3. Loose photon identification criteria.

Variable	Selection (Barrel)	Selection (Endcaps)
Full 5x5 $\sigma_{i\eta i\eta}$	< 0.0103	< 0.0301
H/E	< 0.0597	< 0.0481
charged hadron isolation	< 1.295	< 1.011
neutral hadron isolation	$< 10.92 + 0.0148 \times p_T + 1.7 \times 10^{-5} \times p_T^2$	$< 5.931 + 0.0163 \times p_T + 1.4 \times 10^{-5}$ x p_T^2
photon isolation	$< 3.630 + 0.0053 \times p_T$	$< 6.541 + 0.0034 \times p_T$
Conversion safe electron veto	Yes	Yes

Photons which are used in the γ + jets CR to estimate the $Z(\nu\nu)$ + jets background, are selected by imposing tighter selection requirements as listed in Table 9.4. The photon p_T must be larger than 175 GeV in order to be consistent with the single photon trigger requirements. Also, these tight photons are required to be in the barrel ($|\eta| < 2.5$) to maintain high purity of the γ + jets sample.

Tag and probe method is used to measure the photon efficiency in Z boson decay. Here, the electrons are treated as photons by ignoring the matching requirements between the ECAL supercluster and the track. Figure 9.6 shows the photon efficiency for the tight selection measured in data and simulation as measured by the e-gamma POG relative to the Summer-16MC samples. In this analysis a 2% systematic uncertainty is assigned on the efficiency of the photon selection.

Table 9. 4. Tight photon identification criteria.

Variable	Selection (Barrel)
Full 5×5 $\sigma_{i\eta i\eta}$	< 0.0102
H/E	< 0.0396
charged hadron isolation	< 0.441
neutral hadron isolation	$< 5.931 + 0.0163 \times p_{\mathrm{T}} + 1.4 \times 10^{-5} \times p_T^2$
photon isolation	$< 2.571 + 0.0034 \times p_{\mathrm{T}}$
Conversion safe electron veto	Yes

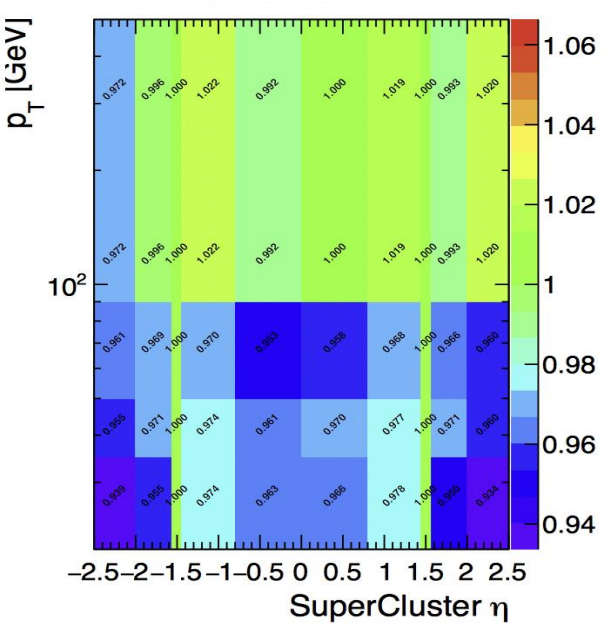

Figure 9. 6. The data-MC scale factors for the photon identification and isolation efficiency is measured by e-gamma POG as a function of photon probe p_{T} and η (Daci et al., 2016).

10. MONTE CARLO REWEIGHTING

Several corrections are applied to the simulation in order to match its prediction as closely as possible to data. We describe all the corrections and weights applied to several simulation processes in this section.

10.1. Pileup Reweighting for MC samples

The simulation of pileup conditions in the MC samples does not match with the one measured in data. Therefore, a re-weighting of the MC samples is essential to reproduce what is observed in data. It has been performed by matching the observed number of reconstructed vertices in a inclusive and high purity sample of $Z \rightarrow \mu\mu$ events.

10.2. Trigger Efficiency

We need to correct the simulated events to account for the L1+HLT trigger efficiency. The efficiency of all the triggers used in the analysis is measured directly in data. The measured efficiency is then applied as an event weight in simulation.

10.3. Lepton and Photon Efficiency and Reconstruction Scale Factors

Data - MC scale factors are obtained from the efficiencies that are measured for the electron, muon and photon selections in both data and simulation. Then these factors are applied to events in the five CRs used in the analysis. These CRs are single muon, single electron, double muon, double electron, and γ + jets.

10.4. NLO Corrections

The electroweak processes (Z + jets and W + jets) and γ + jets, play an highly significant role for backgrounds and CRs of the analysis. The MC samples for these EW processes have been produced at LO, in exclusive H_T bins. The NLO corrections

are applied event by event weights to the LO MC such that the generator-level distributions of the P_T of the Z,W, and γ match the corresponding NLO predictions. For W and Z, aMC@NLO is used to generate large simulation samples with 0, 1, or 2 additional partons at the NLO in QCD and matched to PYTHIA 8.2 parton shower through the FxFx algorithm (Frederix R. and Frixione S., 2012) in order to obtain NLO - QCD p_T distributions. In the same way, for γ + 1 jet, a sample is generated with aMC@NLO and showered with PYTHIA 8.2. In this case no additional parton is generated at the Born level.

We have used NNPDF 3.0 in 5-flavour scheme as the parton distribution function (PDF) set for all samples. The post shower p_T distributions of these samples are then compared to the corresponding distributions in the base LO MC simulation, after requiring the basic monojet like selections on the corresponding generator level objects (gen - leptons and gen-jets). The ratio of the NLO to LO is used as k-factors or weight as a function of p_T and is applied on the LO MC simulations.

The base samples thus corrected to NLO in QCD are further reweighted to include the reduction in the cross section at high p_T due to higher order EW effects, calculations of W + jets, Z + jets and γ + jets differential cross sections at NLO in QCD and in QCD+EW, presented in Refs. (Kallweit et al., 2015). Figure 10.1 shows the comparisons of the p_T distributions of the base MC, QCD NLO, and QCD+EW NLO.

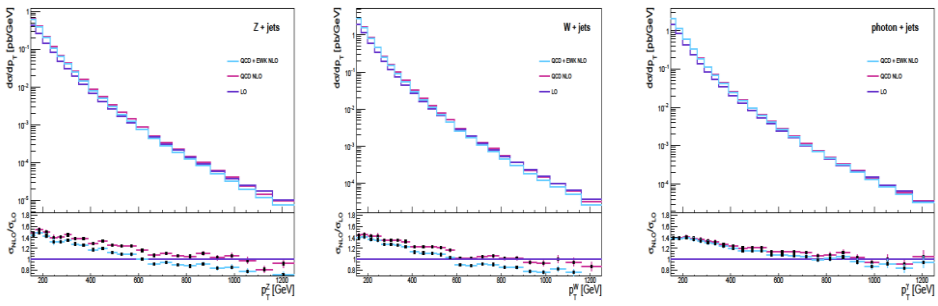

Figure 10. 1. NLO Higher-order corrections on the Z (left), W(middle), and photon (right) p_T distributions (Daci et al., 2016).

11. EVENT SELECTIONS

In this section we explain the selection used to describe events in the SR and CR. There are one SR and five CRs. These five CRs are single electron ($W \rightarrow e\nu$), single muon ($W \rightarrow \mu\nu$), double electron ($Z \rightarrow e^+e^-$), double muon ($Z \rightarrow \mu^+\mu^-$) and γ+jets and are used to estimate the main electroweak backgrounds processes. Background estimation procedure will be described in the next chapter. Data and MC samples were described in Chapter 7.

11.1. Signal Region

The following set of creteria are required for monojet categories in the SR.

- Events pass the E_T^{miss} triggers
- Events pass the E_T^{miss} filters to suppress detector noise and beam backgrounds
- Leading AK4 jet in the event has $p_T > 100$ GeV and $|\eta| < 2.5$
- Leading AK4 jet in the event passes the cleaning cuts
- $\Delta\varphi(\text{jet}, E_T^{miss}) > 0.5$ for the first four leading AK4 jets in the event to suppress QCD
- Require $\left|E_T^{miss}{}_{calo} - E_T^{miss}{}_{PF}\right| / E_T^{miss}{}_{\text{calo}} < 0.5$
- Lepton veto i.e. no loose electrons, muons or taus to suppress electroweak backgrounds
- Photon veto i.e. no loose photons to suppress electroweak backgrounds - Z(νν) γ+jets W(ℓν) γ+jets
- B-jet veto to suppress top background
- Recoil > 250 GeV because E_T^{miss} threshold consistent with the trigger turn-on

11.1.1. Kinematic Distributions in Signal Region

Distribution of the E_T^{miss} and p_T of the leading AK4 jets for events passing the monojet signal selection are shown in Figure 11.1. The number of jets and also the H_T distribution which is scalar sum of the p_T of all AK4 jets with $p_T > 30$ GeV and $|\eta| < 2.5$ are shown in Figure 11.2. Overall good agreement with data is observed.

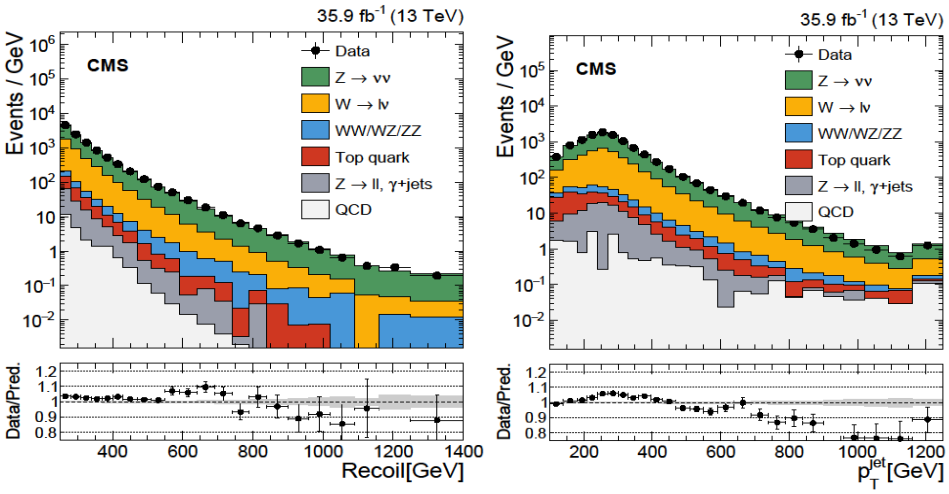

Figure 11. 1. Comparison of the recoil (left), and p_T distribution of the leading jet (right) for data and MC for the SR (Daci et al., 2016).

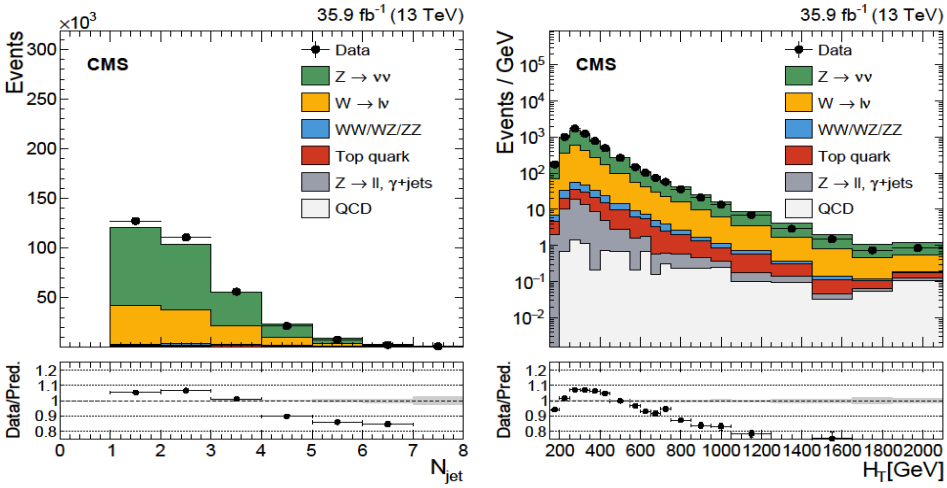

Figure 11. 2. Comparison of the AK4 jet multiplicity (left), and H_T distribution of the leading jet (right) for data and MC for the SR (Daci et al., 2016).

11.2. Control Regions

We applied almost same selection requirements and event categorisation for single muon, double muon, single electron, double electron and single photon CRs as it was for SR but with some differences. These differences are described below.

11.2.1. Single Muon Control Region

- Muon veto is relaxed
- Event must have one tight muon
- Transverse mass must be less than 160 GeV to reduce the QCD background which dominates the tails of the transverse mass distribution

Distributions of the recoil and p_T of the leading AK4 jets is shown in Figure 11.3. The number of jets and also the H_T distribution for events in the single muon CR are shown in Figure 11.4. Figure. 11.5 represents the comparison of the muon p_T and η distributions for data and MC in the single muon CR.

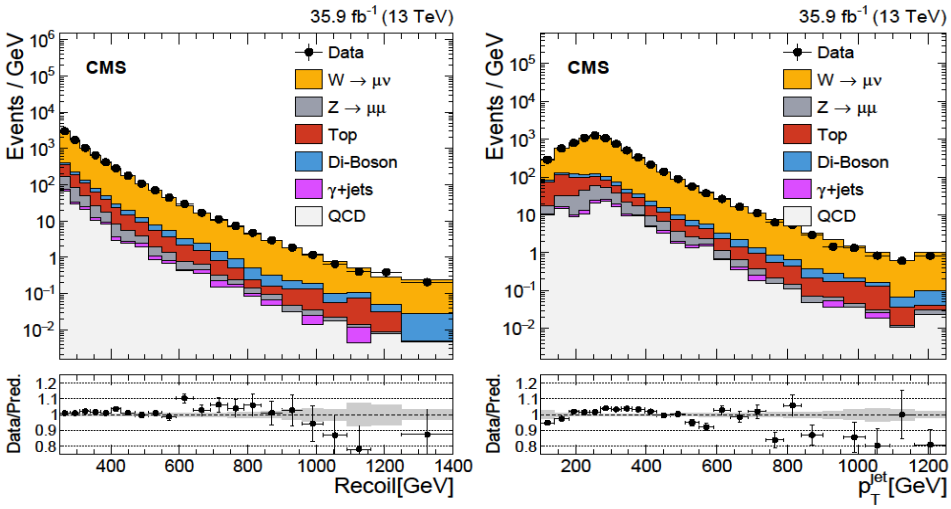

Figure 11. 3. Comparison of the recoil (left), and p_T distribution of the leading jet (right) for data and MC for the single muon CR (Daci et al., 2016).

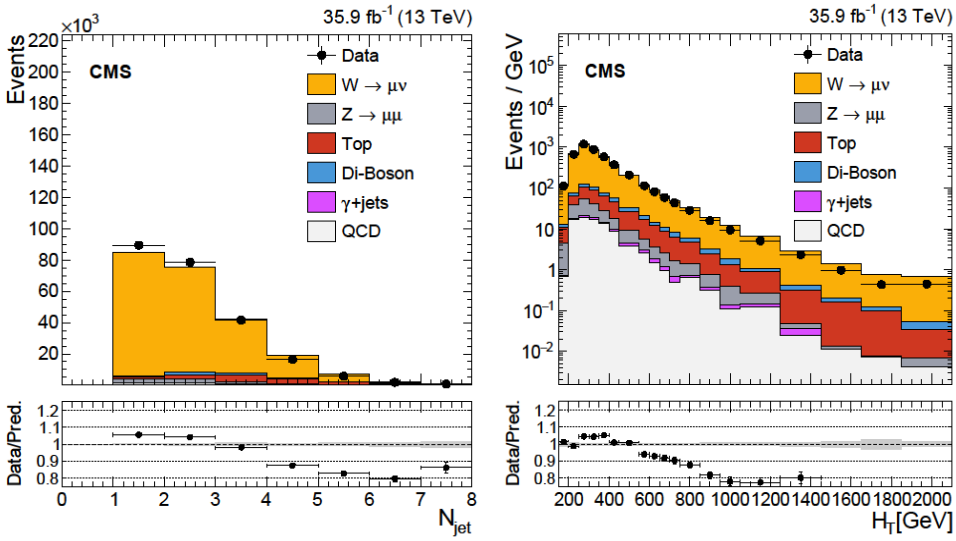

Figure 11. 4. Comparison of the AK4 jet multiplicity (left), and p_T distribution of the leading jet the H_T (right) for data and MC for the single muon CR (Daci et al., 2016).

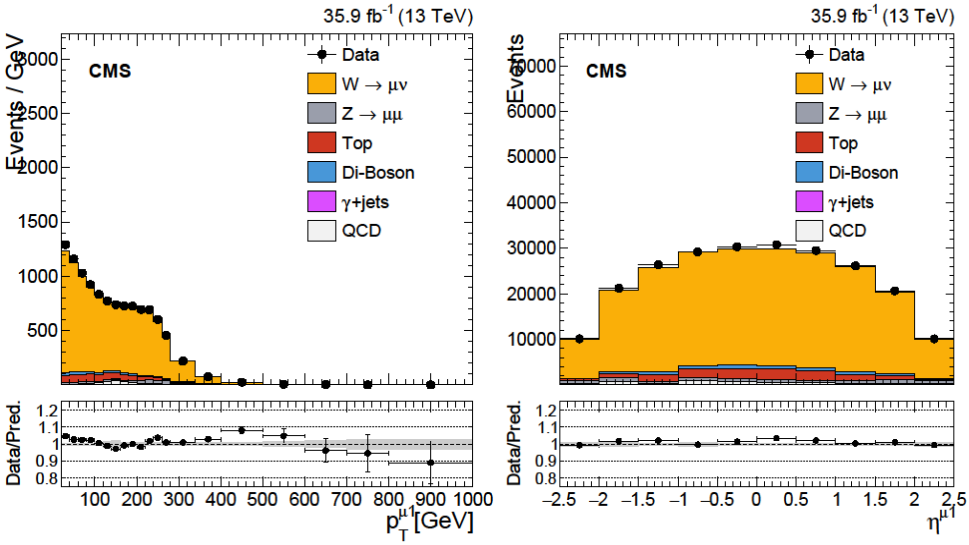

Figure 11. 5. Comparison of the muon p_T (left), and the muon η (right) distribution for data and MC for the single muon CR (Daci et al., 2016).

11.2.2. Single Electron Control Region

Events in the single electron CR are subjected to the same selection requirements and event categorisation as in the case of the SR with the following differences.

- We select events using single electron triggers shown in Table 8.1 and we discard electron veto
- Event must have one tight electron
- E_T^{miss} in the event must the larger than 50 GeV to suppress the QCD background

Distribution of the recoil and p_T of the leading AK4 jets are shown in Figure 11.6. The number of jets and the H_T distribution for events in the single electron CR are shown in Figure 11.7.

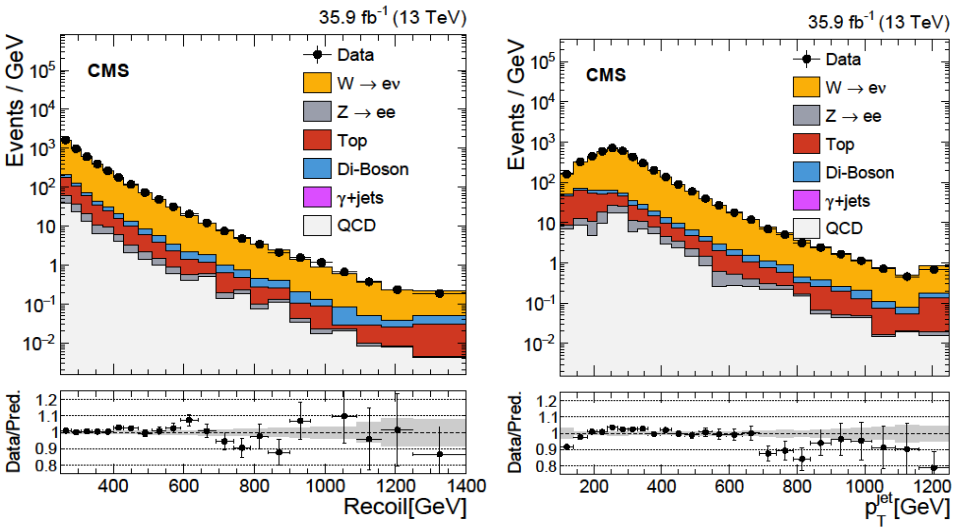

Figure 11. 6. Comparison of the recoil (left), and p_T distribution of the leading jet (right) for data and MC for the single electron CR (Daci et al., 2016).

Figure 11.8 represents the comparison of the electron p_T and η distributions for data and MC for the monojet in the single electron CR. The overall good agreement is observed between data and MC.

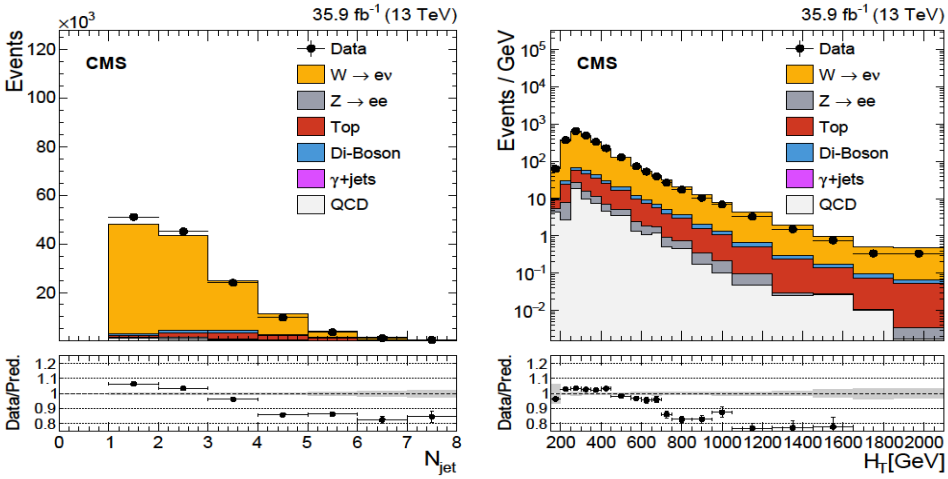

Figure 11. 7. Comparison of the AK4 jet multiplicity (left), and H_T distribution of the leading jet (right) for data and MC for the single electron CR (Daci et al., 2016).

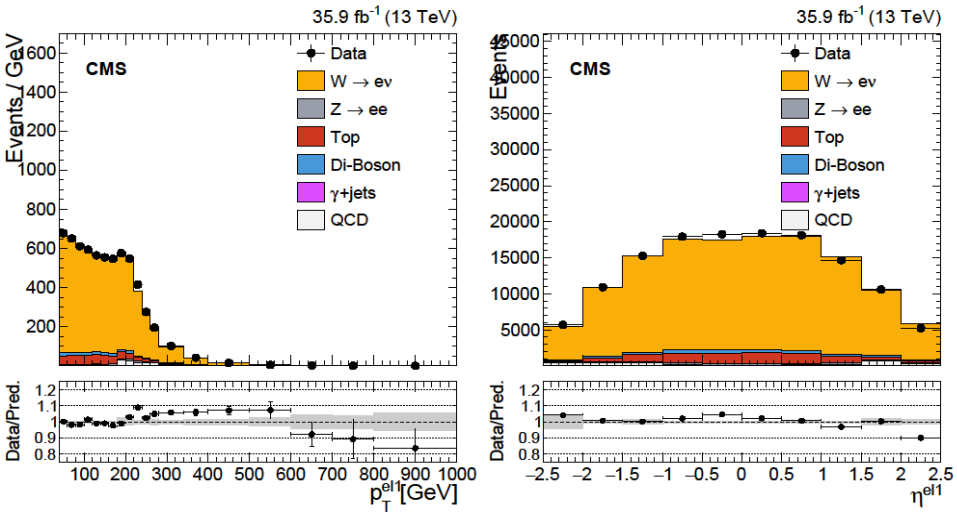

Figure 11. 8. Comparison of the electron p_T (left), and η (right) distributions for data and MC for the single electron CR (Daci et al., 2016).

11.2.3. Double Muon Control Region

Events in the double muon CR are subjected to the same selection requirements and event categorisation as in the case of the SR with the following differences.

- Muon veto is relaxed
- Event must have exactly two loose muons with opposite charge and at least one of the two muons passes the tight selection having a P_T larger than 20 GeV
- The invariant mass of the two muons should be between 60 GeV and 120 GeV

The di-muon mass and dimuon p_T distribution in the monojet of the double muon CR are shown in Figure 11.9. Distribution of the recoil and p_T of the leading AK4 jets for events in the double muon CR are shown in Figure 11.10. The number

of jets and the H_T distribution for the double muon CR are shown in Figure 11.11. Comparison between data and MC for the p_T and η distributions of the leading muon in dimuon events, for the monojet are shown in Figure 11.12. Similarly, Figure 11.13 shows comparison between data and MC for the p_T and η distributions of the subleading muon in dimuon events, in the monojet.

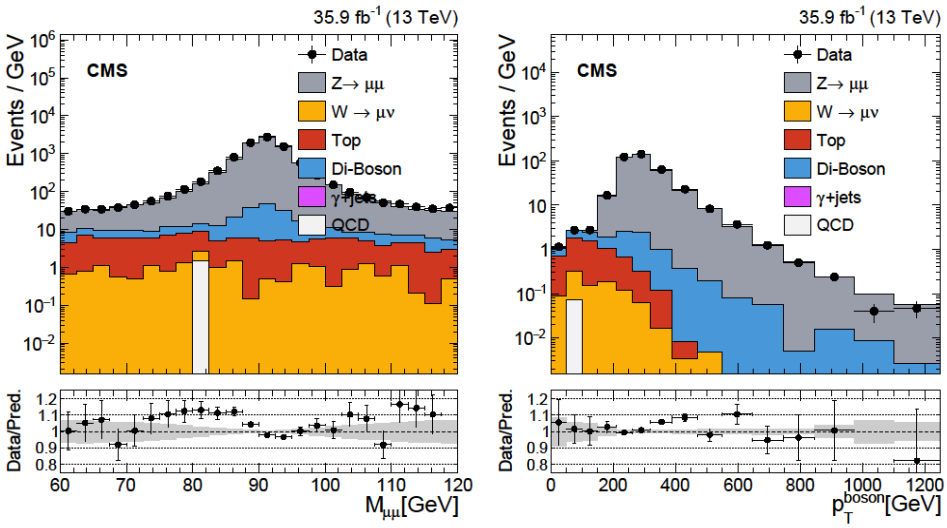

Figure 11. 9. Comparison of the dimuon mass (left), and dimuon p_T distribution (right) for data and MC for the double muon CR (Daci et al., 2016).

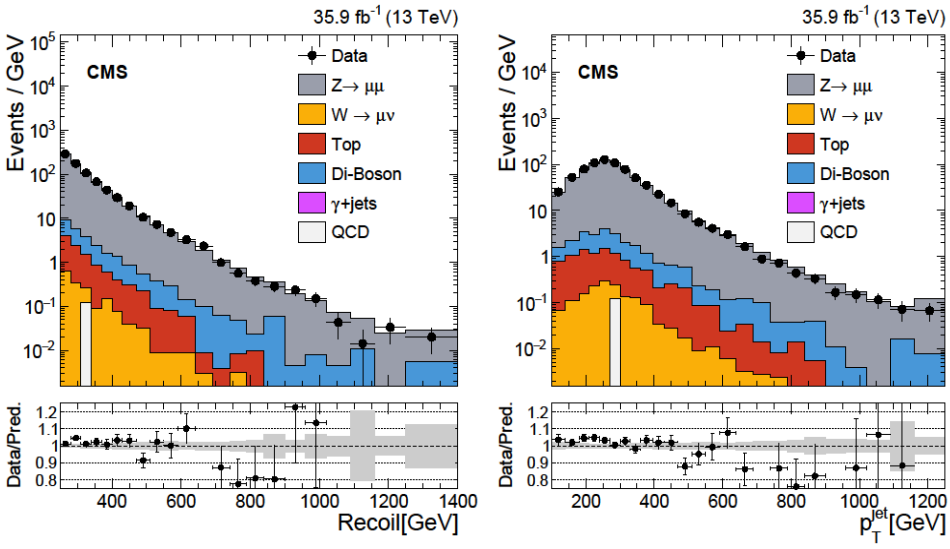

Figure 11. 10. Comparison of the recoil (left), and p_T distribution of the leading jet (right) for data and MC for the double muon CR (Daci et al., 2016).

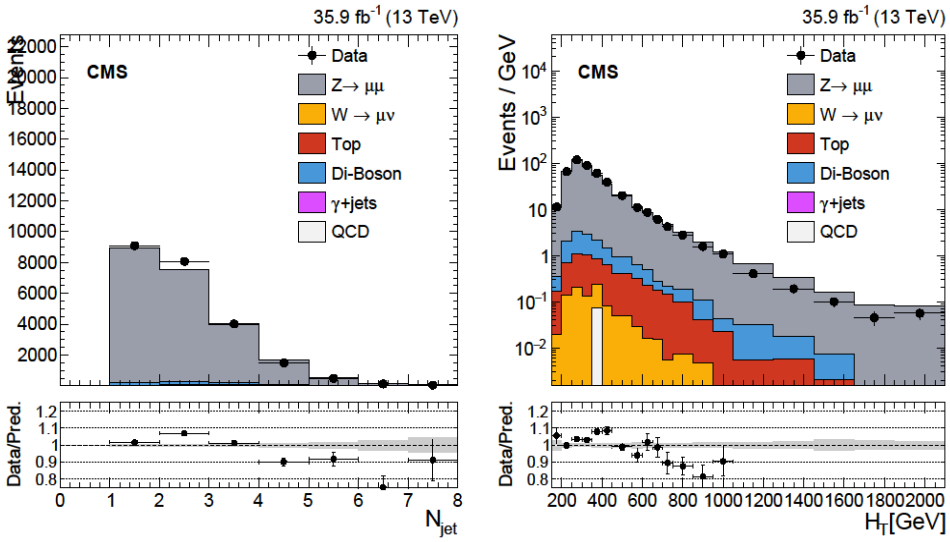

Figure 11. 11. Comparison of the AK4 jet multiplicity (left), and distribution of jet the H_T (right) for data and MC for the double muon CR (Daci et al., 2016).

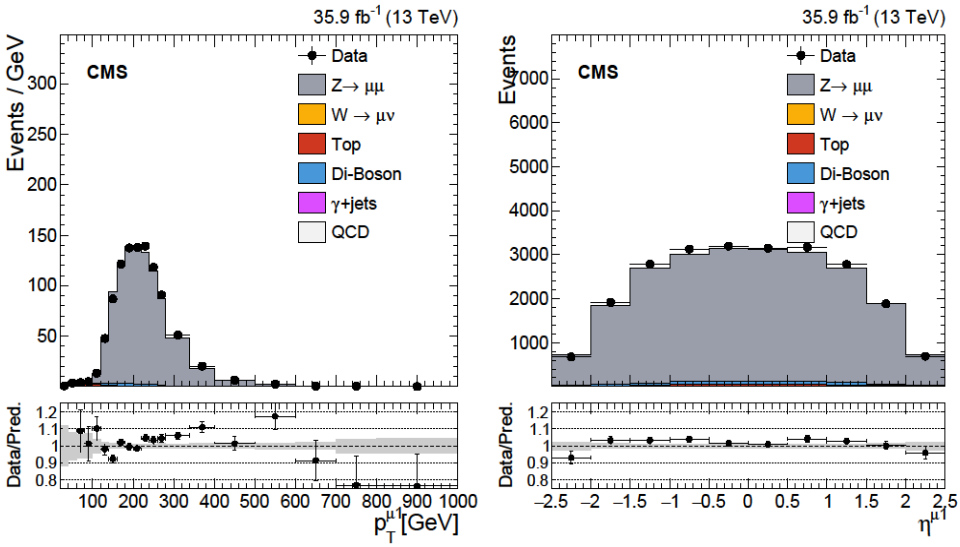

Figure 11. 12. Comparison of the leading muon p_T (left), and the leading muon η (right) distributions for data and MC for the double muon CR (Daci et al., 2016).

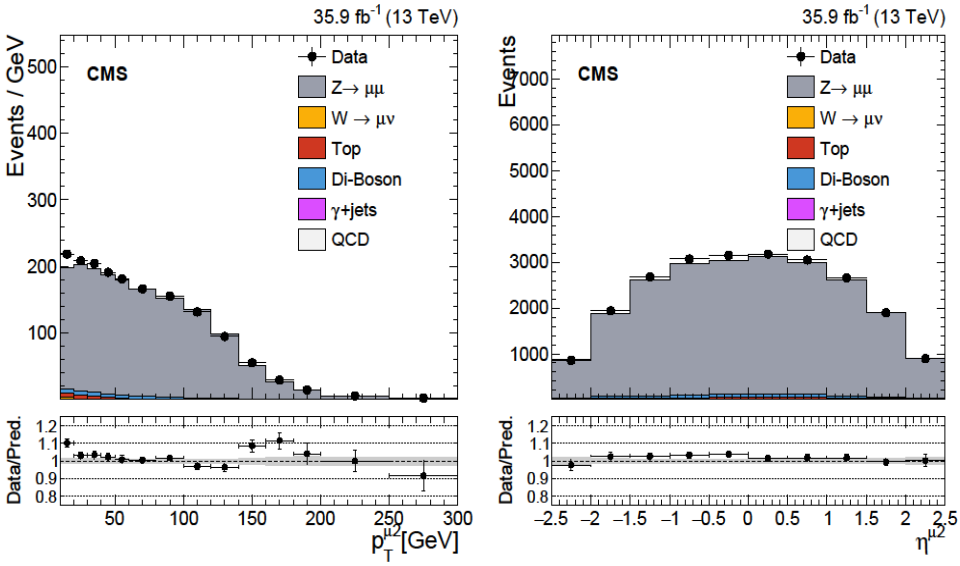

Figure 11. 13. Comparison of the subleading muon p_T (left), and the subleading muon η (right) distributions for data and MC for the double muon CR (Daci et al., 2016).

11.2.4. Double Electron Control Region

Events in the double electron CR are subjected to the same selection requirements and event categorisation as in the case of the SR with the following differences.

- Events are selected using the single electron triggers as shown in Table 8.1.
- Electron veto is relaxed
- Event must have exactly two loose electrons with opposite charge and at least one of the two electrons passes the tight selection with p_{T} larger than $40 \quad \mathrm{GeV}$
- The invariant mass of the two electrons sould be between 60 GeV and $120 \quad \mathrm{GeV}$

The di-electron mass and dielectron p_{T} distribution in the monojet of the double electron CR are shown in Figure 11.14. Distribution of the recoil and p_{T} of the leading AK4 jets for events in the double electron CR are shown in Figure 11.15. The number of jets and the H_{T} distribution for events in the monojet in the double electron CR are shown in Figure 11.16. Comparison between data and MC for the p_{T} and η distributions of the leading electron in dielectron events, in the monojet are shown in Figure 11.17. Similarly, Figure 11.18 shows comparison between data and MC for the p_{T} and η distributions of the subleading electron in dielectron events, in the monojet.

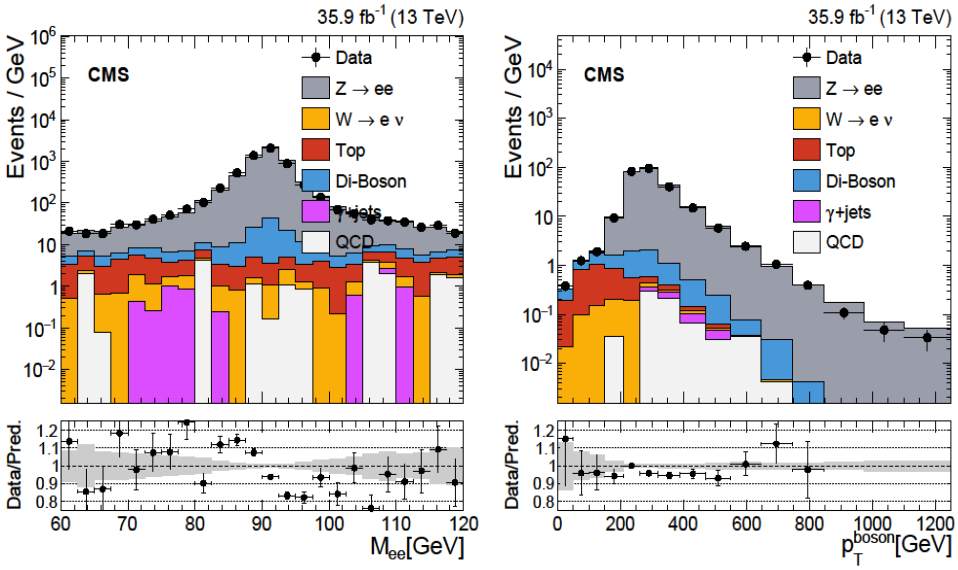

Figure 11. 14. Comparison of the dielectron mass (left), and dielectron p_T distribution (right) for data and MC for the double electron CR (Daci et al., 2016).

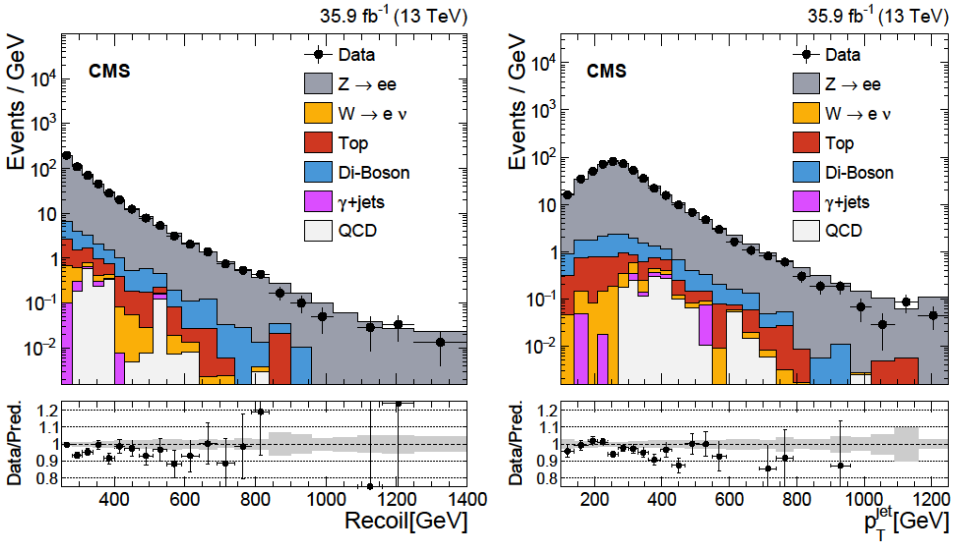

Figure 11. 15. Comparison of the recoil (left), and p_T distribution of the leading jet (right) for data and MC for the double electron CR (Daci et al., 2016).

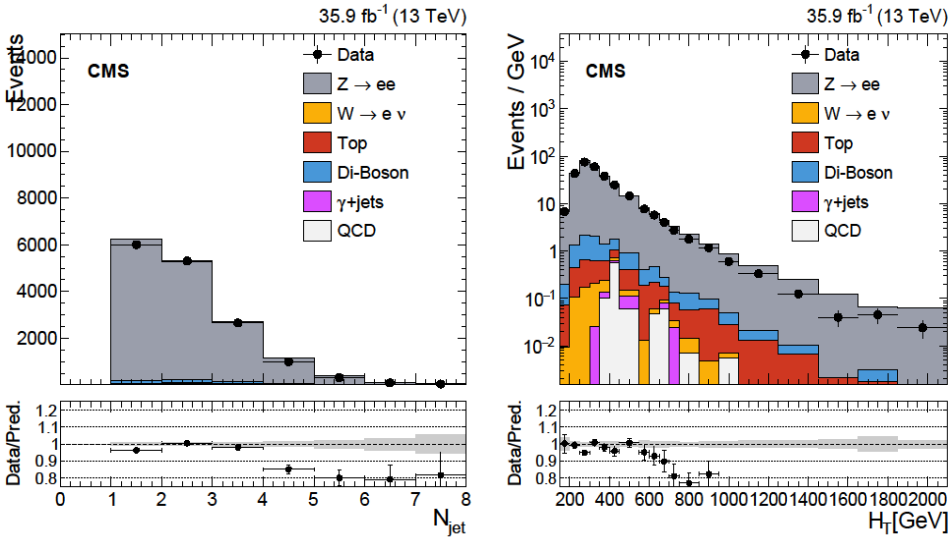

Figure 11. 16. Comparison of the AK4 jet multiplicity (left) and distribution of jet the H_T (right) for data and MC for the double electron CR (Daci et al., 2016).

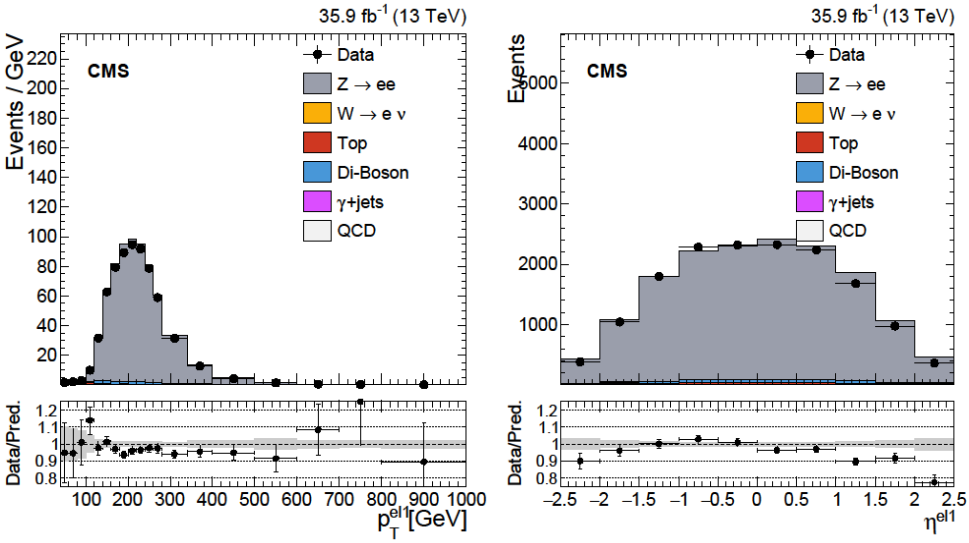

Figure 11. 17. Comparison of the leading electron p_T (left) and the leading electron η (right) distributions for data and MC for the double electron CR (Daci et al., 2016).

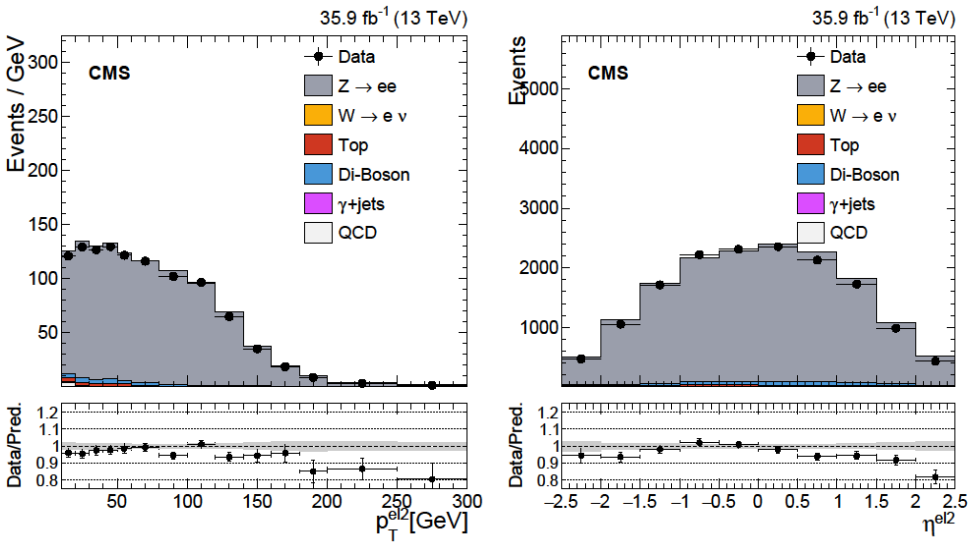

Figure 11. 18. Comparison of the subleading electron p_T (left) and the subleading electron η (right) distributions for data and MC for the double electron CR (Daci et al., 2016).

11.2.5. Photon+jets Control Region

Events in the γ+jets CR are subjected to the same selection requirements and event categorization as in the case of the SR with the following differences.

- We select events using the single photon trigger as shown in Table 8.1.
- Photon veto is relaxed
- Event must have exactly one loose photon which also passes the tight selection
- Photon P_T is larger than 175 GeV

Distribution of the recoil and p_T of the leading AK4 jets are shown in Figure 11.19. The number of jets and also the H_T distribution for events in the monojet in the single photon CR are shown in Figure 11.20. Comparison of photon p_T

distributions for data and MC in the monojet in the single photon CR are represented in Figure 11.21.

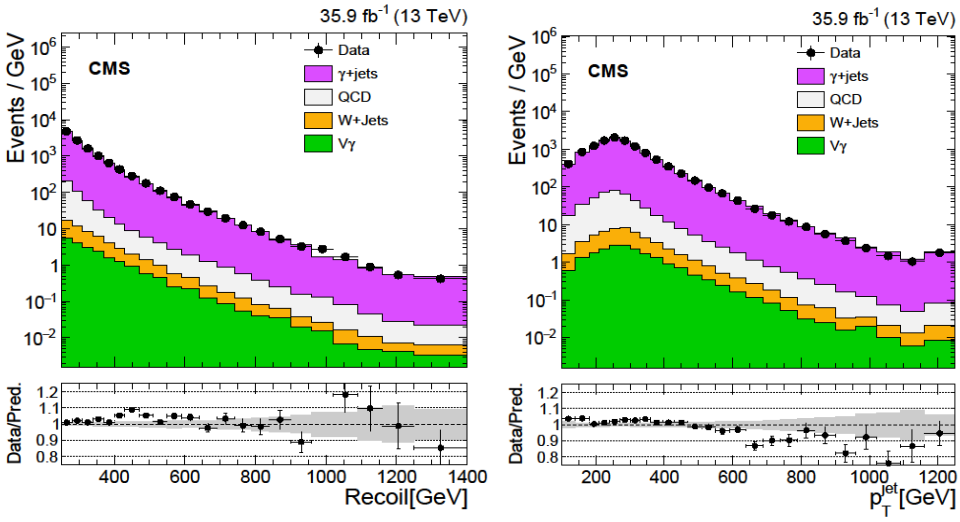

Figure 11. 19. Comparison of the recoil (left), and p_T distribution of the leading jet (right) for data and MC for the γ+jets CR (Daci et al., 2016).

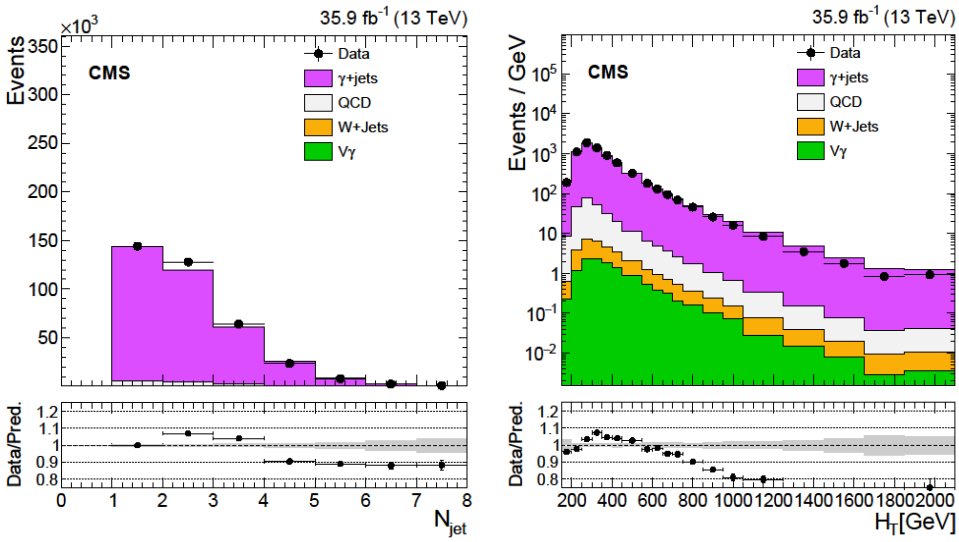

Figure 11. 20. Comparison of the AK4 jet multiplicity (left), and distribution of jet the H_T (right) for data and MC for the γ+jets CR (Daci et al., 2016).

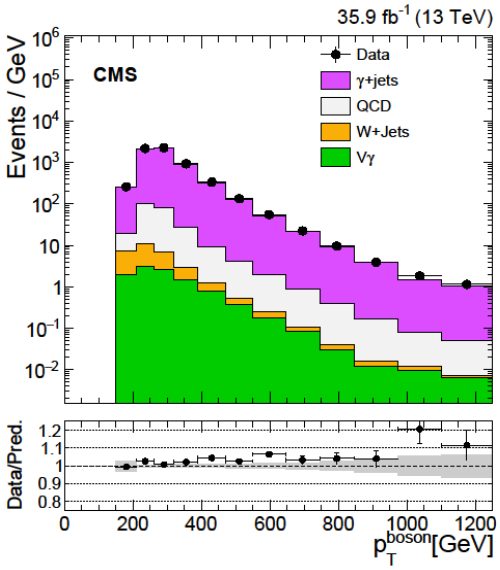

Figure 11. 21. Comparison of the photon p_T distribution for data and MC for the single photon CR (Daci et al., 2016).

12. BACKGROUND ESTIMATION

12.1. Sub-Dominant Backgrounds

Z(νν) + jets and W(*lν*) + jets are main backgrounds in this analysis. The five CRs were used for estimation of these backgrounds. There are also sub-dominant backgrounds in this analysis, namely, top (both tt and single-top), dibosons (WW, WZ, ZZ), QCD multijets, and Z(*ll*) + jets (where both leptons are lost). Except for the QCD multi-jet, all other sub-dominant backgrounds are estimated directly from simulation. We assign 20% uncertainty on the normalization of these backgrounds in monojet. In the case of the QCD background, we use the Δφ extrapolation method to estimate the QCD background.

12.2. Electroweak Background Estimation

The estimations of the two leading backgrounds, namely Z → νν+jets and W+jets, are derived from a combined maximum likelihood fit of the five CRs in data as well as the SR. All sources of systematic uncertainty in the background prediction are used in the fit. The fit also takes into account both shape and normalisation uncertainties. The shape uncertainties are based on several sources such as theory uncertainties, e.g QCD scale, PDF, NLO-EW correction on the estimates of the cross-sections, as well as uncertainties from the reconstructed objects such as jet energy scale and jet energy resolution. The normalisation uncertainties occur as a result of cross-section and luminosity uncertainties for MC-driven backgrounds, in addition uncertainties in the lepton, photon reconstruction in the CRs, and the bjet veto.

12.3. Procedure

For all CRs, we first compute the recoil variable *U* where we removed either the photon, the muons, or electrons from the E_T^{miss} calculation as described in chapter

9.2. Next, transfer factors (R) are computed using LO MC and corrected with NLO(QCD+EW) k-factors that relate the yields between a given CR and a certain background in the SR for every bin of the recoil distribution. The Equation 12.2 is used to derive the transfer factor R to go from the dimuon CR to the Z → νν background in the SR.

$$R_i^Z = \frac{N_{i,MC}^{Z\to\mu^+\mu^-}}{N_{i,MC}^{Z\to\nu\nu}} \tag{12.2}$$

where N_i is the number of events in the ith bin of the recoil distribution, R_i is the transfer factor between the dimuon CR and Z → νν background. Other transfer factors are calculated in an analogous manner. We consider five transfer factors:

Table 12. 1. Five CRs for background estimation.

dimuon CR	Z→νν background
dielectron CR	Z→ νν background
γ+jets CR	Z→ νν background
single muon CR	W+jets background
electron CR	W+jets background

We also use a constrain that connects the Z → νν background SR to W + jets background in the SR. In order to extract the background estimation, a combined maximum likelihood fit is performed using a likelihood that is given in Equation 12.3:

$$\begin{aligned} L_c(\mu_i^{Z\to\nu\nu}, \mu, \theta) = & \prod_i Poisson\left(d_i^\gamma \mid B_i^\gamma(\theta) + \frac{\mu_i^{Z\to\nu\nu}}{R_i^\gamma(\theta)}\right) \\ & \times \prod_i Poisson\left(d_i^Z \mid B_i^Z(\theta) + \frac{\mu_i^{Z\to\nu\nu}}{R_i^Z(\theta)}\right) \\ & \times \prod_i Poisson\left(d_i^W \mid B_i^W(\theta) + \frac{\mu_i^{Z\to\nu\nu}}{R_i^W(\theta)}\right) \\ & \times \prod_i Poisson\left(d_i \mid B_i(\theta) + \left(1 + f_i(\theta)\right)\mu_i^{Z\to\nu\nu} + \mu S_i(\theta)\right) \end{aligned} \tag{12.3}$$

Where $d_i^{\gamma/Z/W}$ are the observed number of events in each recoil bin of the photon, dimuon/dielectron and single-muon/single-electron CRs, $B_i^{\gamma/Z/W}$ is the number of events for background in the respective CRs. $R_i^{\gamma/Z/W}(\theta)$ is transfer factor for each CR and θ represents systematic uncertainties appearing as additive perturbations to the transfer factors and are modelled as Gaussians. The parameter $\mu_i^{Z\to\nu\nu}$ represents the yield of Z → νν background in the *i*th recoil bin into the SR, and is left freely floating in the fit. The function $f_i(\theta)$ is the transfer factor between the Z → νν and W+jets backgrounds in the SR and represents a constraint between these backgrounds. The likelihood also includes the SR with $B_i(\theta)$ representing all the backgrounds, $S_i(\theta)$ representing the nominal signal prediction, and μ being the signal strength parameter also left floating in the fit.

12.4. Transfer Factors

The dominant background in the monojet final state originates in the Z→νν production. This background is mimic the DM final state in that it comprises a boson, the Z(νν) boson, decaying into invisible particles. The only meaning of discriminating against this background source is identifying characteristic features of the initial state radiation which differs for the boson and the DM production.

To model the Z(νν) boson background in monojet final states, the following three CR are used: dimuon, dielectron and single photon. The dimuon CR comprises a clean Z(νν) boson signature with similar acceptances to the Z → νν background, the production mode and kinematics in the CRs are very similar to the SR. At the same time, the dimuon control sample comprises about 10% of the number of Z(νν) + jets events in the SR. The analysis is limited in the statistical knowledge of $Z \to$ μμ in modelling the Z → νν background. Figure 12.1a shows transfer factor between the dimuon CR and the Z → νν background. The transfer factor is close to 9, implying that with the dimuon CR alone, the analysis is systematically limited to an uncertainty 3 times larger than the statistical precision of the analysis.

The dielectron CR is similar to the dimuon, so we use it to model the Z boson background in the SR, as it was done for the dimuon sample. Figure 12.1b shows the transfer factor for going from Z → ee to Z → νν. Dielectron and dimuon transfer factors value are different in the absolute due to trigger, identification efficiency (typically a tight electron selection is 70-75% efficient, while a tight muon has an efficiency close to 90%) and differences in the lepton p_T requirement (20 GeV for muons, 40 GeV for electrons).

The photon CR ensures the dominant constraint on the high p_T Z → νν back ground owing to its large yield even at high boson p_T. The production of γ+jets events has only one additional background, that is to say QCD events where a jet is mis-reconstructed as a photon. Figure 12.1c shows the ratio of Z → νν events to γ+jets events. The yield from γ+jets events is approximately 2 times that of the boson yield.

The W → ℓν process is second largest background in the SR which comes from W bosons where either a lepton is not reconstructed or is found outside of the signal acceptance. To model the W boson background, single muon and single electron CR is added to the analysis to estimate the W bosons in the SR. The lepton is removed from the E_T^{miss} for yielding the hadronic recoil U. Figures 12.2a, 12.2b show the transfer factor for the single lepton region to the W + jets background in the CR. The value of the transfer factor is less than 1 for $U > 30$ GeV, which is the sensitive region for the analysis. This allows for a constraint that is lower than the implicit statistical uncertainty on the W+jets in the SR.

Finally, we used W → ℓν background to estimate Z → νν background in SR and define respective transfer factor. Figure 12.3 shows the transfer factor for going from the W → ℓν background to the Z→ νν background in the SR.

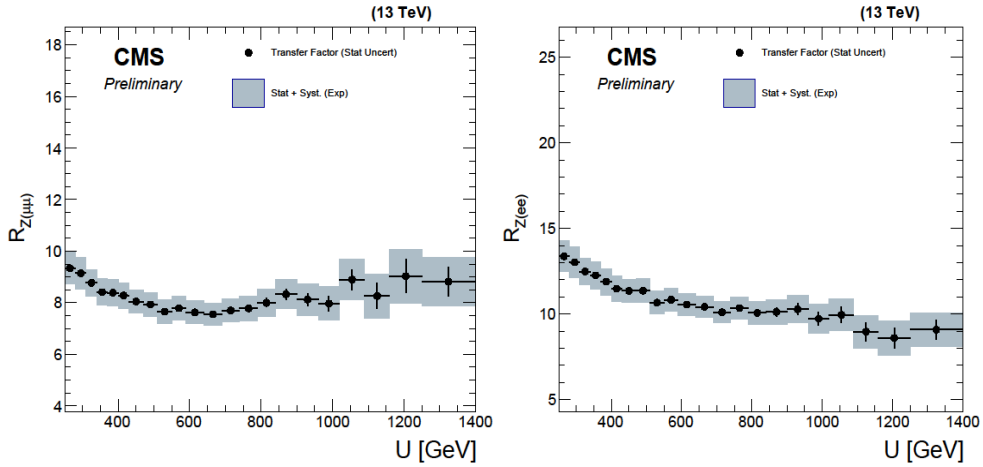

(a)

(b)

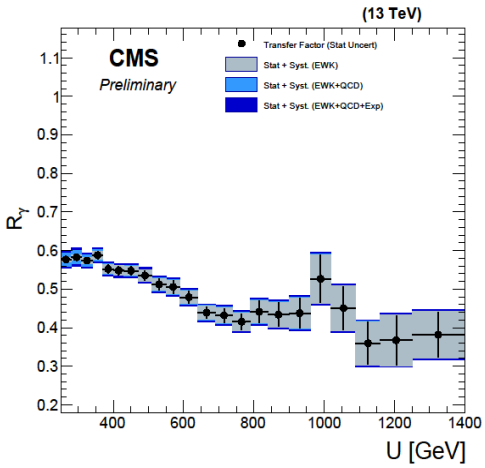

(c)

Figure 12. 1. Transfer factors for the Z→ νν background as a function of the recoil using the dimuon (a), dielectron (b) and photon (c) CR in monojet final state (Daci et al., 2016).

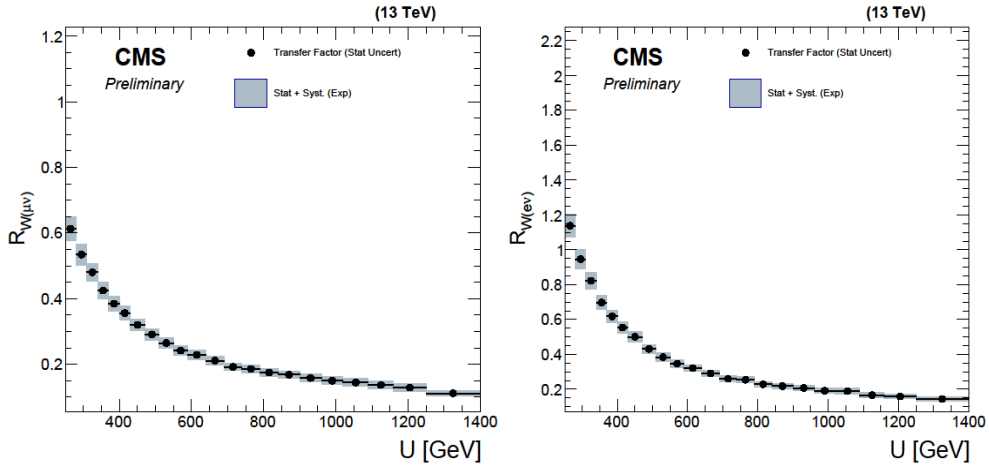

Figure 12. 2. Transfer factors for the W → ℓν background as a function of the *U* using the single muon (left) and single electron (right) CR for the monojet final state.

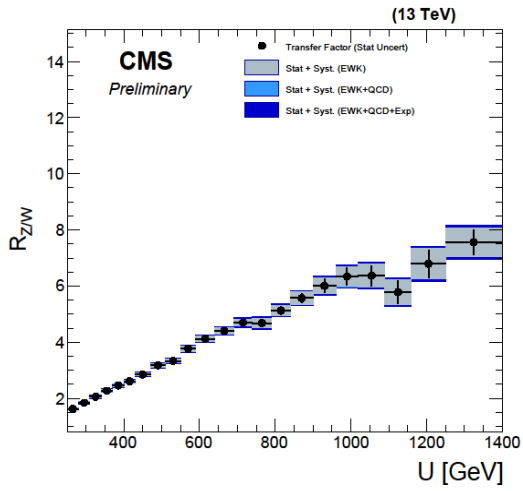

Figure 12. 3. Transfer factors for to estimate the Z(νν)+jets background from W+jets in the SR as a function of the recoil for the monojet final state (Daci et al., 2016).

13. UNCERTAINTIES

13.1. Experimental Uncertainties on Transfer Factors

Table 13.1 shows a summary of the experimental uncertainties contained in the transfer factors. Since no experimental uncertainties are affecting the Z/W ratio in the SR, except for the lepton veto, no transfer factors are included in the Table 13.1 for this ratio. Jet energy scale and jet energy resolution systematics are not affecting the transfer factors since their hadronic content is almost identical for SR and CRs.

Table 13. 1. Experimental uncertainties affecting transfer factors used in the analysis to estimate (W, Z, γ)+jets backgrounds in the SR (Daci et al., 2016).

Source	Process	Uncertainty
Electron trigger	$W_{SR}/W_{e\nu}$, $Z_{\nu\nu}/Z_{ee}$	1%
Photon trigger	$Z_{\nu\nu}/\gamma$	1%
E_T^{miss}	$W_{SR}/We\nu$, $Z_{\nu\nu}/Z_{ee}$, $Z_{\nu\nu}/Z_{\mu\mu}$, $W_{SR}/W_{\mu\nu}$, $Z_{\nu\nu}/\gamma$	shape vs E_T^{miss}
Muon-reco efficiency	$W_{SR}/W_{\mu\nu}$, $Z_{\nu\nu}/Z_{\mu\mu}$	1% (per leg)
Muon-ID efficiency	$W_{SR}/W_{\mu\nu}$, $Z_{\nu\nu}/Z_{\mu\mu}$	1% (per leg)
Electron-reco efficiency	$W_{SR}/W_{e\nu}$, $Z_{\nu\nu}/Z_{ee}$	1% (per leg)
Electron-ID efficiency	$W_{SR}/W_{e\nu}$, $Z_{\nu\nu}/Z_{ee}$	2% (per leg)
Photon-ID efficiency	$Z_{\nu\nu}/\gamma$	2%
Muon veto	$W_{SR}/W_{e\nu}$, $W_{SR}/W_{e\nu}$, Z/W	shape vs E_T^{miss}
Electron veto	$W_{SR}/W_{e\nu}$, $W_{SR}/W_{e\nu}$, Z/W	shape vs E_T^{miss}
Tau veto	$W_{SR}/W_{e\nu}$, $W_{SR}/W_{e\nu}$, Z/W	shape vs E_T^{miss}

Since we have measured an inefficiency at the HLT-level in the PF-muon assignment, a conservative systematic uncertainty taken as the full difference between the E_T^{miss} trigger turn-ons measured in dimuon Z ($\mu^+\mu^-$) and single muon W($\mu\nu$) events, as reported in previous sections, is assigned to all transfer factors. The

variation in uncertainties as a function of the hadronic recoil of the event is decreasing from 2% at 250 GeV to few per-mille for E_T^{miss} grater than 500 GeV.

13.2. Theoretical Uncertainties on Transfer Factors

The PDF uncertainties, QCD higher-order corrections, and the EW corrections are propagated into the transfer factors. To calculate the PDF uncertainty, the QCD NLO samples are reweighted with the event by event scale factors that represent the shift in kinematic distributions from variations in the PDF. These scale factors are computed at the event generation level for each 1 unit variation of the eigenvectors of the PDF fit. Reweighted p_{T} distributions and thus the transfer factors are produced for each eigenvector variation, and the RMS of the transfer factor variation is taken as the PDF uncertainty. NLO re-weighting is calculated using Equation 13.1.

$$\frac{d\sigma_{NLO}}{dp_T^V}\left(\vec{\varepsilon}_{\mathrm{QCD}}, \varepsilon_{\mathrm{mix}}, \vec{\varepsilon}_{\mathrm{EW}}\right) = \left[K_{\mathrm{NLO,QCD}}\left(\vec{\varepsilon}_{\mathrm{QCD}}\right) . \left(1 + K\mathrm{EW}\left(\vec{\varepsilon}_{\mathrm{EW}}\right)\right) + \varepsilon_{\mathrm{mix}}\, \delta\, K_{\mathrm{mix}}\right] \times \frac{d\sigma_{LO}}{dp_T^V}(\vec{\mu}_0) \quad (13.1)$$

$K_{\mathrm{NLO,QCD}}\left(\vec{\varepsilon}_{\mathrm{QCD}}\right)$ represents the NLO-QCD corrections (k-factor). It depends on a set of different $\vec{\varepsilon}_{\mathrm{QCD}}$ according to:

$$K_{\mathrm{NLO,QCD}}\left(\vec{\varepsilon}_{\mathrm{QCD}}\right) = K_{\mathrm{NLO,QCD}}\left(\vec{\mu}_0\right) + \sum_{i=0}^{3} \varepsilon_{QCD,i}\, X\, \delta^i\, K_{\mathrm{NLO,QCD}} \quad (13.2)$$

- $\delta^1 K_{\mathrm{NLO,QCD}}$ is represented by the standard 7-point factor-two variations around the central renormalization and factorization scale values $(\mu_R = \mu_F = \mu_0)$.
- $\delta^2 K_{\mathrm{NLO,QCD}}$ is the so called "QCD shape uncertainty". Constant scale variations mainly affect the overall normalization of single processes, underestimating shape uncertainties, which play an important role to extrapolate low $\boldsymbol{p}_{\mathbf{T}}$ measurement to the high $\boldsymbol{p}_{\mathbf{T}}$ region.

- $\delta^3 K_{\text{NLO,QCD}}$ is a process-dependent uncertainty specifically derived for Z+jets, W+jets and γ+jets, as the difference between the NLO k-factor of each process wrt the Z → $\ell\ell$+jets.

We consider all these nuisance parameters as fully correlated across E_T^{miss} bins, as well as across different processes (Z,W,γ).

The $\vec{\varepsilon}_{\text{QCD}}$ parameters should be Gaussian distributed with one standard deviation corresponding to the range $\vec{\varepsilon}_{\text{QCD}} \in [-1,+1]$. Figure 13.1 (a) shows the standard NLO-QCD uncertainty from the 7-point scale variations for Z+jets,W+jets and γ. Additionally, Figure 13.2 (b) shows the "QCD shape uncertainty" for each individual Z+jets, W+jets and γ process, while Figure 13.3 (c) shows the process dependent uncertainty.

K_{EW} ($\vec{\varepsilon}_{\text{EW}}$) in Equation. 13.1 represents the pure NLO-EW correction which can be parametrised as:

$$K_{\text{EW}}(\vec{\varepsilon}_{\text{EW}}) = [1 + K_{\text{NLO-EW}} + K_{\text{NLO-Sud}}] + \sum_{i=0}^{3} \varepsilon_{EW,i} \times \delta^{i}{}_{\text{EW}} \qquad (13.3)$$

where $K_{\text{NLO-EW}}$ indicates the NLO-EW corrections for virtual photon and quark bremsstrahlung, no photon induced production, while $K_{\text{NNLO-Sud}}$ demonstrates the NNLO Sudakov terms which have a sizable effect at high p_{T}. The three nuisance parameters ($\varepsilon_{\text{EW,i}}$) taken into account are given below:

- Unknown Sudakov logs in the perturbative expansion beyond NNLO, which is one of the most important source of EW uncertainties at high p_{T}.
- Missing NNLO effects which are not absorbed by the NLL. They are estimated to be as large as 5% of the full NLO EW correction.
- The difference between the NLL Sudakov approximation and a naive exponentiation of the full NLO EW correction is taken as a conservative systematic uncertainty.

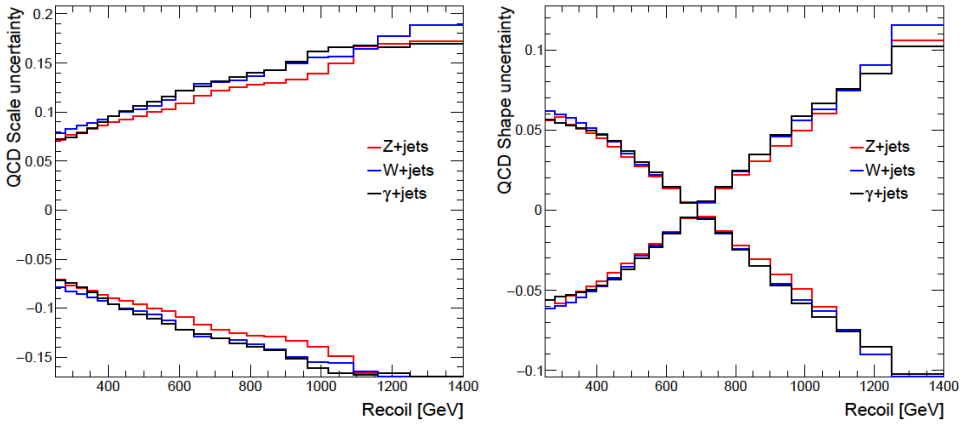

(a)

(b)

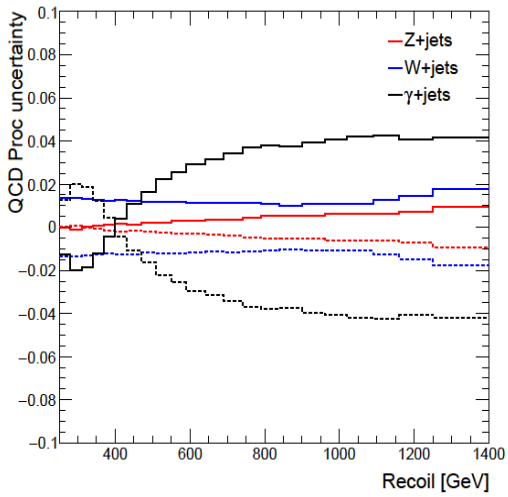

(c)

Figure 13. 1. QCD scale uncertainty as a function of U is displayed in (a) for the different V+jets processes, while (b) and (c) show the "QCD shape" and the "process dependent" uncertainty, respectively. Note that the process dependent uncertainty for W+jets and γ+jets are not onesided. Solid (dashed) lines in (c) are showing the positive (negative) one sigma shift of the related nuisance, which can cross zero as a function of p_T (Daci et al., 2016).

Finally, the last nuisance (ε_{mix}), is combination of higher order QCD and EW corrections which is given in Equation 13.1. δK_{mix} represents the uncertainty due to non factorise EW-QCD effects.

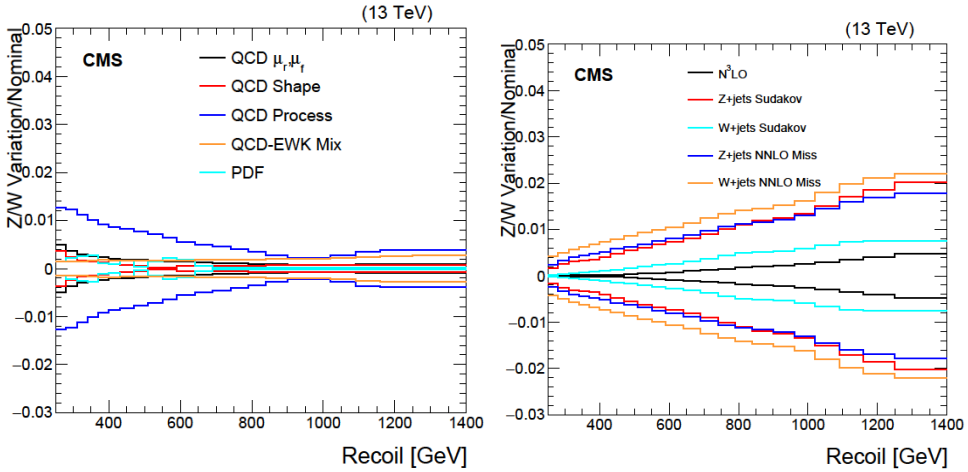

Figure 13. 2. Theoretical uncertainties on the Z/W transfer factors (left) nuisances related to the NLO-QCD re-weight + the mixing between QCD and EW corrections, (right) effect of the nuisance parameters related to NLO EW corrections (Daci et al., 2016).

Figure 13.2 shows the uncertainties on Z/W ratios of the recoil distributions according the prescription coming from the theorist. The left plot shows the impact of the following nuisances: QCD scale (black line) and QCD shape (red line) uncertainties decrease with p_{T} from 0.5% to few per-mille, while PDF and EW-QCD mixing are almost negligible. The largest uncertainty at low p_{T} is represented by the so called QCD process dependent nuisance, which varies from 1.5 to 0.5%. On the contrary, Figure 13.3 shows the impact of NLO EW uncertainties. The effect of mentioned all three Sudakov uncertainties are the dominating at high p_{T} , which can reach up to 2% each. Figure 13.3 represents the uncertainties on Z/γ ratios of the recoil distributions. The left plot shows the impact of the following nuisances: QCD scale (black line) and shape (red line) uncertainties, which tend to flip sign at around

350-400 GeV, while the EW-QCD mixing is smaller along the whole E_T^{miss} spectrum. The largest uncertainty at high p_T is represented by the process dependent nuisance, which varies from -2% for hadronic recoil smaller than 400 GeV to $+2\%$ at high recoil. In contrast, Figure 13.3 (right) shows the impact of NLO EW uncertainties on the Z/γ. These uncertainties are the dominating at high p_T, which can reach up to 2% each.

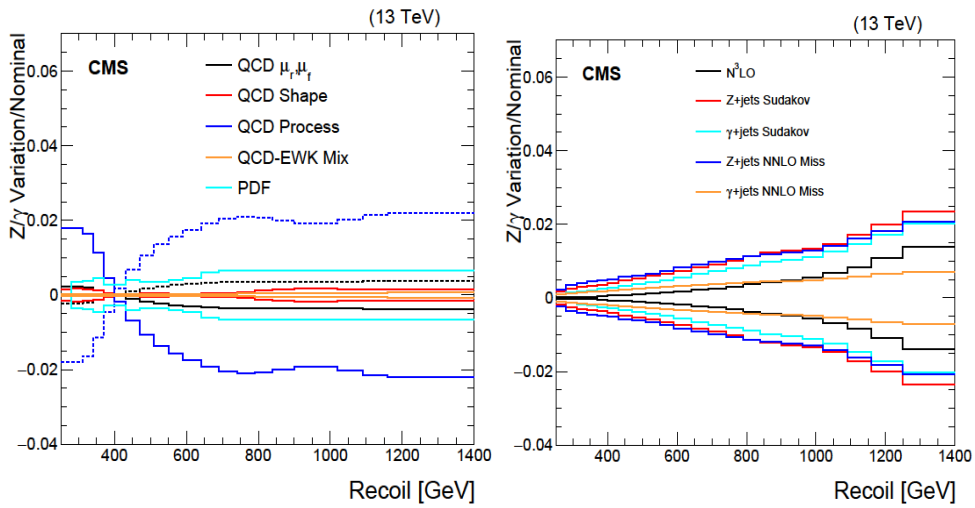

Figure 13. 3. Theoretical uncertainties on the Z/γ transfer factors (left) nuisances related to the NLO-QCD re-weight + the mixing between QCD and EW corrections, (right) effect of the nuisance parameters related to NLO EW corrections. Solid (dashed) lines in (left) are showing the positive (negative) one sigma shift of the nuisance parameters for which the Z/γ can flip sign wrt the nominal value as a function of p_T (Daci et al., 2016).

13.3. Systematic Uncertainties on Minor Backgrounds

Table 13.2 shows the list of systematic uncertainties considered on minor backgrounds which are taken directly from simulation (single-top, $t\bar{t}$, di-bosons) or from data (QCD multi-jets).

13.4. Validation in Data

The NLO and the electroweak corrections are checked by looking at pre-fit ratio for the Z + jets events to both γ + jet events and W + jet events. The values of the higher order NLO QCD and electroweak corrections will change the ratio allowing for an independent cross check. This is a particularly beneficial for the EW

Table 13. 2. Normalisation uncertainties used in the analysis on minor backgrounds populating SR and CRs (Daci et al., 2016).

Source	Process	Uncertainty
Luminosity	All except for data driven backgrounds	2.6%
Electron trigger	MC bkgs in Weν and Zee CRs	1%
Photon trigger	MC bkgs in γ+jets CR	1%
E_T^{miss} trigger	MC bkgs/signal in SR, Wμν and Zμμ CRs	shape vs E_T^{miss}
Jet energy scale	MC bkgs/signal in SR and CRs	5%
Muon-reco efficiency	MC bkgs in Wμν and Zμμ CRs	1%
Muon-ID efficiency	MC bkgs in Wμν and Zμμ CRs	1%
Electron-reco efficiency	MC bkgs in Weν and Zee CRs	1%
Electron-ID efficiency	MC bkgs in Weν and Zee CRs	2%
Photon-ID efficiency	MC bkgs in γ +jets CR	2%
Lepton veto	MC bkgs in SR like Zℓℓ, $t\bar{t}$ VV	shape vs E_T^{miss}
Photon purity	QCD in Photon CR	40%
b-jet veto	Top in SR and all CRs	6%
	All remaining in SR and all CRs	2%
Top P_T reweight	Top	10%
Top norm	Top	10%
VV norm	VV	20%
Z($\ell\ell$) + jets norm	Z($\ell\ell$) + jets (SR)	20%
γ + jets norm	γ + jets (SR)	20%
QCD (shape from DD)	QCD (SR)	~100%

corrections, where the higher order corrections for photons, W bosons, and Z bosons all differ. Figure 13.4 shows the ratio of Z($\ell\ell$) to γ events as a function of the recoil for the monojet final states. Data and simulation after the application of the NLO corrections are in good agreement. Figure 13.5 shows the ratio of Z($\ell\ell$) and W($\ell\nu$) in data and simulation. The agreement is reasonably good, both experimental and theoretical uncertainties are represented by the gray band. The offset in the data/MC ratio observed in the Z(ee)/W(eν) ratio is due to the normalisation discrepancy between data and MC. Figure 13.6 shows comparison between data and MC simulation of the W($\ell\nu$)/γ+jets ratio.

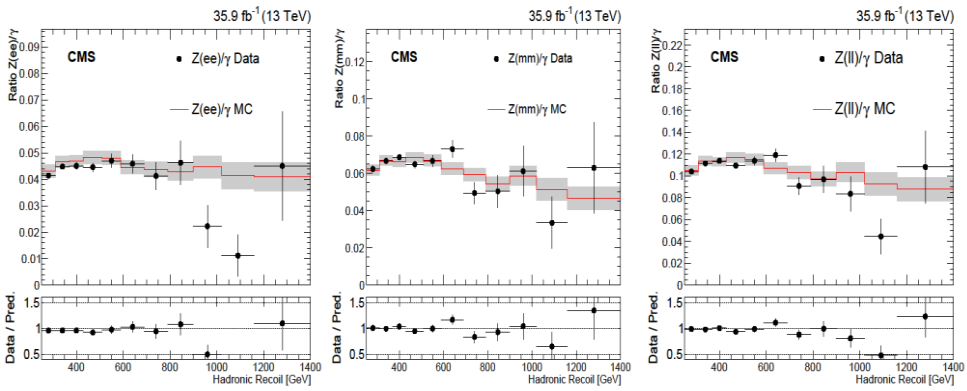

Figure 13. 4. Comparison of data and MC simulation for the Z/γ+jets ratio as a function of the hadronic recoil in the monojet in electron (left), muon (middle) and combined (right) channels respectively. The gray bands represent both the systematic uncertainties and also statistical uncertainty in the simulation (Daci et al., 2016).

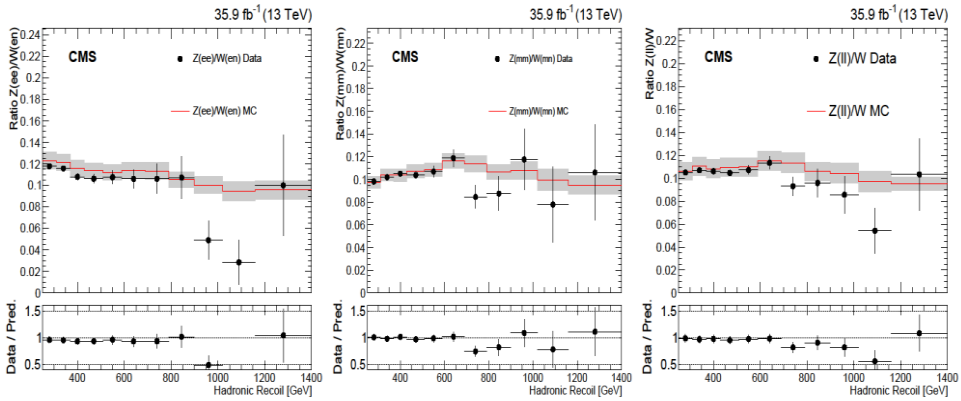

Figure 13. 5. Comparison of data and MC simulation for the Z(ℓℓ)/W(ℓν) ratio as a function of the hadronic recoil in the monojet in electron (left), muon (middle) and combined (right) channels respectively. The gray bands represent both systematic uncertainties and also statistical uncertainty in the simulation (Daci et al., 2016).

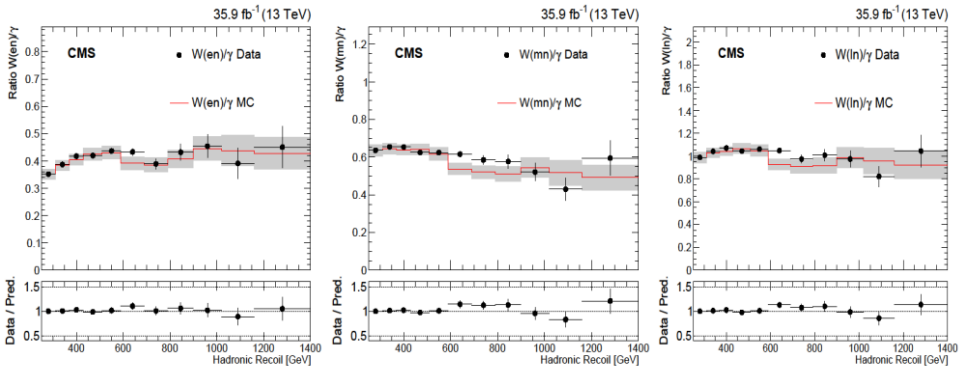

Figure 13. 6. Comparison of data and MC simulation for the W(ℓν)/γ+jets ratio as a function of the hadronic recoil in the monojet in electron (left), muon (middle) and combined (right) channels respectively. The gray bands represent both systematic uncertainties and also statistical uncertainty in the simulation (Daci et al., 2016).

14. RESULTS

14.1. Control Region Only Fit

We obtain binned re-weighting factors for the simulated major background ($Z \rightarrow \nu\nu$ and $W \rightarrow \ell\nu$), on maximizing the likelihood with respect to the $\mu^{Z\rightarrow\nu\nu}$ parameter for each category. Then these reweigthed events provide the recoil templates for the $Z \rightarrow \nu\nu$ and $W \rightarrow \ell\nu$, called post-fit distributions. The post-fit results from the simultaneous fit of monojet, considering only data from the CRs, are shown in Figure 14.1 for dimuon CR and dielectron CR, Figure 14.2 for γ+jets CR, Figure 14.3 for single muon CR, and single electron CR. Good agreement is observed in all CRs. The simultaneous fit is performed using the theoretical uncertainties on both Z/Wand Z/γ ratios.

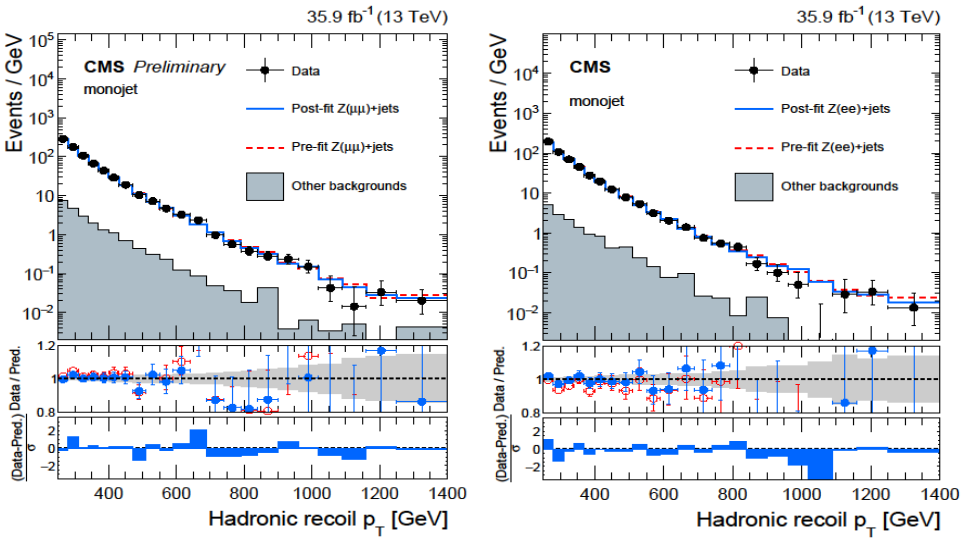

Figure 14. 1. Comparison between data and prediction in dimuon (left) and dielectron (right) CR before and after the simultaneous CR-only fit. Ratio plots with the gray band shows individual uncertainty with all systematics per-bin (Daci et al., 2016).

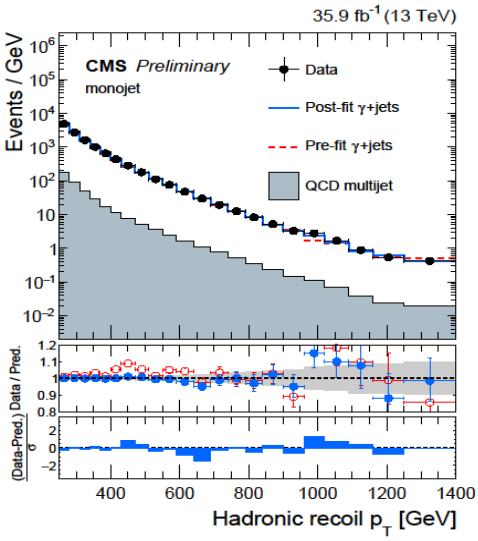

Figure 14. 2. Comparison between data and prediction in γ+jets CR before and after the simultaneous CR-only fit. Ratio plots with the gray band shows individual uncertainty with all systematics per-bin (Daci et al., 2016).

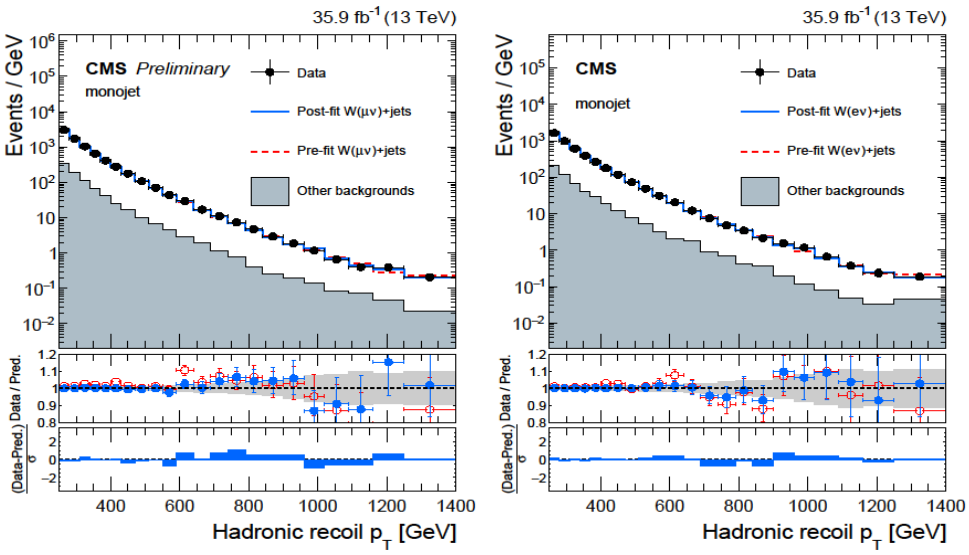

Figure 14. 3. Comparison between data and prediction in single muon (left) and single electron (right) CR before and after the simultaneous CR-only fit. Ratio plots with the gray band shows individual uncertainty with all systematics per-bin (Daci et al., 2016).

The post-fit background prediction and data are compared for observed E_T^{miss} distribution in monojet SR as shown in Figure 14.4, in which in the SR is masked from the likelihood. In this case, the post fit background prediction is fully oblivious to the data in the SR. The fit performed only in the CRs is shown in the plot. The last bin includes all events with $E_T^{miss} > 1250$ GeV for the monojet. In the lower panels, the ratio of data and the post-fit background prediction is shown for the monojet SR. The gray band also in the lower panel shows the post-fit uncertainty after applying all the systematic uncertainties. Eventually, the distributions of the pulls are shown in lower panel and are defined as the difference between data and the post-fit background prediction relative to sum in quadrature of the post-fit uncertainty in the prediction and the statical uncertainty on data.

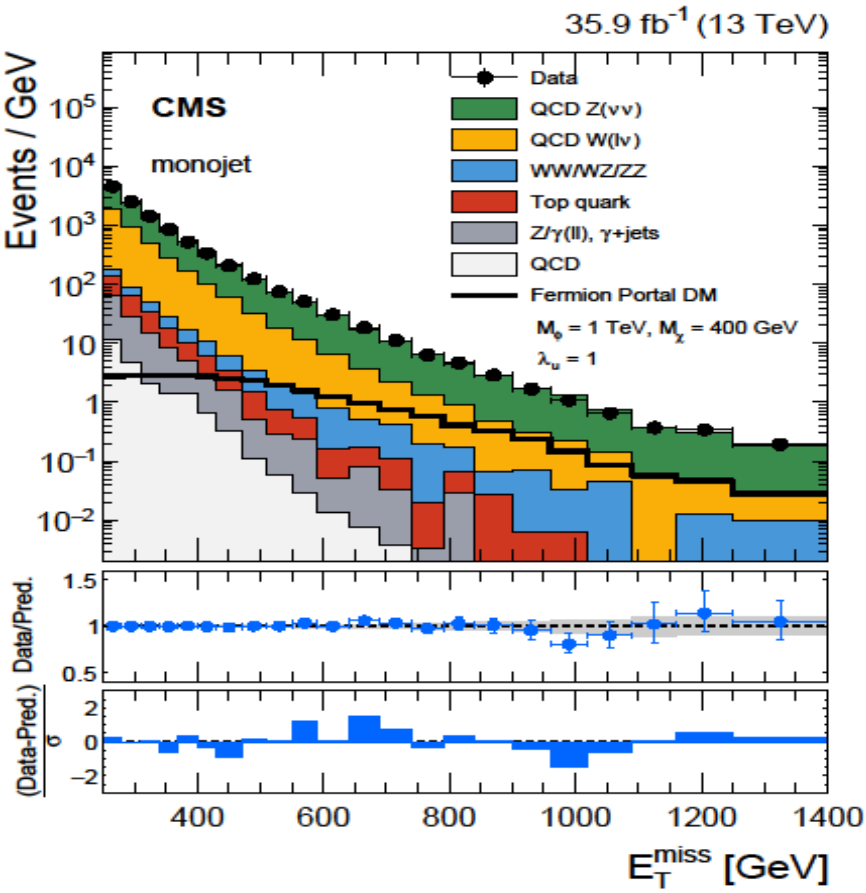

Figure 14. 4. Observed E_T^{miss} distribution in the monojet SR compared with the background expectations for various SM processes evaluated after performing a combined maximum likelihood fit to the data in all the control samples, but excluding the SR. Black curve shows E_T^{miss} distributions from FP DM model with M_ϕ = 1 TeV and M_χ = 400 GeV according to λ_u= 1. The gray bands indicate the post-fit uncertainty in the background prediction on the ratio plots.

Tables 14 shows the estimated yields of SM background processes and their observed event yields in the monojet SR.

Table 14. 1. The SM background predictions and corresponding uncertainties compared to the data in each E_T^{miss} bin are reported in the monojet SR. The background yields and the corresponding uncertainties are obtained after performing a combined fit to data in all the control samples, but excluding data in the SR (Daci et al., 2016).

E_T^{miss} (GeV)	Observed	Z→νν +jets	W→ℓν+jets	Top	Diboson	Other	Total Bkg.
250-280	136865	79700±2300	49200±1400	2360±200	1380±220	1890±240	134500 ± 3700
280-310	74340	45800±1300	24950±730	1184±99	770±120	84±110	73400±2000
310-340	42540	27480 ± 560	13380 ± 260	551 ± 53	469 ± 77	445 ± 63	42320 ± 810
340-370	25316	17020 ± 350	7610 ± 150	292 ± 28	301 ± 51	260 ± 39	25490 ± 490
370-400	15653	10560 ± 220	4361 ± 91	157 ± 17	198 ± 33	152 ± 26	15430 ± 310
400-430	10092	7110 ± 130	2730 ± 47	104 ± 12	133 ± 23	84 ± 15	10160 ±170
430-470	8298	6110 ± 100	2123 ± 37	75.2 ± 7.9	110 ± 19	67 ± 11	8480 ± 140
470-510	4906	3601 ±75	1128 ± 22	38.6 ± 5.3	75 ± 12	21.± 3.9	4865 ± 95
510-550	2987	2229 ± 39	658 ± 12	18.5 ± 3.3	51.7 ± 9.5	12 ± 2.4	2970 ± 49
550-590	2032	1458 ± 27	398 ± 8	12.3 ± 2.6	35.9 ± 7.1	9.7 ± 1.9	1915 ± 33
590-640	1514	1182 ± 26	284 ± 7	5.5 ± 1.4	30.9 ± 5.7	2.6 ± 0.7	1506 ± 32
640-690	926	667 ± 15	151 ± 4	4.6 ±_ 1.7	16.7 ±_ 3	4.0 ± 0.8	844 ± 18
690-740	557	415 ± 12	90.4 ± 3.0	3.8 ± 1.5	15.6 ± 3.6	1.7 ± 0.4	526 ± 14
740-790	316	259 ± 9.6	55.2 ± 2.3	0.8 ± 0.5	9.14 ± 2.3	0.2 ± 0.1	325 ± 12
790-840	233	178 ± 7.1	35.3 ± 1.7	1.7 ± 0.8	5.35 ± 1.7	1.4 ± 0.3	223 ± 9
840-900	172	139 ± 6.2	25.2 ± 1.3	1.5 ± 1.2	2.52 ± 1.0	0.04±0.03	169 ± 8
900-960	101	88.1 ± 4.9	14.7 ± 0.9	0.3 ± 0.3	3.88 ± 1.4	0.03± 0.0	107 ± 6
960-1020	65	73.8 ± 4.7	12.0 ± 0.8	0.4 ± 0.3	1.83 ± 0.9	0.02 ± .01	88.1 ± 5.3
1020-1090	46	42.6 ± 3.1	6.7 ± 0.6	0.0 ± 0.0	3.42 ± 1.3	0.01 ± .01	52.8 ± 3.9
1090-1160	26	21.5 ± 2.1	3.5 ± 0.4	0.0 ± 0.0	0.0 ± 0.0	0.01 ± .00	25.0 ± 2.5
1160-1250	31	21.0 ± 2.2	3.3 ± 0.4	0.0 ± 0.0	1.07 ± 0.6	0.01 ± .00	25.5 ± 2.6
1250-1400	29	22.5 ± 2.4	2.9 ± 0.3	0.0 ± 0.0	1.49 ± 0.9	0.01 ± .00	26.9 ±2.8

14.2. Control + Signal Region Background Only Fit

We performed the post-fit resulting from the simultaneous fit of monojet, under the background only hypothesis including data from the SR. The results are shown for dimuon CR and dielectron CR in Figure 14.5, for γ+jets CR in Figure 14.6 and for single muon CR and single electron CR in Figure 14.7. Although the CRs with the larger yields drive the fit, good agreement is observed in all CRs. The simultaneous fit is applied using the theory uncertainties on both Z/Wand Z/γ ratios.

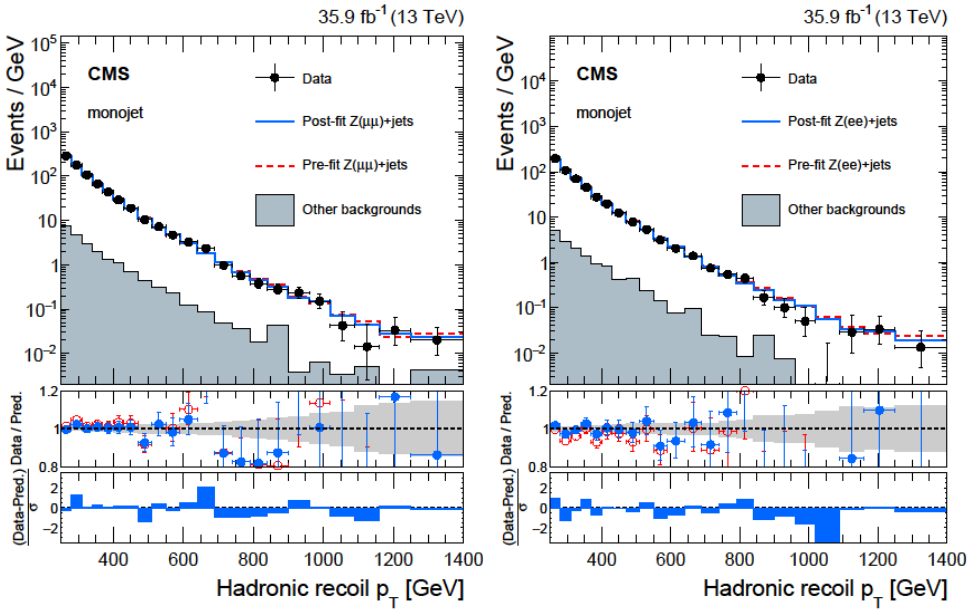

Figure 14. 5. Comparison between data and prediction in dimuon (left) and dielectron (right) CR before and after the simultaneous CR+SR background only fit. Ratio plots with the gray band shows individual uncertainty with all systematics per-bin (Daci et al., 2016).

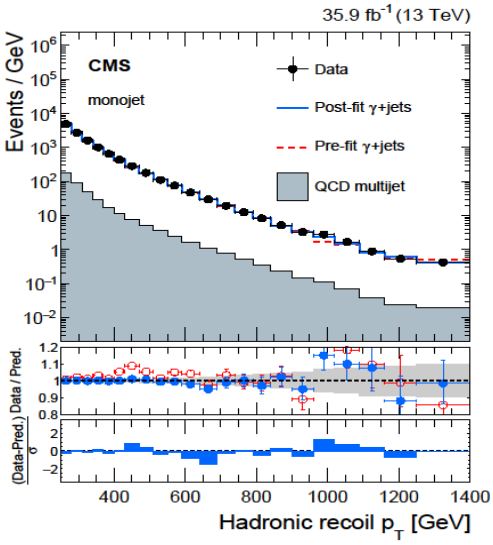

Figure 14. 6. Comparison between data and prediction in the γ+jets CR before and after the the simultaneous CR+SR background only fit. Ratio plots with the gray band shows individual uncertainty with all systematics per-bin (Daci et al., 2016).

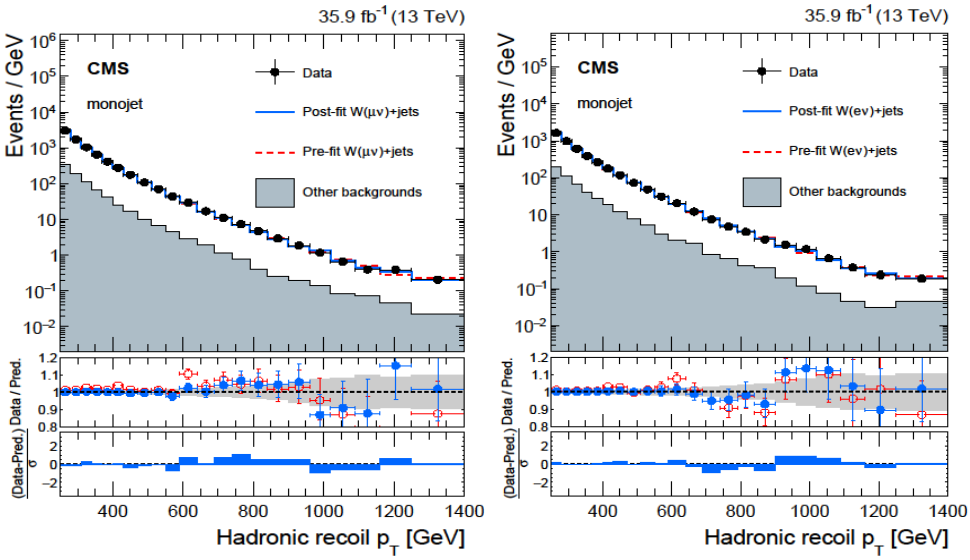

Figure 14. 7. Comparison between data and prediction in single muon (left) and single electron (right) CR before and after the simultaneous CR+SR background only fit. Ratio plots with the gray band shows individual uncertainty with all systematics per-bin (Daci et al., 2016).

Figure 14.8 shows the E_T^{miss} distributions in which the background estimates have been calculated including events from the SR in the fit. But we assume that there is no signal. The comparison of this fit with an alternative fit assuming the presence of signal is used to set limits on the DM signal cross section.

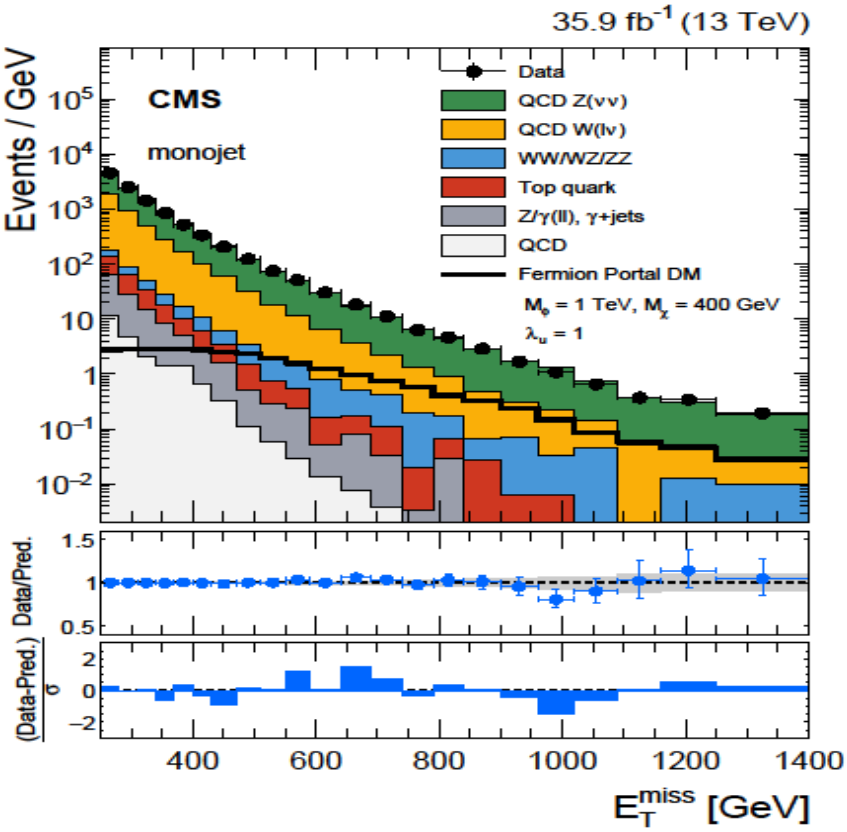

Figure 14. 8. Observed $\boldsymbol{E_T^{miss}}$ distribution are compared for data and SM in the monojet SR with the background expectations for various SM processes evaluated after applying a combined maximum likelihood fit to the data in all the control samples, as well as in the SR. Black curve shows $\boldsymbol{E_T^{miss}}$ distributions from FP DM model with M_ϕ = 1 TeV and M_χ = 400 GeV according to λ_u= 1. The fit is performed assuming the absence of any signal. For the monojet SRs, ratio of data and the post-fit background prediction is shown. The gray bands are indicative of the post-fit uncertainty in the background prediction in the lower panel, ratio plots.

15. MODEL INTERPRETATIONS

15.1. Limit on ADD Model

Searches for ADD model in the jet plus E_T^{miss}has already been performed by CDF (1.1 fb^{-1} and 2.0 $\mathrm{fb}^{-1}$of data respectively CDF Collaboration, 2008), D0 in jet $+ E_T^{miss}$ and $\gamma + E_T^{miss}$ (2.7 fb^{-1} D0 Collaboration,2008), and LEP experiments (Delgado A. and Strassler M., 2010). ADD searches have been completed recently by CMS (CMS Collaboration,2015) and ATLAS (M. A. et al., 2016) in the jet $+ E_T^{miss}$ signature. So far no evidence of such a new physics signatures has been observed, therefore exclusion limits in the parameter space have been set. Upper limits on the graviton production cross section at 95% CL are shown in Figure 15.1 as a function of M_{D} and for several values of n_{ED}. Limits are obtained from a binned Likelihood fit of the E_T^{miss} spectrum of the selected monojet events, as shown in previous sections. To summarize the best exclusion limit for the ADD model, Figure 15.2 shows the highest excluded M_{D} value as a function of n_{ED}. The expected exclusion in M_{D} ranges from 10 to 5 TeV while changing n_{ED} from 2 to 6.

Table 15.1 shows signal efficiency of ADD model samples after monojet events selection for each *n* versus M_{D} and also shows the grid in with full simulation.

Table 15. 1. ADD model acceptance for different *n* vs M_{D}.

n	M_{D} [TeV]									
	3	4	5	6	7	8	9	10	11	12
2			0.145	0.146	0.145	0.147	0.147	0.146	0.147	0.146
3		0.17	0.175	0.176	0.174	0.173	0.174	0.173	0.174	
4	0.177	0.184	0.186	0.186	0.188	0.187	0.191			
5	0.181	0.193	0.194	0.196	0.198					
6	0.179	0.195	0.196	0.202	0.203					

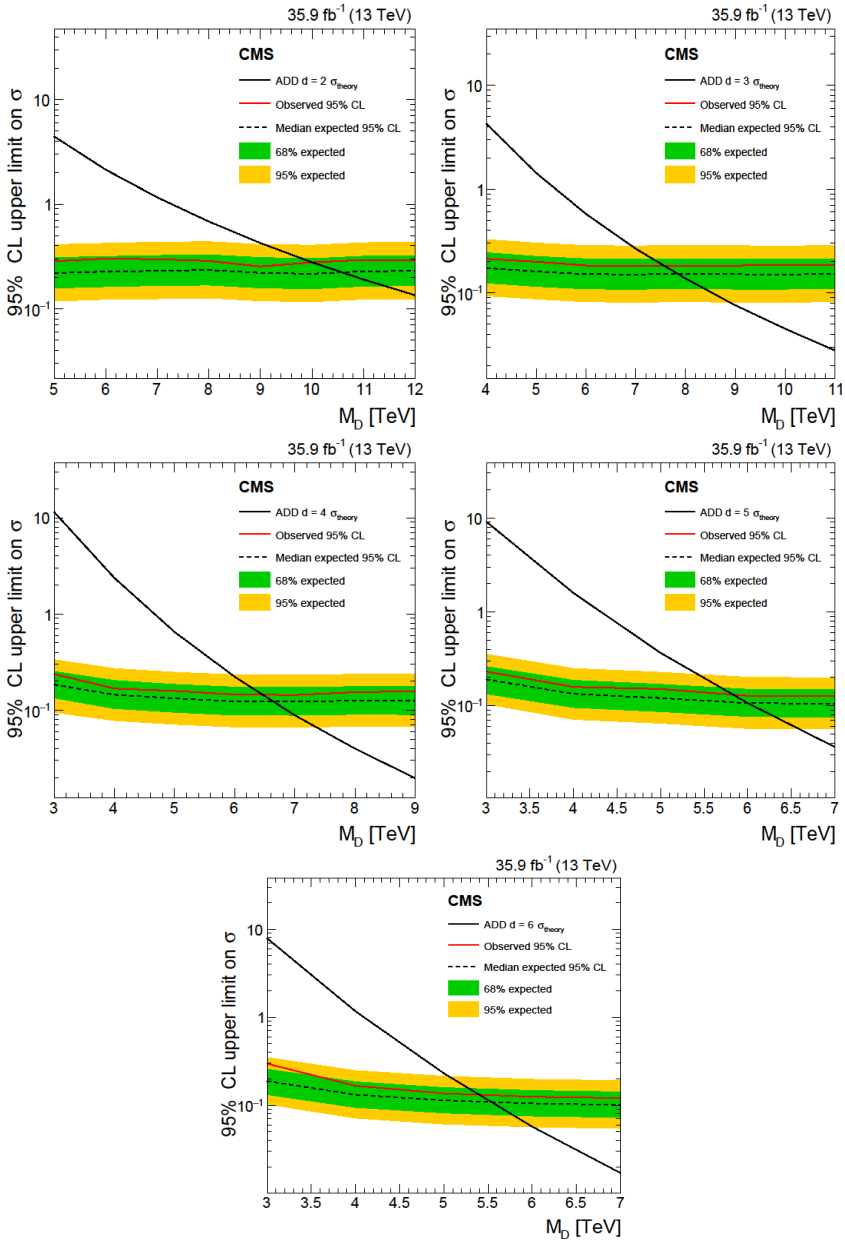

Figure 15. 1. The observed and expected upper limit on the graviton production cross section. Green ($\pm 1\sigma$) and yellow ($\pm 2\sigma$) bands show the on the expected limits. Black solid line which is showing theoretical cross section for comparision.

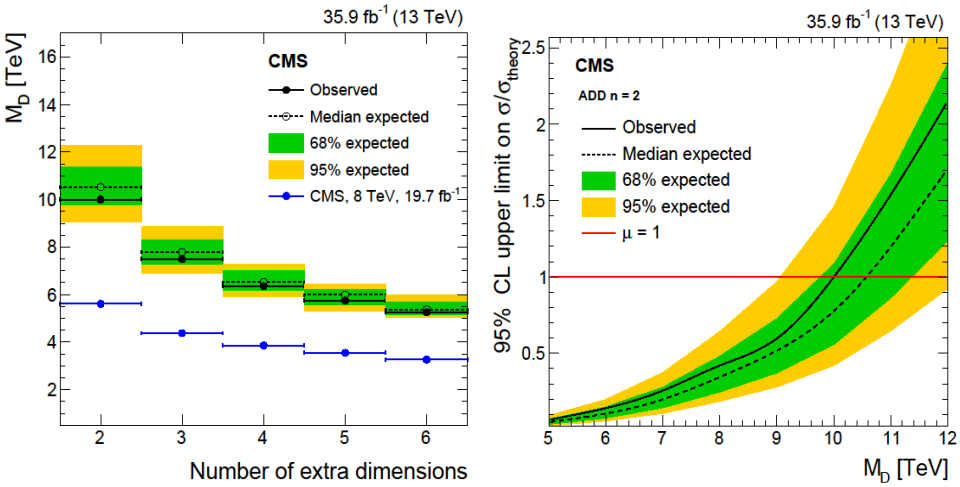

Figure 15. 2. The 95% CL observed and expected upper limits on ADD graviton production (left), as a function of fundamental Planck scale (M_D) for n = 2, where n is the number of extra spatial dimensions. The 95% CL expected and observed lower limits (right) on M_D as a function of n in the ADD model. Comparison between the results and previous ones obtained by the CMS Collaboration with data corresponding to an integrated luminosity of 19.7 fb^{-1} at a centre-of-mass energy of 8 TeV (blue points).

15.2 Fermion Portal Dark Matter Model

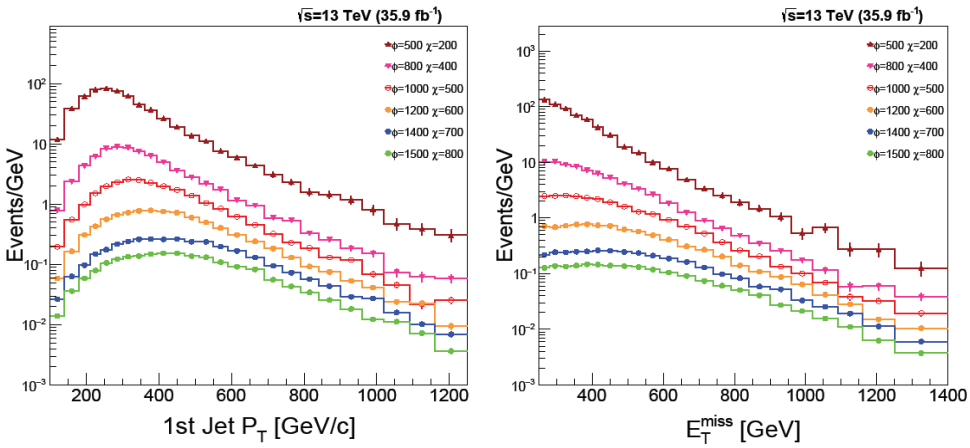

Figure 15. 3. Reconstracted level jet p_T (left) and MET (right) distrubitons for varios M_ϕ and M_χ.

15.2.1 Signal Efficiency

Table 15.2 shows signal efficiency of Dirac FP DM samples after monojet events selection criteria. The table shows the grid in $M_\chi - M_\phi$ plane used to perform the mass scan with full simulation.

15.2.2. Validation of Dirac Fermion Dark Matter Signal

To validate the Dirac Fermion DM samples produced privately, we compared few mass points with the official CMS production for validation purpose. In Figure 15.4, the expected distribution for the E_T^{miss} (a), leading jet P_T (b), number of jets (c) and jets multipliycity (d) are reported for a chosen mass point with $M_\phi = 1$ TeV and $M_\chi = 400$ GeV. The two samples are fully consistent within the statistical uncertainties.

Table 15. 2. Signal efficiency of Dirac FP DM samples after monojet events selection in the M_ϕ - M_χ plane.

M_χ [GeV]	M_ϕ [GeV]									
	500	550	600	650	800	1000	1200	1400	1500	1600
1000	0.14	0.14	0.14	0.15	0.15	0.15	0.28	0.44	0.45	0.46
800	0.13	0.13	0.13	0.14	0.14	0.28	0.43	0.46	0.44	0.43
700	0.12	0.13	0.13	0.13	0.15	0.37	0.44	0.45	0.42	0.41
600	0.11	0.12	0.12	0.11	0.26	0.42	0.45	0.42	0.40	0.37
500	0.11	0.10	0.12	0.18	0.35	0.44	0.43	0.39	0.36	0.34
400	0.11	0.16	0.23	0.28	0.39	0.42	0.40	0.35	0.32	0.30
300	0.20	0.25	0.30	0.34	0.40	0.40	0.36	0.31	0.29	0.26
200	0.26	0.30	0.33	0.35	0.37	0.36	0.31	0.27	0.24	0.20
100	0.27	0.30	0.32	0.33	0.34	0.31	0.26	0.22	0.20	0.18
10	0.25	0.27	0.29	0.30	0.30	0.26	0.22	0.18	0.18	0.15

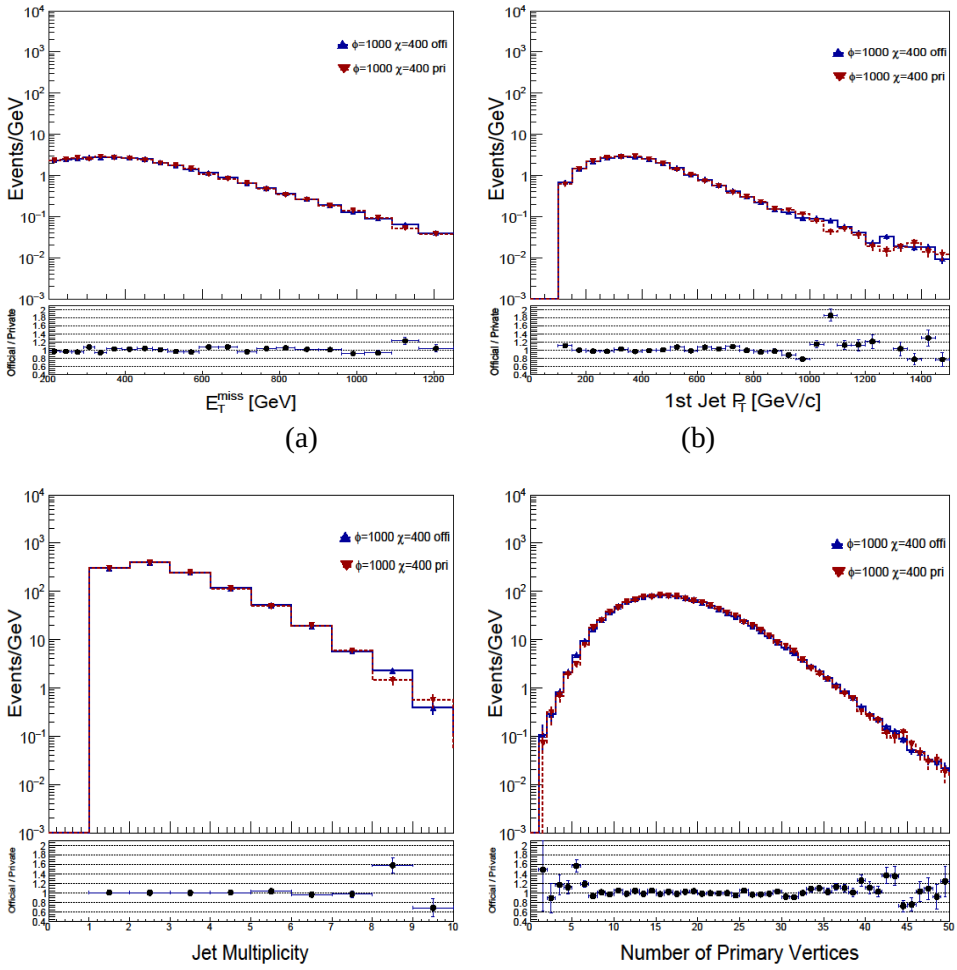

(a) (b)

(c) (d)

Figure 15. 4. Comparison between offcial sample (blue line) and private production sample (red line) for dirac DM M_ϕ = 1 TeV and M_χ = 400 GeV.

15.2.3 Limit on Dirac Fermion Portal Dark Matter Signal

The monojet category selections, which have been described in previous sections, are applied to the FP signal events. Expected exclusion limits at 95% C.L. on the signal strength are presented in the $M_\chi - M_\phi$ plane. The exclusion contours for $\lambda_u = 1$ are shown in Figure 15.5 (right). The exclusion limit extends up to around

1.4 TeV on mediator mass, and up to 600 GeV on DM masses are excluded. We have included the co-annihilation effects for the degenerate spectrum. We show the thermal relic required parameter space in the dark blue and solid line in Figure 15.5.

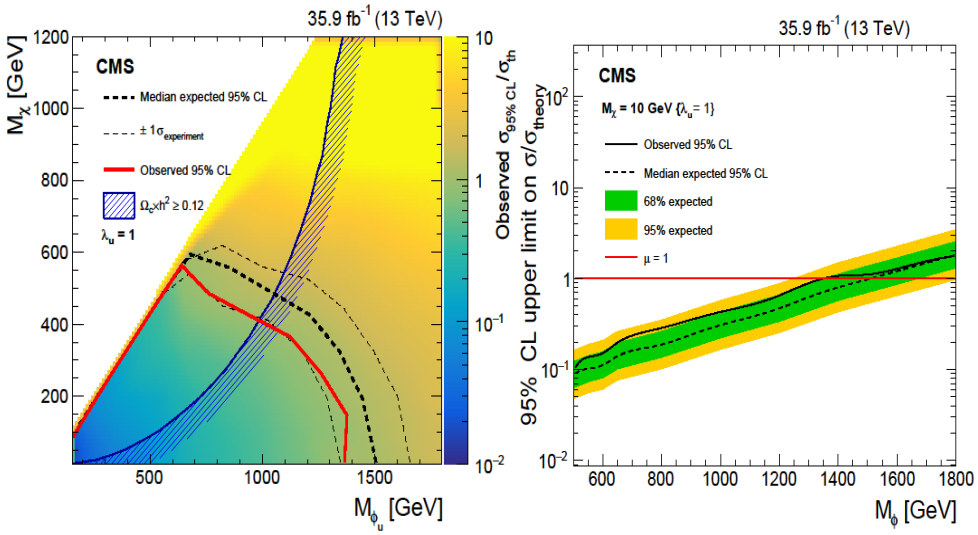

Figure 15. 5. 95% CL expected (black dashed line) and observed (red solid line) upper limits on $\mu = \sigma/\sigma_{th}$ for Dirac DM with the coupling strength parameter for the up quark corresponding to $\lambda_u = 1$ in the $M_\phi - M_\chi$ plane. Constraints from the Planck satellite experiment are shown with the dark blue contours. DM is overabundant in the shaded area.

16. CONCLUSION

The *s*-chanel DM production are extensively studied in Run 1, but there is no published result on the *t*-channel DM production. Fermion portal model is one of the *t*-channel DM models. This is the main motivation of the present study. A dominant monojet channel produces a mediator and a DM, followed by a decay of the mediator to a quark and DM. The decay of the mediator produces a Jacobian like structure in the E_T^{miss} distribution, while the *s*-channel DM produces a simple dumping E_T^{miss}spectrum. These models produce different types of signal shape in the P_{T} imbalance distribution. For all models, the signal extraction is performed by considering the shape of the P_{T} imbalance in each event category. Therefore, we look for excess in the E_T^{miss} spectrum over the SM background for the DM and extra dimensions.

In this thesis, the search for DM with monojet beyond SM using data from proton-proton collisions at $\sqrt{s}$ =13 TeV recorded with the CMS experiment is presented. We do not see any significant deviation from the SM expectation and therefore we set upper limits on the production cross section of DM in the context of simplified models with FP and ADD models. Fermion portal Dirac DM signal events are generated using MadGraph5 at LO, showered by PYTHIA 8 and finally passed through the CMS full simulation. 200 data sets which have different M_{ϕ} and M_{χ} are produced for mass scanning. The samples are analyzed according to Monojet analysis framework. The results are interpreted in terms of simplified *t*-channel DM models assuming a scaler mediator decaying into a pair of fermionic DM particles.

As a result, mediator masses up to 1.4 TeV, and DM masses up to 600 GeV are excluded. In additon, the results are also interpreted in terms of stringent limits on the fundamental Planck scale in the ADD model which is another well known model with large extra spatial dimensions. The lower limits are also computed on the fundamental Planck scale M_{D} in the context of the large extra dimensional model

where the exclusion is found to be varying between 10 TeV for the number of extra dimensions n = 2 to 5.5 TeV for n = 6 (Table 16.1).

Table 16. 1. Upper limits on the signal production cross section in the ADD model and lower limits on M_D as a functions of the number of extra spatial dimensions (n).

n	Observed (expected) cross section exclusion [pb]	Observed (expected) M_D exclusions [TeV]
2	0.28 (0.22)	9.9 (10.5)
3	0.18 (0.15)	7.5 (7.8)
4	0.15 (0.13)	6.3 (6.5)
5	0.13 (0.11)	5.7 (6.0)
6	0.13 (0.10)	5.3 (5.4)

REFERENCES

Aad, G., et al., 2008., "The ATLAS Experiment at the CERN Large Hadron Collider". Journal of Instrumentation 3, 08, p. S08003 (2008).

Aaboud, M. *et a, 2016. (*ATLAS collaboration*),* Search for new phenomena in final states with an energetic jet and large missing transverse momentum in pp collisions at *s√=13* TeV using the ATLAS detector, Phys. Rev. *D 94 (2016) 032005 [arXiv:1604.07773] [INSPIRE]*.

Aaij, R., et al., 2015. "LHCb Detector Performance". Int. J. Mod. Phys. 30 (2015), no. 07 1530022, arXiv:1412.6352.

Aamodt, K., et al., 2008. "The ALICE experiment at the CERN LHC". Journal of Instrumentation 3, 08, p. S08002 (2008).

Aartsen, M. G. et al, 2018. IceCube Collaboration: (Journal) Physical Review D98 (2018) 062003, 12 September 2018; e-print archive arXiv:1807.01820 [astro-ph.HE]

Abdallah, J. et. al, 2015. "Simplified models for dark matter searches at the LHC", Phys. Dark Univ. 9-10 (2015) 8-23, doi:10.1016/j.dark.2015.08.001

Abercrombie, D., et al, 2015. Dark matter benchmark models for early LHC Run-2 searches: Report of the ATLAS/CMS Dark Matter Forum, arXiv:1507.00966.

Ackermann, M. et al, 2011. Fermi-LAT collaboration Collaboration,. Constraining Dark Matter Models from a Combined Analysis of Milky Way Satellites with the Fermi Large Area Telescope," Phys.Rev.Lett. 107 (2011) 241302, arXiv:1108.3546 [astro-ph.HE].

Akerib, D. S. et al., 2014. (LUX Collaboration), First Results from the LUX Dark Matter Experiment at the Sanford Underground Research Facility, Phys. Rev. Lett. 112, 091303 (2014).

Alves, A. A., et al., 2008. "The LHCb Detector at the LHC". J. Instrum. 3 (2008), no. LHCb-DP-2008-001. CERN-LHCb-DP-2008-001 S08005.

Anelli, G., et al. 2008. *The* Totem *experiment at the* cern *Large Hadron collider*, *JINST* **3** (2008) S08007.

Antoniadis, I., Benakli K., and Quiros M., 1999. "Direct collider signatures of large extra dimensions", Phys. Lett. B 460 (1999) 176, doi:10.1016/S0370-2693(99)00764-9, arXiv:hep-ph/9905311.

Arkani-Hamed, N., Dimopoulos, S., and Dvali, G., 1998. "The hierarchy problem and new dimensions at a millimeter", Phys. Lett. B 429 (1998) 263, doi:10.1016/S0370-2693(98)00466-3, arXiv:hep-ph/9803315.

Arkani-Hamed, N., Dimopoulos, S., and Dvali, G., 1999. "Phenomenology, astrophysics and cosmology of theories with submillimeter dimensions and TeV scale quantum gravity", Phys. Rev. D 59 (1999) 086004, doi:10.1103/PhysRevD.59.086004, arXiv:hep-ph/9807344.

Aprile, E. et al., 2012. (XENON100 Collaboration), \Dark Matter Results from 225 Live Days of XENON100 Data," Phys.Rev.Lett. 109 (2012) 181301, arXiv:1207.5988 [astro-ph.CO].

Aprile, E. et al., (XENON Collaboration): Dark Matter Results from 225 Live Days of XENON100 Data http://arxiv.org/abs/1207.5988

Bayatiyan, G. L., et al., 2006. CMS Physics, "Tehcnical Design Report, Volume I: Detector Performance and Software", 2006-001, CMS TDR 8.1, CERN/LHCC.

Bayatiyan, G. L., et al., 2000a. CMS TriDAS Project Technical Design Report Volume 1.

Bayatiyan, G. L., et al., 2000b. CMS TriDAS Project Technical Design Report Volume 2: The Data Acquisition System, Technical Report 2002-26 CERN/LHCC.

Bayatiyan, G. L., et al.,1998. The Tracker Project Technical Design Report, CERN-LHCC- 98-006 (1998).

Bayatiyan, G. L., et al., 1997a. CMS Electromagnetic Calorimeter Project Technical Design Report, CERN/LHCC-97-33.

Bayatiyan, G. L., et al., 1997b. CMS Hadronic Calorimeter Project Technical Design Report, CERN/LHCC-97-31.

Bayatiyan, G. L., et al., 1997c. CMS Magnet Technical Design Report, CERN/LHCC-97- 10.

Bayatiyan, G. L., et al., 1997d. CMS Muons Technical Design Report, CERN/LHCC-97-32.

Berry, T. S., 2005. "Extra Dimension Searches at Accelerators"

Bai, Y. and Berger J.,2013. "Fermion Portal Dark Matter", JHEP 11 (2013) 171, doi:10.1007/JHEP11(2013)171, arXiv:1308.0612.

Bai, Y., Barger V., Everett L. L., and Shaughnessy G., 2HDM Portal Dark Matter: LHC data and the Fermi-LAT 135 GeV Line, arXiv:1212.5604.

Bai, Y., Carena M., and Lykken J., 2009. Dilaton-assisted Dark Matter, Phys.Rev.Lett. 103 (2009) 261803, [arXiv:0909.1319].

Chatrchyan, S., et al. 2013, The performance of the CMS muon detector in proton proton collisions at ps = 7 TeV at the LHC. JINST, 8:P11002, 2013

Chatrchyan, S., et al. 2010. Commissioning and performance of the CMS pixel tracker with cosmic ray muons. JINST 5 (2010) T03007, doi:10.1088/1748-0221/5/03/T03007, arXiv:0911.5434.

Chatrchyan, S., et al. 2008. "The CMS experiment at the CERN LHC", *JINST* **3** (2008) S08004, http://dx.doi.org/10.1088/1748-0221/3/08/S08004

Chatrchyan, S., et al. S., et al., 2012c. "Observation of a new boson at a mass of 125 GeV with the CMS experiment at the LHC," Phys. Lett. B, vol. 716, pp. 30–61, 2012.

Cern accelerator complex, http://te-epc-lpc.web.cern.ch/te-epc-lpc/ machines/pagesources/Cern-Accelerator-Complex.jpg.

Cheung, K. and Yuan, T. C., 2007. Hidden fermion as milli-charged dark matter in Stueckelberg Z-prime model, JHEP 0703 (2007) 120, [hep-ph/0701107].

CDF Collaboration, 2008. "Search for large extra dimensions in final states containing one photon or jet and large missing transverse energy produced in pp¯ collisions at ps=1.96 TeV", Phys. Rev. Lett. 101 (2008) 181602, doi:10.1103/PhysRevLett.101.181602.

Daci, N. et al., 2016. "Search for dark matter produced with an energetic jet or a hadronically decayingWor Z boson at $\sqrt{s}$ =13 TeV with the full 2016 dataset", Technical Report, CERN, 2016. CMS Analysis Note : AN-16-473.

CMS BTV POG. https://twiki.cern.ch/twiki/bin/viewauth/CMS/BtagRecommendation74X.

CMS EGamma POG. https://twiki.cern.ch/twiki/bin/viewauth/CMS/CutBasedElectronIdentificationRun2#Spring15_selection_25ns.

CMS Muon POG. https://twiki.cern.ch/twiki/bin/view/CMSPublic/SWGuideMuonIdRun2#Loose_Muon.

CMS Muon POG. https://twiki.cern.ch/twiki/bin/view/CMSPublic/SWGuideMuonIdRun2#Tight_Muon.

CMS Jet/MET POG. https://twiki.cern.ch/twiki/bin/viewauth/CMS/MissingETOptionalFiltersRun2.

CMS Collaboration, "Search for dark matter, extra dimensions, and unparticles in monojet events in proton-proton collisions at ps = 8 TeV", Eur. Phys. J. C75 (2015), no. 5, 235, doi:10.1140/epjc/s10052-015-3451-4, arXiv:1408.3583.

CMS Collaboration., 2014. "Description and performance of track and primary-vertex reconstruction with the CMS tracker," Journal of Instrumentation, vol. 9, no. 10, p. P10009, (2014).

DAMA/LIBRA Collaboration, 2018. DAMA/LIBRA-phase2 in WIMP effective models doi: 10.1088/1475-7516/2018/07/016, arXiv:1804.07528v2

Delgado, A., and Strassler, M., 2010. "A Simple-Minded Unitarity Constraint and an Application to Unparticles", Phys. Rev. D 81 (2010) 056003, doi:10.1103/PhysRevD.81.056003.

D0 Collaboration, 2008. "Search for Large Extra Dimensions via Single Photon plus Missing Energy Final States at ps = 1.96 TeV", Phys. Rev. Lett. 101 (2008) 011601, doi:10.1103/PhysRevLett.101.011601.

DiFranzo, A. et al, 2013. "Simplified Models for Dark Matter Interacting with Quarks" JHEP 1311 (2013) 014, doi: 10.1007/JHEP11(2013)014

Evans, L., and BRYANT P., 2008. "LHC Machine". JINST 3 (2008) S08001.

Fabienne, M., 2013. "CERN's Accelerator Complex. La chaîne des accélérateurs du CERN" (2013), Oct. https://cds.cern.ch/record/1621583. – General Photo (cited on page 8.)

Frederix, R. and Frixione, S., 2012. "Merging meets matching in MC@NLO", JHEP **12 (**2012)061, doi:10.1007/JHEP12(2012)061, arXiv:1209.6215.

Giudice, G., Rattazzi R., and Wells J., 1999. "Quantum gravity and extra dimensions at high-energy colliders", Nucl. Phys. B **544** (1999) 3, doi:10.1016/S0550-3213(99)00044-9, arXiv:hep-ph/9811291.

Grachov, O. A et al., 2006. "Status of zero degree calorimeter for CMS experiment", AIP Conf. Proc. 867 (2006) 258 [nucl-ex/0608052].

Graham P. et al., 2015. "Towards a Bullet-proof test for indirect signals of dark matter," arXiv:1502.03824 [hep-ph], Phys. Rev. D 91, 103524

Hooper D., 2008. "Particle Dark Matter", in "Proceedings of Theoretical Advanced Study Institute in Elementary Particle Physics on The dawn of the LHC era (TASI 2008): Boulder, USA, June 2-27, 2008", pp. 709–764. 2010. arXiv:0901.4090. "http://lss.fnal.gov/cgi-bin/find_paper.pl?conf-09-025",

IceCube Collaboration, 2016. “Improved limits on dark matter annihilation in the Sun with the 79-string IceCube detector and implications for supersymmetry”, JCAP **04** (2016) 022, doi:10.1088/1475-7516/2016/04/022, arXiv:1601.00653.

Kallweit S. et al., 2015. “NLO electroweak automation and precise predictions for W+multijet production at the LHC”, JHEP **04** (2015) 012, doi:10.1007/JHEP04(2015)012, arXiv:1412.5157.

Kallweit S. et al., 2015. “NLO QCD+EWautomation and precise predictions for V+multijet production”, in Proceedings, 50th Rencontres de Moriond, QCD and high energy interactions, pp. 121–124. 2015. arXiv:1505.05704.

Lee H. M., Park M., and Sanz V., 2013. Gravity-mediated Dark Matter, arXiv:1306.4107.

LUX Collaboration, 2016. "Signal yields, energy resolution, and recombination fluctuations in liquid xenon", Accepted for publication in Phys. Rev. D, December 15, 2016. DOI:10.1103/PhysRevD.95.012008, arXiv:1610.02076

LUX Collaboration, 2017. “Results from a search for dark matter in the complete LUX exposure”, Phys. Rev. Lett. **118** (2017) 021303, doi:10.1103/PhysRevLett.118.021303, arXiv:1608.07648.

MADGRAPH5_AMC@NLO J. Alwall, R. Frederix, S. Frixione, V. Hirschi, F. Maltoni, O. Mattelaer, H.-S. Shao, T. Stelzer, P. Torrielli, and M. Zaro, The automated computation of tree-level and next-to-leading order differential cross sections, and their matching to parton shower simulations, J. High Energy Phys. 07 (2014) 079.

Massey, R. and Kitching, T., 2010. “The dark matter of gravitational lensing,” Rep. Prog. Phys. 73 (2010) 086901.

Mirabelli, E., Perelstein, M., and Peskin, M., 1999. “Collider signatures of new large space dimensions”, Phys. Rev. Lett. **82** (1999) 2236, doi:10.1103/PhysRevLett.82.2236, arXiv:hep-ph/9811337.

M. A. et al., 2016. “Search for new phenomena in final states with an energetic jet and large missing transverse momentum in pp collisions at ps = 13 TeV using the ATLAS detector”, Phys. Rev. D **94** (2016) 032005, doi:10.1103/PhysRevD.94.032005.

Tanabashi, M. et al. 2018. (Particle Data Group), Phys. Rev. D 98 , 030001 (2018) DOI: 10.1103/PhysRevD.98.030001

Nomura, Y. and Thaler, J., 2009. Dark Matter through the Axion Portal, Phys.Rev. D79 (2009) 075008, [arXiv:0810.5397].

NASA: https://science.nasa.gov/astrophysics/focus-areas/what-is-dark-energy

Panagiotou, A., et al., 2008. “CASTOR engineering design report”, CMS Note in preparation (2008). “CERN Accelerators and Technology Sector”, https://espace.cern.ch/acc-tec- sector/default.aspx, February, 2016.

Planck Collaboration., 2016. arXiv:1502.01589v3 [astro-ph.CO]

Ralich, R. M., 2009. “Study of b Quark Pair Production Mechanisms in pp Collisions with the CMS Experiment at LHC”, CERN-THESIS-2009- 021, CMS-TS-2010-040.

Rubin, V. C., N. Thonnard, and J. F. W. K., 1980. Rotational properties of 21 SC galaxies with a large range of luminosities and radii, from NGC 4605 /R = 4kpc/ to UGC 2885 /R = 122 kpc/, ApJ 238 (1980) 471. doi:10.1086/158003.

Salam, A. J. W., et al., 1964, “Electromagnetic and weak interactions,” Phys. Lett. 13 (1964) 168–171.

Shrock, R. E. and Suzuki, M., 1982. INVISIBLE DECAYS OF HIGGS BOSONS, Phys.Lett. B110 (1982) 250.

Simone, De A. and Jacques, T., 2016. “Simplified Models vs. Effective Field Theory Approaches in Dark Matter Searches”, Phys. J. C (2016) 76: 367, doi:10.1140/epjc/s10052-016-4208-4

Sirunyan, A. M. et al. 2018. “Search for new physics in final states with an energetic jet or a hadronically decaying W or Z boson and transverse momentum imbalance at √s=13 TeV”, Phys. Rev. D 97, 092005
DOI: 10.1103/PhysRevD.97.092005

Spencer, C. et al. 2014, Effective WIMPs Phys. Rev. D 89, 015011

Steigman, G. And Turner, M. S., 1985. Cosmological constraints on the properties of weakly interacting massive particles, Nucl. Phys. B **253**, 375 (1985).

tau-POG.
https://twiki.cern.ch/twiki/bin/view/CMS/TauIDRecommendation13TeV#Measurement_in_Z_tautau_events.

Zwicky, F., 1933. Die Rotverschiebung von extragalaktischen Nebeln, Helvetica Physica Acta 6 (1933) 110127.

CURRICULUM VITAE

YALCIN GULER

Date of birth:	25 September 1978
Place of birth:	Kadirli, Turkey
Nationality:	Turkish
Email:	**yalcin.guler**@cern.ch

EDUCATION

2012 – Present	**Ph.D student at Cukurova University** Cukurova University, Institute of Science, Physics Department, Adana, Turkey
2008 - 2011	**Master Degree (M.A. in High Energy Physics)** Cukurova University, Institute of Science, Physics Department, Adana, Turkey
M.A Thesis	Radiation Damage Monitoring System of the Fibers Used in The CMS (Compact Muon Solenoid) Experiment HF Detector
2003 - 2007	**Bachelors Degree (B.A. in Physics)** Cukurova University, Faculty of Science and Letter, Physics Department, Adana, Turkey
1999 – 2001	**Vocational Schools of Higher Education (Computer Programming)** Mustafa Kemal University, Antakya, Hatay

WORK EXPERIENCE

2014-2018	**European Organization for Nuclear Research (CERN)** Dark Matter Physics Research under Exotica.
2016-2018	**European Organization for Nuclear Research (CERN)** Dijet Resonance Physics Research under Exotica
2014-2018	**European Organization for Nuclear Research (CERN)** Hadron Calorimeter (HCAL) Detector analysis Group
2013-2014	**European Organization for Nuclear Research (CERN)** Hadronic Forward (HF) Detector analysis under Hadron Calorimeter (HCAL) Group
2010-2011	**European Organization for Nuclear Research (CERN)** Radiation Damage Monitoring System of The Fibers Used in The CMS (Compact Muon Solenoid) Experiment HF Detector

COURSES AND CONFERENCES ATTENDED

2018	1.Ulusal CERN ile İlgili Faaliyetler Çalıştayı Ankara/TÜRKİYE
2017	TPS-33: Turkish Physical Society 33rd International Physics Congress, 6-10 Sep 2017, Bodrum (Turkey)
2013	C-class occupational safety specialist
2010	The International School Of Trigger And Data Acquisition 2010 (as a assistant in one of the experiment) TAEK - Ankara
2009	Computing Applications for Accelerator and Particle Physics: Turkish Atomic Energy Authority Certificate of Participant
2008	6 th International Student Conference Of the Balkan Physical Union (Experiment Presentation) Bodrum-Turkey
2008	Balkan Physical Union Second İnternational Physics Project Competition (Competitor) Bodrum-Turkey
2008	Fourth International Summer School on Particle Accelerator and Detectors, Bodrum, Turkey